University of Arkansas, Fayetteville
ScholarWorks@UARK

Theses and Dissertations

8-2017

Si-Based Germanium Tin Semiconductor Lasers for Optoelectronic Applications

Sattar H. Sweilim Al-Kabi
University of Arkansas, Fayetteville

Follow this and additional works at: http://scholarworks.uark.edu/etd

Part of the Electromagnetics and Photonics Commons, and the Electronic Devices and Semiconductor Manufacturing Commons

Recommended Citation

Al-Kabi, Sattar H. Sweilim, "Si-Based Germanium Tin Semiconductor Lasers for Optoelectronic Applications" (2017). *Theses and Dissertations*. 2505.
http://scholarworks.uark.edu/etd/2505

This Dissertation is brought to you for free and open access by ScholarWorks@UARK. It has been accepted for inclusion in Theses and Dissertations by an authorized administrator of ScholarWorks@UARK. For more information, please contact scholar@uark.edu, ccmiddle@uark.edu.

Si-Based Germanium Tin Semiconductor Lasers for Optoelectronic Applications

A dissertation submitted in partial fulfillment
of the requirements for the degree of
Doctor of Philosophy in Microelectronics-Photonics

by

Sattar H. Sweilim Al-Kabi
University of Baghdad, Iraq
Bachelor of Science in Physics, 2002
University of Baghdad, Iraq
Master of Science in Physics (Molecular and Laser), 2006

August 2017
University of Arkansas

This dissertation is approved for recommendation to the Graduate Council.

Dr. Shui-Qing (Fisher) Yu
Dissertation Director

Dr. Gregory J. Salamo
Dissertation Director

Dr. Hameed A. Naseem
Committee Member

Dr. Simon Ang
Committee Member

Dr. Rick Wise
Ex-Officio Member

The following signatories attest that all software used in this dissertation was legally licensed for use by Sattar H. Sweilim Al-Kabi for research purposes and publication.

___________________________________ _____________________________________

Sattar H. Sweilim Al-Kabi, Student Dr. Shui-Qing (Fisher) Yu, Dissertation Director

This dissertation was submitted to http://www.turnitin.com for plagiarism review by the TurnItIn company's software. The signatories have examined the report on this dissertation that was returned by TurnItIn and attest that, in their opinion, the items highlighted by the software are incidental to common usage and are not plagiarized material.

___________________________________ _____________________________________

Dr. Rick Wise, Program Director Dr. Shui-Qing (Fisher) Yu, Dissertation Director

Abstract

Silicon-based materials and optoelectronic devices are of great interest as they could be monolithically integrated in the current Si complementary metal-oxide-semiconductor (CMOS) processes. The integration of optoelectronic components on the CMOS platform has long been limited due to the unavailability of Si-based laser sources. A Si-based monolithic laser is highly desirable for full integration of Si photonics chip. In this work, Si-based germanium-tin (GeSn) lasers have been demonstrated as direct bandgap group-IV laser sources. This opens a completely new avenue from the traditional III-V integration approach.

In this work, the material and optical properties of GeSn alloys were comprehensively studied. The GeSn films were grown on Ge-buffered Si substrates in a reduced pressure chemical vapor deposition system with low-cost $SnCl_4$ and GeH_4 precursors. A systematic study was done for thin GeSn films (thickness < 200 nm) with Sn compositions from 0 to 12%, and for thick GeSn films (thickness > 400 nm) with Sn composition 5 to 17.5%. The room temperature photoluminescence (PL) spectra were measured that showed a gradual shift of emission peaks towards longer wavelength as Sn composition increases. Strong PL intensity and low defect density indicated high material quality. Moreover, the PL study of n-doped samples showed bandgap narrowing compared to the unintentionally p-doped (boron) thin films with similar Sn compositions.

Finally, optically pumped GeSn lasers on Si with broad wavelength coverage from 2 to 3 μm were demonstrated using high-quality GeSn films with Sn compositions up to 17.5%. The achieved maximum Sn composition of 17.5% broke the acknowledged Sn incorporation limit using similar deposition chemistry. The highest lasing temperature was measured at 180 K with an active layer thickness as thin as 270 nm. The unprecedented lasing performance is due to the

achievement of high material quality and a robust fabrication process. The results reported in this work show a major advancement towards Si-based electrically pumped mid-infrared laser sources for integrated photonics.

Acknowledgements

My sincere gratitude goes first to my advisor, Dr. Shui-Qing (Fisher) Yu for all his guidance, motivation, encouragement, and immense knowledge. Through my entire study, his support and patience were there to help me achieving better training and experience as a research scientist.

My appreciation also extends to my dissertation committee members: Dr. Greg Salamo, Dr. Hameed Naseem, Dr. Simon Ang, and Dr. Rick Wise, for serving as my committee members their insightful comments and encouragement. My special thanks go to Prof. Ken Vickers who supported and assisted me through many stages of my study.

I would like to thank Dr. Du from my deep heart for his help and encouragement. Also, I would like to thank both Dr. Mosleh and Dr. Ghetmiri for their countless help and support and being great friends. Special thanks to my colleagues Yiyin, Thach, Huong, Wei, P.C., Matt, and all other our research group members for their help, suggestions, and comments.

I want to express my deep appreciation for my family for their great help, support, and they have always encouraged me to achieve my goals.

This work was supported by the National Science Foundation (NSF) under DMR-1149605, the Defense Advanced Research Projects Agency (DARPA) under W911NF-13-1-0196, the Air Force Office of Scientific Research (AFOSR) under FA9550-14-1-0205, Arktonics, LLC (AFOSR, FA9550-16-C-0016), NASA EPSCoR (NNX15AN18A), Minister of High Education and Scientific Research – Iraq, University of Wasit, Kut, Iraq.

Dedication

This edition of the dissertation is dedicated to my beloved parents, to Sayed Jassim, to my brothers, sisters, and friends.

Table of Contents

1. Chapter 1: Introduction 1

1.1 Motivation 1

1.2 Indirectness of group IV semiconductor bandgap 2

1.3 Group IV lasers 3

1.4 Germanium-tin direct bandgap 5

1.5 Germanium tin lasers 6

1.6 Fundamentals of semiconductor lasers 9

1.6.1 Semiconductor laser system 9

1.6.2 Generation and recombination processes 10

1.6.3 Absorption, spontaneous, and stimulation emission 14

1.6.4 Gain, loss, and threshold conditions 15

1.6.5 Light power output and efficiency 18

1.7 Research statement 19

1.8 Outline of dissertation 20

2. Chapter 2: Growth, Fabrication and Experimental Setup 21

2.1. Growth and material characterization 21

2.1.1 Growth information 21

2.1.1.1 Thin and doped GeSn films 21

2.1.1.2 Thick GeSn films 21

2.1.2. Material characterization 22

2.1.2.1Transmission electron microscopy (TEM) 22

2.1.2.2 X-ray Diffraction (XRD) 23

2.1.2.3 Secondary ion mass spectrometry 24
2.1.3 Optical characterization and setups 24
2.1.3.1 Raman spectroscopy and Raman setup 25
2.1.3.2 Photoluminescence characterization and PL setup 27
2.2. Fabrication processes for devices 30
2.2.1. Device design 30
2.2.2. Wet etching 31
2.2.3. Dry etching 32
2.3. Lapping and cleaving processes 33
2.4. Optical pumping setup and device characterization 34
3. Chapter 3: Optical Characterization of Thin GeSn 36
3.1. Introduction 36
3.2. Material characterization 37
3.3. Raman spectroscopy measurements 39
3.4. Photoluminescence of thin GeSn films 41
3.5. The impact of n-type doping on GeSn bandgap 46
3.6. Summary 48
4. Chapter 4: Thick GeSn Films with High Quality and Material Gain 49
4.1. Introduction 49
4.2. Material characterization of thick GeSn films 50
4.3. Optical characterization 53
4.4. The impact of thickness of the GeSn films on the material gain and intensity enhancement 57

4.5. Summary 59

5. Chapter 5: Initial Optically Pumped GeSn Edge-Emitting Lasers 60

5.1. Introduction 60

5.2. Material and optical characterization 60

5.2.1 Material characterization 60

5.2.2 Photoluminescence characterization 62

5.3. Fabrication process and devices preparation 63

5.4. GeSn laser devices measurements 64

5.5. Evidence of achieving GeSn lasers 65

5.6. Band structure and modes profiles 67

5.7. GeSn laser device performance 69

5.8. Summary 72

6. Chapter 6: Systematic Study of GeSn Edge-Emitting Lasers 73

6.1. Introduction 73

6.2. Material and optical characterization 73

6.2.1 Growth information 73

6.2.2 Material characterization 75

6.2.2 Photoluminescence characterization 77

6.3. Devices fabrication and measurements conditions 79

6.4. Lasing at different Sn compositions 81

6.5. GeSn lasing threshold 82

6.6. The impact of GeSn film thickness on the GeSn lasers 84

6.7. Power dependent of lasing spectrum 86

6.8. Study the modes of GeSn lasers....87

6.9. Temperature operation of edge-emitting GeSn lasers....90

6.10. Band diagram calculation....93

6.11. Lasing mode pattern calculation....94

6.12. The performance of GeSn laser devices....95

6.13. Summary....95

7. Chapter 7: Summary and Future Work....97

7.1. Summary....97

7.1.1 Thin GeSn films....97

7.1.2 Doped thin GeSn films....97

7.1.3 Thick GeSn film....98

7.1.4 Optically pumped edge-emitting GeSn laser....98

7.1.5 Summary of Key Observations....100

7.2. Future work....101

7.2.1 Optimize the bulk GeSn lasers using DHS....101

7.2.2 Study of doped GeSn lasers....102

7.2.3 Quantum Wells GeSn lasers....102

7.2.4 Electrically injected GeSn lasers....103

References....104

Appendix A. Knife-Edge Method to Calculate the Gaussian Beam Size....114

Appendix B: Description of Research for Popular Publication....115

Appendix C. Executive Summary of Newly Created Intellectual Property....117

Appendix D. Potential Patent and Commercialization Aspects of Listed Intellectual Property

Items..118

D.1 Patentability of Intellectual Property (Could Each Item Be Patented) 118

D.2 Commercialization Prospects (Should Each Item Be Patented) 118

D.3 Possible Prior Disclosure of IP 118

Appendix E. Broader Impact of Research 119

E.1. Applicability of Research Methods to Other Problems..119

E.2. Impact of Research Results on U.S. and Global Society 119

E.3. Impact of Research Results on the Environment 119

Appendix F. Microsoft Project for PhD MicroEP Degree Plan..120

Appendix H. Identification of All Software Used in Research and Dissertation Generation......121

Appendix I. All Publications Published, Submitted, and Planned...123

I.1. List of peer-reviewed published works 123

I.2. List of conference proceedings and publications 124

I.3. List of submitted works..125

I.4. List of planned works...126

Appendix J. Taken from Author's Published Works...127

List of Figures

Figure 1.1. Band structure in momentum space for Ge 3

Figure 1.2. Optically pumped edge-emitting Ge laser using 1064 nm laser to show the spectra of spontaneous, lasing threshold, and laser emission SEM image of device and setup diagram [5] 5

Figure 1.3 Evidence of GeSn a direct bandgap....6

Figure 1.4 (a) Schematic of designed GeSn MQW. (b) Model gain of GeSn MQW as a function of injected surface density [80] 7

Figure 1.5. Optically pumped GeSn waveguide laser with (a) laser spectrum, (b) L-L curves for different cavity lengths, and (c) Fabry-Perot modes for different devices [21]....8

Figure 2.1. TEM image showing the different layers of GeSn/GeSn/Ge/Si structure of thick $Ge_{0.919}Sn_{0.081}$ sample [92]....22

Figure 2.2. XRD measurements of relaxed thick $Ge_{0.882}Sn_{0.118}$ sample....23

Figure 2.3. SIMS results show the mole fraction versus depth of Si, Ge, and Sn in a $Ge_{0.826}Sn_{0.174}$ sample 24

Figure 2.4. Schematic diagram of Raman spectroscopy setup 26

Figure 2.5. Raman shifts for thick relaxed GeSn samples from 7.3% to 17.5% at room temperature 27

Figure 2.6. Schematic diagram of PL setup with several lasers sources 29

Figure 2.7. Normalized PL intensity of different Sn compositions from 0 to 17.5 of GeSn alloys at 300 K 30

Figure 2.8 Schematic diagram showing the fabricated GeSn waveguides using the designed mask with several widths (1, 2, 3, 4, and 5 μm) 31

Figure 2.9. SEM images using wet etching method for the $Ge_{0.882}Sn_{0.118}$ laser device for both sidewalls and facet....32

Figure 2.10. SEM images using dry etching method for the $Ge_{0.903}Sn_{0.097}$ laser device for both sidewalls and facets 33

Figure 2.11. Schematic diagram illustrating (a) optical pumping setup for laser device measurements and (b) how a GeSn laser device was uploaded and measured insidethe cryostat 35

Figure. 3.1. Cross-sectional TEM image of Si/Ge/$Ge_{0.9}Sn_{0.1}$ film 37

Figure 3.2. 2θ-ω XRD scan from (004) plane for (a) unintentionally doped and (b) n-type doped samples 38

Figure 3.3. Raman spectroscopy for (a) unintentionally doped and (b) n-type doped samples 40

Figure 3.4. (a) Normalized PL spectra of the unintentionally doped GeSn thin films. (b) PL peak position attributed to the bandgap as a function of Sn composition [16] 42

Figure 3.5. Temperature-dependent PL for GeSn samples with several Sn compositions...........45

Figure 3.6. Comparison of the normalized PL spectra between the unintentionally doped and n-type doped GeSn samples with Sn compositions 46

Figure 3.7. Temperature-dependent PL spectra for n-type doped GeSn samples with several Sn compositions..47

Figure 4.1. Cross-sectional view TEM image of sample C, $Ge_{0.9195}Sn_{0.0805}$ 50

Figure 4.2. The 2θ-ω XRD scan from (004) plane for GeSn samples..53

Figure 4.3. Normalized PL spectra of samples A-E at 300 K..54

Figure 4.4. Comparison of the PL spectra between the GeSn thin and thick films at 10 K and 300 K..56

Figure 4.5. Temperature-dependent PL spectra from 300-10 K..57

Figure 4.6. (a) Temperature-dependent PL spectra of sample E using 1064 nm high-frequency laser. The PL of Ge is also plotted for comparison (b) Pumping power-dependent PL of sample E at 10 K..58

Figure 5.1. (a) Cross-sectional view TEM image showing two distinct GeSn layers. (b) RSM contour plot showing the superposition of bottom and top GeSn layers.......................61

Figure 5.2. L-L curves of the 600 μm-long edge-emitting device at 10 and 90 K. Inset: (top left) SEM image of ridge waveguide device; (top right) Temperature-dependent integrated PL intensity; (bottom) Optically pumped lasing spectra at 90 K................................63

Figure 5.3. L-L curves of the 300 μm-long edge-emitting device at 10 K. Inset: The high-resolution spectra under 2× and 5× threshold pumping power [85].....................................66

Figure 5.4. L-L curves of the 1100 μm-long edge-emitting device taken at the temperatures from 10 to 110 K. Inset: Laser threshold versus temperature for the purpose of fitting T0 [85] ..67

Figure 5.5. (a) Band structure of the sample at 300 K (b) Profile of the fundamental transverse electric (TE0) mode. Inset: cross-sectional profile of TE0 mode [85] 68

Figure 6.1 Sn composition and GeSn layers for each sample discussed in Chapter 6 75

Figure 6.2. (a) Cross-sectional TEM image showing two distinct GeSn layers of Sample J. (b) EDX plot presents the thickness and layer composition of Ge buffer, and three GeSn layers with different thickness and Sn % of Sample J 76

Figure 6.3. Normalized PL spectra of samples A-J at (a) 300 K and (b) 10 K.............................78

Figure 6.4. Temperature-dependent PL spectra of GeSn for (a) Sample A, (c) Sample J. The corresponding FWHM and integrated PL intensity against temperature are plotted in (b) Sample A, (d) Sample J 79

Figure 6.5. SEM images for GeSn laser devices for facets and sidewalls...................................80

Figure 6.6. GeSn laser performance characterization...83

Figure 6.7. (a) L-L curves of Samples A, B, C, D, E, F, I and J versus power density (kW/cm2) at 77 K. (b) L-L curves of Sample B at 10 K...84

Figure 6.8 L-L curves of Samples B, D, E, and I versus power density (kW/cm^2) at 77 K 85

Figure 6.9. The spectrum measurements of Sample C at 10 K..86

Figure 6.10. The GeSn laser modes at low resolution for Sample I 88

Figure 6.11. The modes measurements of GeSn lasers. 90

Figure 6.12. Temperature-dependent L-L curves presented for samples (a) C, (c) D, and (e) J. The characteristic temperature shown for samples (b) C, (d) D, and (f) J....................................92

Figure 6.13. Band diagram calculation for Samples (a) D and (b) J at 300 K..............................93

Figure 6.14. Calculated pattern of the fundamental transverse electric mode..............................94

List of Tables

Table 3.1. Summary of measurement results of unintentionally and doped thin GeSn films 39

Table 3.2. Raman shift of Ge-Ge and Ge-Sn bonds for unintentionally and n-type doped sample 41

Table 4.1. Summary of GeSn sample, composition, thickness and relaxation [106] 51

Table 6.1. Summary of GeSn samples information including Ge buffer thickness, thickness, and composition of each layer of GeSn, and Ge cap thickness 74

Table 6.2. Summary of GeSn laser devices including a lasing wavelength at 77 K, the threshold value at 77 K, temperature characteristic, and temperature operation...........................82

Chapter 1. Introduction

1.1 Motivation

Silicon-based materials and their optoelectronic devices are of great interest due to the scalable incorporation with current Si complementary metal-oxide-semiconductor (CMOS) processes [1]. The development of optoelectronic integration with CMOS has long been limited by the unavailability of monolithic Si-based laser sources [2-3]. Tremendous efforts have been made to overcome this technical barrier. An all-Si Raman laser was reported in 2005 [4] which relies on stimulated Raman scattering rather than band-to-band transition. The development of Ge techniques has led to optically and electrically pumped Ge lasers [5-6]. The energy difference of ~136 meV between the direct Γ-valley and the indirect L-valley was compensated by heavily n-type doping or tensile strain Ge layer, which either resulted in a high threshold or technical fabrication difficulties [7, 8]. The hybrid integration of III-V lasers on Si has been investigated extensively [9-11]. The III-V materials feature efficient light emission, and the recent hybrid integration-based results show significantly improved material quality [12-13]. This route requires either a wafer-bonding process or direct growth of III-V on Si techniques.

Among the various material systems that could be integrated on Si, the $Ge_{1-x}Sn_x$ alloy has attracted much attention recently due to the following reasons: (1) capability of monolithic integration on Si [14]; (2) availability of direct bandgap material [15]; and (3) tunable bandgap covering broad shortwave- and mid-infrared (IR) wavelength range [16].

Theoretically, by incorporating Sn into Ge lattice, the direct and indirect bandgap energies could be reduced and eventually a direct bandgap material is attainable [17-20]. This was experimentally proven by the report of the direct bandgap GeSn in 2014 [15], followed by the demonstration of an optically pumped GeSn laser in 2015 [21]. Moreover, for the past five

years, the GeSn-based optoelectronic devices including light emitting diodes (LEDs), photoconductive detectors, photodiode detectors, and modulators have been investigated by research groups all over the world [22-28] indicating the great potential of the GeSn technique in the area of Si photonics. Particularly, for the GeSn photodetector, some results [29- 30] indicated that a key figure of merit, such as specific detectivity, could potentially get close to that of the current market-dominating infrared detectors such as InGaAs and InAs [31, 32].

The inordinate characteristics of GeSn, such as directness and tunability of the bandgap, reaching high Sn composition, high-quality materials, and covering a broad range of wavelength, make GeSn the best candidate for light emitting devices especially lasers.

1.2 Indirectness of bandgap group IV semiconductor

Semiconductor materials include two types: direct and indirect bandgap. Group III-V and some of group II-VI materials are direct bandgaps. The energy level of direct material is located vertically at the lowest point between the conduction and valence bands in the momentum (k) space. The transition occurs between Γ Valley and valence band. However, the nature of group IV is indirect bandgap. There are Γ and L and/or X valleys in the conduction band. Therefore, the transition occurs from the lowest level of energy, which is L valley as shown in Figure 1.1. Among group IV elements, Ge is the best candidate to become a direct material due to the lowest difference between Γ and L valleys – about 136 meV. Several techniques were used to shrink the bandgap of Ge and reduce the Γ valley to be lower than the L point. The first technique used was applying tensile strain on Ge layer to reduce the distance between Γ and the valence band. The second method was heavily doped Ge material. The doping reduces the direct bandgap to lower than the indirect bandgap which depends on the level of doping. Many emitting devices

have been demonstrated demonstrated using direct Ge material [34-35].

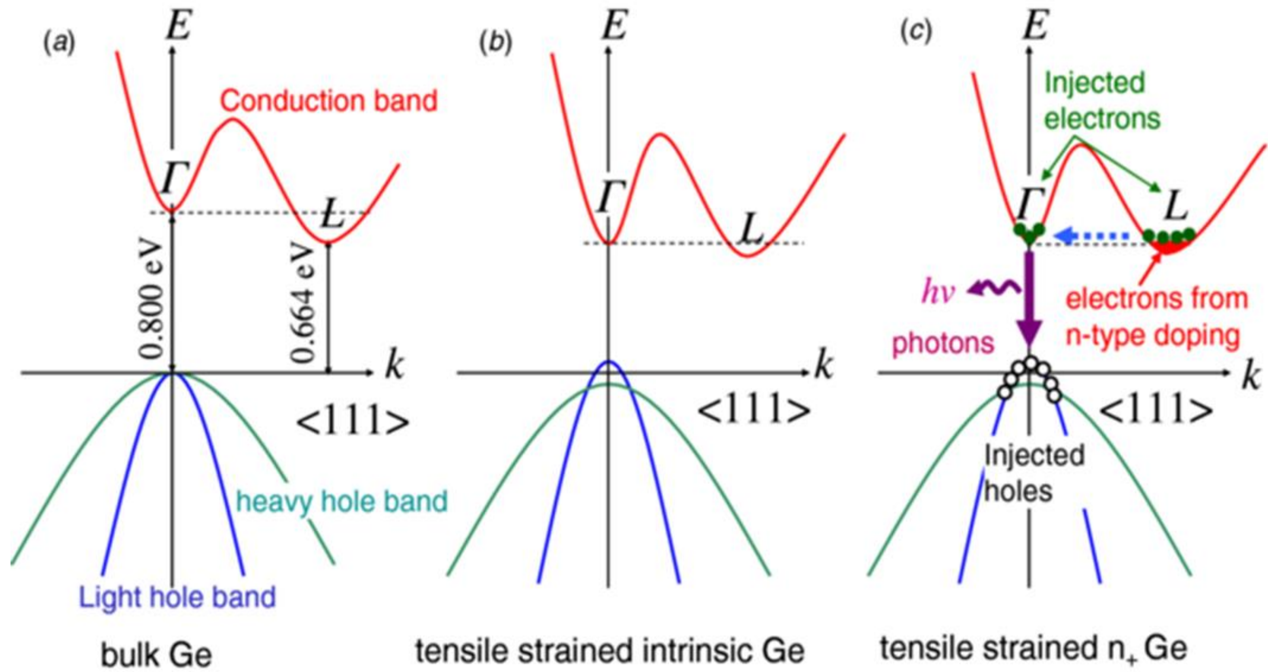

Figure 1.1. Band structure in momentum space for Ge. (a) Indirect bandgap, (b) indirect bandgap of Ge with tensile strain, and (c) direct bandgap under strain, doping, or alloying with Sn [33].

Nonetheless, neither method is desirable. The tensile strain affects the structure of Ge material and increases defect levels. Also, the doping process is costly and it is not appropriate for large scale. These methods, which are hindered by technical fabrication difficulties, are less than satisfactory for the community.

1.3 Group IV lasers

The Si-based laser is desirable for several reasons. First, the laser can be integrated with optoelectronics and electronics components due to its compatibility with COMS processing. Second, monolithic growth on Si substrates can reduce the cost much more than other semiconductor lasers grown on expensive substrates. Third, the emitting light of these lasers

covers the desirable range of wavelength in short and mid-infrared. Finally, they can be electrically pumped to avoid using an extra light source [36]. The development of Si photonics has suffered from the indirect bandgap of Si, Ge, and their alloys, which led to low efficiency of group IV-based light emitters. Various routes have been explored to improve the performance of light emitters on Si.

The early investigations on Si-based laser were done on Si with different methods including porous silicon [37], erbium-doped silicon [38], and silicon Raman lasers with both pulse and continuous operation [39-41]. These methods do not rely on bandgap emission and cannot be operated under direct electrical pumping. Moreover, the efficiency of these lasers is very low due to the high loss inside the lasing cavity. Then, more attention was paid in the last few years to integration of III-V lasers on Si [9-10]. The III-V lasers show high efficiency, but the growth of III-V materials on Si substrate is a challenge due to crystal structure differences. Recently, new methods of hybrid integration were applied to improve material quality [11-13, 42-44]. Moreover, Ge laser on Si substrate has attracted several groups to investigate and demonstrate Ge lasers with different techniques. In order to obtain lasing from Ge, the Ge must be a direct bandgap material. As discussed previously in Section 1.2, the Ge becomes a direct bandgap material by applying strain and/or heavy doping. Both optically and electrically injected Ge lasers were demonstrated in the last decade [45-52]. Figure 1.2 presents the optically pumped edge-emitting Ge laser.

Three spectra at different pumping powers show the spontaneous, threshold, and laser emission of Ge laser (Figure 1.2). The n-type doped concentration was $1x10^{19}$ cm^{-3} and with 0.24% applied tensile strain. The direct bandgap energy of Ge is 0.8 meV which corresponds to the wavelength of 1.55 μm, the most common wavelength in telecommunications.

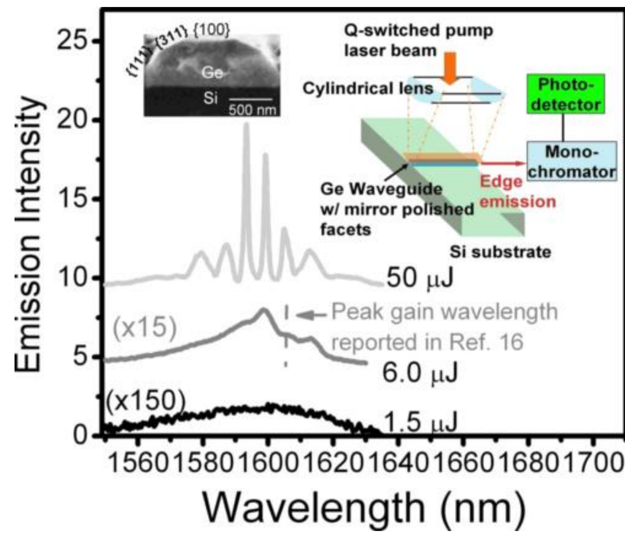

Figure 1.2. Optically pumped edge-emitting Ge laser using 1064 nm laser to show the spectra of spontaneous, lasing threshold, and laser emission SEM image of device and setup diagram [5].

1.4 Germanium-tin direct bandgap

Germanium is considered a potential candidate for photonic devices due to the lowest energy difference between its Γ-conduction bands and valence bands, which is about 136 meV. Alloying Sn to Ge reduces the energy difference between L and Γ-valleys, which leads to change in the GeSn alloy to become direct bandgap material; this depends on Sn composition and strain of the GeSn film. During the early 1990s, many theoretical studies indicated that GeSn could be a direct bandgap material [53-55]. Later, many research groups studied alloying Sn into Ge theoretically and experimentally [56-59]. However, the direct GeSn bandgap was experimentally reported in 2014 [15]. During the last decade, GeSn was investigated for basic material study and different types of devices. GeSn devices such as photodetectors [60-67], GeSn modulators [68, 69], and light emitting diodes [70-76] have been explored, which make up a complete set of components for Si photonics. For these prototype devices, the material characteristics have become the decisive factor for the performance of the device. Figure 1.3 presents evidence of

GeSn as a direct bandgap at a Sn composition around 10%. The linewidth is reduced as the Sn composition increases as shown in Figure 1.3(a). The three samples were selected with a composition of 8, 9, and 10% Sn. The sample with 10% Sn shows the lowest FWHM, and it was reduced as the temperature decreased. Figure 1.3(b) presents the bandgap of GeSn theoretically and experimentally from different groups. From 0 to 7% Sn, there are clearly two peaks that are corresponding to the indirect and direct transition. At 8-9% Sn composition, there is overlap between direct and indirect bandgap with broad spectra. However, there is only one peak with narrower linewidth.

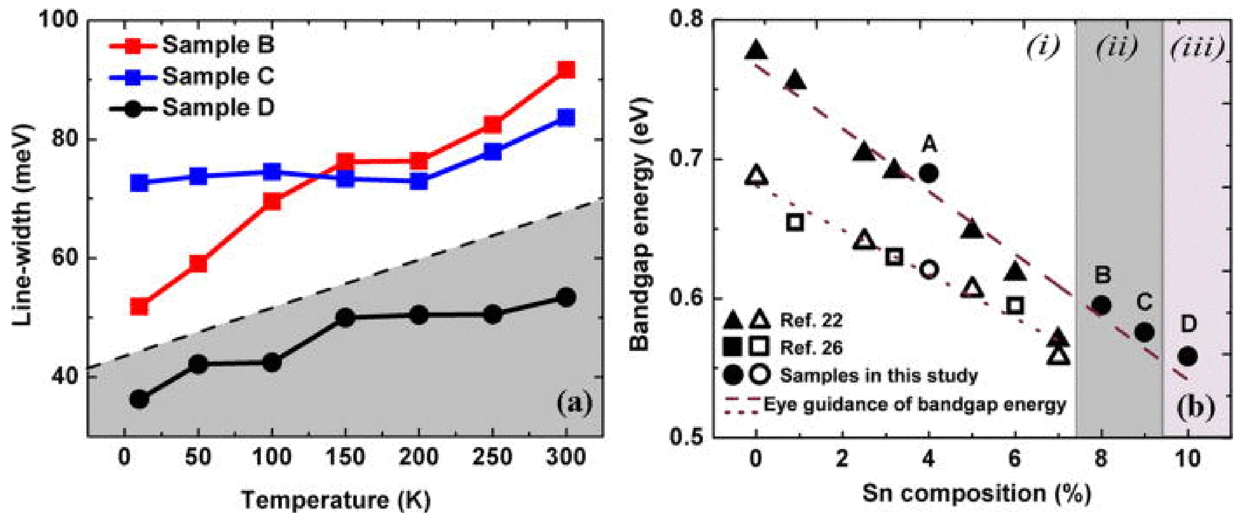

Figure 1.3 Evidence of GeSn a direct bandgap. (a) FWHM is reduced with increasing Sn composition up to 10%. (b) Bandgap of GeSn versus Sn composition [15].

1.5 Germanium tin lasers

Si-based monolithically grown lasers have attracted many research groups especially after proving the concept that GeSn can be a direct bandgap material with alloying Sn at a particular Sn percentage. The GeSn laser was theoretically investigated for several types of structures such as double heterostructure (DHS), and quantum wells (QWs). Sun et al. theoretically studied a SiGeSn/GeSn/SiGeSn DHS design for electrically pumped devices. The

modeling and simulation showed that GeSn could be lased at a temperature range of 100 to 200 K. The lasing threshold of this designed structure was too high at 300 K [77]. Later, the same team designed and calculated GeSn/SiGeSn multi-QW with type-I band diagram to operate at room temperature (RT). The Sn composition was selected to be 10% as a direct bandgap and the barriers with compositions of $Ge_{0.75}Si_{0.1}Sn_{0.15}$. The lasing wavelength of this design was 2.3 µm. The model gain increased with pumping density and increasing the number of wells due to increasing the optical confinement [78-79]. Chang et al. theoretically studied MQW of GeSn/SiGeSn lasers with Sn composition at 16%. The barriers were with both n-doped $Si_{0.08}Ge_{0.78}Sn_{0.14}$ and p-doped $Si_{0.08}Ge_{0.78}Sn_{0.14}$ as a cap. The barriers and QWs were grown on a strain-relaxed $Ge_{0.88}Sn_{0.12}$ buffer. Figure 1.4 presents the GeSn MQW structure and the model gain at different carrier densities.

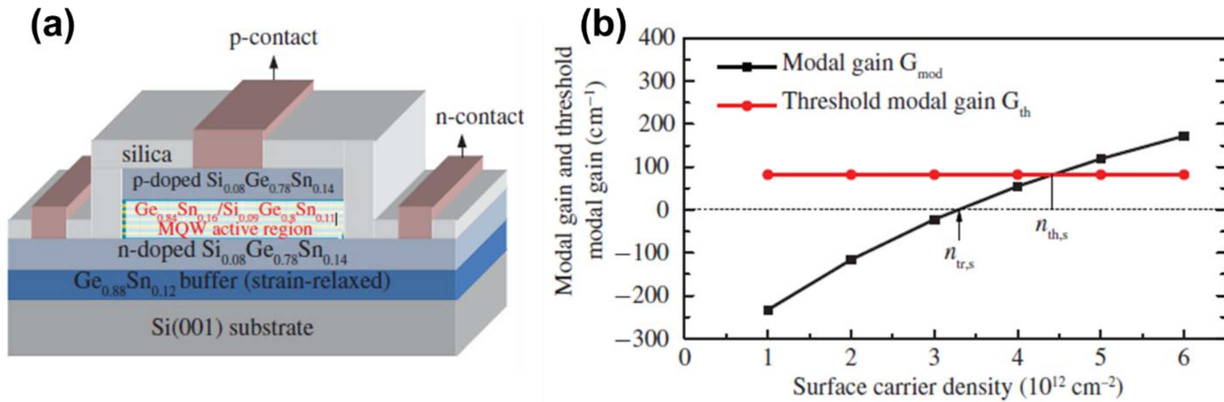

Figure 1.4 (a) Schematic of designed GeSn MQW. (b) Model gain of GeSn MQW as a function of injected surface density [80].

The calculated lasing wavelength of this structure was 2.883 µm. For 500 µm of cavity length, the threshold carrier density was 4.3 x 10^{18} cm^{-3}, and lasing threshold current was 9.78 kA/cm^3 [80]. Several other groups investigated the modeling and simulation of GeSn lasers to estimate lasing wavelength, threshold, mode gain, loss, lifetime, and temperature operation [81-83].

The first optically pumped GeSn laser demonstrated experimentally was reported by Wirths et al. in 2015 [21]. A direct bandgap GeSn laser with 12.6% Sn composition and 2.25 µm of lasing wavelength was achieved. The lasing threshold of 1 mm of cavity length was 325 kW/cm^2 at 20 K with temperature operation at 90 K as shown in Figure 1.5 [21]. Figure 1.5(a) presents the spectrum of GeSn laser device at different power density for 1 mm cavity length. The intensity increases rapidly as the power density increases. The temperature-dependent PL show that the temperature operation of the laser is 90 K. Figure 1.5(b) illustrates the light-in-light-out (L-L) curves at different cavity lengths that indicate the intensity increases for longer cavity length. Inset of Figure 1.5(b) shows the FWHM at various power density. The FWHM is large before lasing and then reaches the minimum value at lasing. Then it slightly increases with increasing the power density due to heating. Figure 1.5(c) presents the Fabry-Perot cavity modes for 250 and 500 µm of cavity length at power density 500 kW/cm^2 and 20 K.

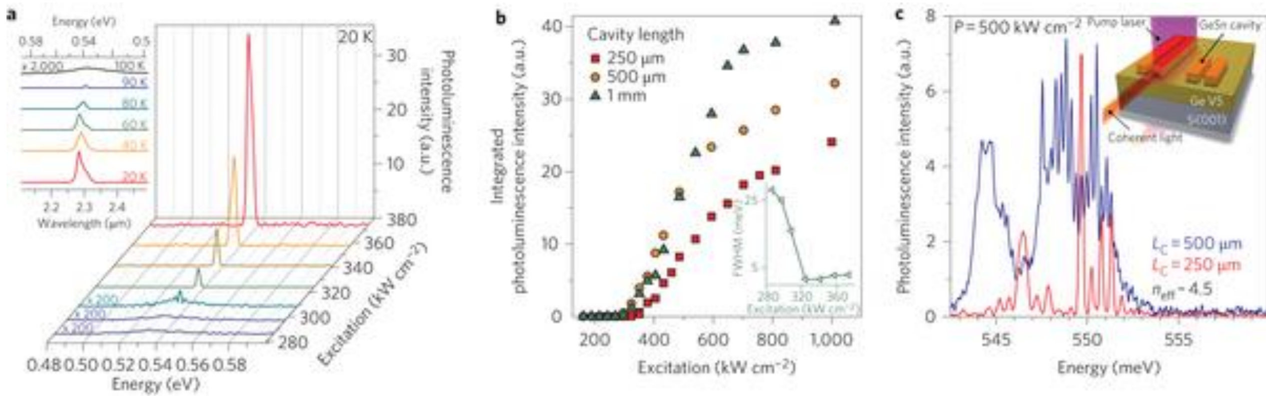

Figure 1.5. Optically pumped GeSn waveguide laser with (a) laser spectrum, (b) L-L curves for different cavity lengths, and (c) Fabry-Perot modes for different devices [21].

The same group demonstrated an optically pumped GeSn microdisk lasers with lasing threshold 220 kW/cm^2 and temperature operation 140 K [84]. After that, an optically pumped GeSn laser with 2.5 µm of lasing wavelength and 110 K of temperature operation was reported by Al-Kabi et al. in 2016 [85]. There was a significant reduction of lasing threshold, 68 kW/cm^2

at 10 K and with lower Sn composition, 10.9%, compared to the first GeSn laser reported in Ref. 21.

1.6 Fundamentals of semiconductor lasers

Understanding the concepts of the laser is very significant to explain any experimental results of lasers. The word LASER means "Light Amplification by Stimulated Emission of Radiation." There are several requirements to build a laser system. These requirements are gain medium, a pump source, and optical resonator (optical cavity). Lasers are classified according to the gain medium that is used to generate lasing, such as solid, liquid, gas, and semiconductor lasers. In this study, the background mainly explains how semiconductor lasers work.

Since the first semiconductor laser (GaAs) was demonstrated in 1962, semiconductor lasers have attracted numerous researchers to investigate and develop these lasers. The unique characteristics of semiconductor lasers, such as availability of materials, small size, low cost, low power input, a variety of engineered structures, and covering a wide range of wavelengths make them desirable for many applications [86].

1.6.1 Semiconductor laser system

As with other types of lasers, semiconductor laser system involves a gain medium, an optical resonator, and a pump source. First, the gain medium is semiconductor materials that are alloyed with two or more semiconductor elements. Second, one of the differences between a semiconductor and other types of lasers is the optical cavity. The optical cavity in many lasers includes two mirrors with different reflectivity to amplify stimulated radiation that is generated from the gain medium. However, the optical resonator of the semiconductor laser is different in

that it can be made by cleaving both sides (facets) of the semiconductor waveguide. The reflectivity of facets depends on the refractive index of the gain materials and outside the waveguide such as air. Sometimes facets are polished to increase the reflectivity inside the cavity to reduce the loss. Third, there are two types of pumping that are used to pump semiconductor lasers; these are optical and electrical pumping. The usage of these pumping types depends on how the semiconductor laser structure is designed and fabricated.

There are several types of material structures that are used for a semiconductor laser: for instance, bulk, quantum well(s), nanowire, and quantum dots. These laser structures are designed to be used for different reasons and applications. The lasing wavelength, threshold, temperature operation, power consumption, and size of devices are the main reasons for using different structures of semiconductors.

Moreover, there are two types of device structures in semiconductor lasers. These are edge- and surface-emitting laser devices that depending on how the laser light is emitted from laser devices. For edge-emitting laser devices, the light pump source is incident perpendicular to the top of the device and laser light is emitted from one of the edges of devices and parallel to the surface of the device. However, emitted laser light from the surface of the device and pump light incident are diagonal at a particular angle which increases the output emitted light from the surface. Also, surface-emitting laser device can be electrically injected. Edge-emitting laser devices with bulk materials were chosen to be studied in this research study [87-89].

1.6.2 Generation and recombination processes

Understanding the physics of the processes inside the active region and how it is reacting with incident photons it is very significant to explain how the laser is generated and behaves.

First, there is a need to comprehend the generation and recombination processes inside the gain medium. The carrier generation and recombination processes divide into the radiative and nonradiative processes. The radiative generation-recombination processes create photons. However, the nonradiative processes do not generate photons, and it is due to defects (Shockley-Read-Hall), impurities, and Auger processes. The energy that is produced by these nonradiative processes increases the degradation of the device and excited phonons. To calculate the generation and recombination rate, the following equations are used: under the assumption of optical rate generation rate, $\mathrm{G_n}$is uniform

$$\mathrm{G_n} = \mathrm{G_n(t)}, \quad \text{(Equation 1.1)}$$

and the total recombination rate $R(n)$ is,

$$\mathrm{R(n) = An + Bn^2 + \ Cn^3 = \frac{n}{\tau(n)}} \quad \text{(Equation 1.2)}$$

where An is nonradiative recombination (HSR) at defects, $\mathrm{Bn^2}$ is the radiative recombination from spontaneous emission of photons, $\mathrm{Cn^3}$ is the Auger processes. From Equation 1.2, the carrier lifetime can be calculated,

$$\mathrm{\tau(n) = (An + Bn^2 + \ Cn^3)^{-1}}, \quad \text{(Equation 1.3)}$$

where $\mathrm{\tau(n)}$the carrier lifetime, and B is the bimolecular recombination coefficient. The carrier lifetime equation includes two parts; the first part is related to the radiative recombination,

$$\mathrm{\tau_r = \frac{1}{Bn}}, \quad \text{(Equation 1.4)}$$

where $\mathrm{\tau_r}$ is the radiative lifetime. The second part is for nonradiative recombination,

$$\mathrm{\tau_{nr} = \frac{1}{A + Cn^2}}, \quad \text{(Equation 1.5)}$$

where $\mathrm{\tau_{nr}}$ is the nonradiative lifetime.

Therefore, the total recombination rate depends on carrier concentration and total lifetime,

$$R(n) = \frac{n}{\tau(n)}. \qquad \text{(Equation 1.6)}$$

The carrier concentration at any time is given by:

$$\frac{dn(t)}{dt} = G_n(t) - R(n). \qquad \text{(Equation 1.7)}$$

At the steady state $G_n(t) = G_0$. The amount of excess carrier concentration is,

$$n_c = G_0 \tau(n), \qquad \text{(Equation 1.8)}$$

or

$$G_0 = \frac{n_c}{\tau_n}. \qquad (\textit{Equation } 1.9)$$

The carrier concentration in the active region is determined by the rate equation:

$$\frac{dn(t)}{dt} = \eta_{in} \frac{J(t)}{qd} - R(n) - v_g\, g(n) S(t). \qquad \text{(Equation 1.10)}$$

The first term on the right-hand accounts for the carrier injection into the active region with a thickness d, where η_{in} is the intrinsic quantum efficiency, J is the current density, d is thickness of active region, and q is electron charge. The second term, $R(n)$, accounts for the carrier recombination due to both radiative (spontaneous emission) and nonradiative processes. The last term is the carrier loss due to the stimulated emission process; S(t) is the photon density (the number of photons per unit volume), v_g is the group velocity [$v_g = c/n_g$] where n_g is the group index, and c is the speed of light.

Intrinsic quantum efficiency (η_{in}) is the ratio of the radiative rate to the total recombination rate. The intrinsic quantum efficiency can be calculated using the following equation:

$$\eta_{in} = \frac{\frac{1}{\tau_r}}{\frac{1}{\tau_r} + \frac{1}{\tau_{nr}}} = \frac{\tau_{nr}}{\tau_r + \tau_{nr}} \quad \text{(Equation 1.11)}$$

At steady state below threshold, the carrier concentration n is determined by injected density,

$$\eta_{in} \frac{J}{qd} = \frac{n}{\tau}, \quad \text{(Equation 1.12)}$$

$$n = \eta_{in} \frac{J\tau}{qd}. \quad \text{(Equation 1.13)}$$

A, B, and C coefficients (from Equation 1.2) for lasers structures can be estimated from experimental data or theoretical model.

The total electron and hole concentration in the active region can be determined using the following equations. The quasi-Fermi level F_n in active region is determined by,

$$n = N_c F_{1/2}\left(\frac{F_n - E_c}{K_B T}\right), \quad \text{(Equation 1.14)}$$

where F_n is the quasi-Fermi level.

$$N_c = 2\left(\frac{m_e^* K_B T}{2\pi\hbar^2}\right)^{3/2} = 2.51 * 10^{19} \left(\frac{m_e^*}{m_o} \frac{T}{300}\right)^{3/2} cm^{-3}, \quad \text{(Equation 1.15)}$$

and

$$p = N_v F_{1/2}\left(\frac{E_c - F_p}{K_B T}\right), \quad \text{(Equation 1.16)}$$

where F_p is the quasi-Fermi level.

$$N_v = 2\left(\frac{K_B T}{2\pi\hbar^2}\right)^{3/2} \left(m_{hh}^{*\,3/2} + m_{lh}^{*\,3/2}\right) = 2.51 * 10^{19} \left(\frac{m_h^*}{m_o} \frac{T}{300}\right)^{3/2} cm^{-3}, \quad \text{(Equation 1.17)}$$

From known electron and hole concentrations, n and p, or the quasi-Fermi levels, F_n and F_p, the gain can be calculated directly using the band structure [87].

1.6.3 Absorption, spontaneous, and stimulation emission

There are three major processes that take place to generate a laser – absorption, spontaneous, and stimulation emission. Absorption is the first process when light or current is applied to a gain medium. In both optical and electrical injection, energy is absorbed by the carriers. Then, these carriers are excited to higher levels. The absorption inside the material can be measured by determining absorption coefficient. Optical absorption coefficient, α (1/cm), is

$$\alpha = \frac{number\ of\ photons\ absorbed\ per\ second\ per\ unit\ volume}{number\ of\ photons\ absorbed\ per\ second\ per\ unit\ area},$$

$$\alpha(\hbar\omega) = \frac{R}{P/\hbar\omega} = \frac{\hbar\omega}{\left(\frac{n_r c \varepsilon_0 \omega^2 A_0^2}{2}\right)} R \qquad \text{(Equation 1.18)}$$

where R is the net upward transition rate per unit volume, P is the power density, $\hbar\omega$ is the energy of the photon, $\hbar$ is Planck constant, ω is angular frequency, n_r is the refractive index, and ε_0 is the permittivity of the vacuum.

Optical absorption spectrum is given by,

$$\alpha(\hbar\omega) = C_0 \left|\hat{e} \cdot P_{CV}\right|^2 \left[\frac{1}{2\pi^2}\left(\frac{2m_r^*}{\hbar^2}\right)^{\frac{3}{2}} \left(\hbar\omega - E_g\right)^{1/2}\right], \qquad \text{(Equation 1.19)}$$

where

$$C_0 = \frac{\pi e^2}{n_r c \varepsilon_o m_0^2 \omega}, \qquad \text{(Equation 1.20)}$$

m_r^* is the reduced effective mass ($1/m_r^* = 1/m_e^* + 1/m_h^*$), m_e^* and m_h^* are the effective masses of electrons and holes, respectively, m and e are the mass and charge of the electron, E_g is the energy of bandgap of material, $\left|\hat{e} \cdot P_{CV}\right|^2$, is the matrix element. For bulk material,

$$\left|\hat{e} \cdot P_{CV}\right|^2 = M_b^2 = \frac{m_o}{6} E_p, \qquad \text{(Equation 1.21)}$$

where E_p is the energy parameter that is taken from experiental data.

Rewriting Equations 1.20 and 1.21 in Equation 1.19, the optical absorption spectrum equation becomes

$$\alpha(\hbar\omega) = \left(\frac{\pi e^2}{n_r c \varepsilon_o m_o^2 \omega}\right)\left(\frac{m_o}{6} E_p\right)\left[\frac{1}{2\pi^2}\left(\frac{2m_r^*}{\hbar^2}\right)^{\frac{3}{2}}\left(\hbar\omega - E_g\right)^{1/2}\right]. \qquad \text{(Equation 1.22)}$$

The total upward transition rate is given by,

$$R_{12} = B_{12} S(E_{21}), \qquad \text{(Equation 1.23)}$$

where $S(E_{21})$ is the number of photons per unit volume,

$$S(E_{21}) = N(E_{21}) n_{ph} \; and \; n_{ph} = \frac{1}{e^{E_{21}/k_B T} - 1}, \qquad \text{(Equation 1.24)}$$

n_{ph} is the number of photons per state, and $E_{21}$is an optical energy between level 2 and 1 and equals to E_2 –E_1.

Spontaneous emission rate per unit volume (R_{21}^{spon}) can be calculated using the following equation:

$$R_{21}^{spon} = r_{21}^{spon}(E)dE = A_{21} f_2 (1 - f_1) \qquad \text{(Equation 1.25)}$$

And, the spontaneous emission rate per unit volume (R_{21}^{stim}) is given by:

$$R_{21}^{stim} = r_{21}^{stim}(E)dE = B_{21} f_2 (1 - f_1) S(E_{21}), \qquad \text{(Equation 1.26)}$$

where f_1 and f_2 are the Fermi-Dirac distribution of level 1 and 2, respectively. B_{21}, B_{21}, and A_{21} are Einstein's coefficients between two levels. From Equations 1.25 and 1.26, the spontaneous emission rate does not depend on the photon density, $S(E_{21})$.

1.6.4 Gain, loss, and threshold conditions

The gain in the laser is one of the important functions in the lasing processes. There are

two types of gain – material gain and optical gain. First, material gain is opposite to absorption with a negative sign. Material gain is the ability of material to absorb energy and provide carriers. Second, optical gain is the net gain when the gain becomes higher than the loss inside the laser cavity. Therefore, there are three areas for gain and loss mechanism domination: below, at, and above the threshold. The loss is higher than the gain inside the cavity below the lasing threshold. The emitted light in this stage is spontaneous emission. At threshold, the loss equals to the gain, and there is no lasing. The gain becomes higher than the loss in the laser cavity above the lasing threshold. The emitted light is a stimulated emission, and there are optical gain and net of gain increases with increasing gain [87].

The relation between gain and carrier concentrations is:

$$g(n) = g' (n - n_{tr}), \qquad \text{(Equation 1.27)}$$

where $g(n)$ is peak gain as function of carrier concentration, g' is the differential gain (dg/dn), n is the carrier concentration, and n_{tr} is the transparency concentration.

$$\frac{g(n)}{g'} = n - n_{tr} \qquad \text{(Equation 1.28)}$$

$$n = n_{tr} + \frac{g(n)}{g'} \qquad \text{(Equation 1.29)}$$

and at threshold condition,

$$G_{th} = \Gamma g_{th} = \alpha_i + \alpha_m, \qquad \text{(Equation 1.30)}$$

where G_{th} is the optical gain and Γ is the confinement factor defined as the part of the power that is guided by the waveguide. Its value is between 0 to 1, and the best conditions of waveguide is when Γ is close to 1. The confinement factor depends on the dimensions of the waveguide and refractive index inside and outside the waveguide. By knowing the Γ and thickness (d) of active medium, the effective thickness of optical mode can be calculated by (d/Γ); g_{th} is the gain at threshold condition, α_i is the internal loss, and α_m is the mirror loss.

$$g_{th} = \frac{\alpha_i + \alpha_m}{\Gamma} \quad \text{(Equation 1.31)}$$

By using Equations 1.29 and 1.31, carrier density at threshold becomes:

$$n_{th} = n_{tr} + \frac{\alpha_i + \alpha_m}{\Gamma g'} \quad \text{(Equation 1.32)}$$

$$\alpha_m = \frac{1}{2L} \ln\left(\frac{1}{R_1 R_2}\right) \quad \text{(Equation 1.33)}$$

where R_1 and R_2 are reflectivities of each facet of the cavity.

$$R_1 \cong R_2 = \frac{(n1 - n2)^2}{(n1 + n2)^2} \quad \text{(Equation 1.34)}$$

where n1 is the refractive index of the gain material and n2 the refractive index of outside the waveguide (air in most structures). The internal loss includes two parts as given by:

$$\alpha_i = \alpha_{(FCA)} + \alpha_s \quad \text{(Equation 1.35)}$$

where α_i is the internal loss that includes the free carrier absorption $\alpha_{(FCA)}$ and α_s is the scattering loss.

The free carrier absorption can be calculated using

$$\alpha_{(FCA)} = \frac{e^3 \lambda^2 n_c}{4\pi^2 c^3 \varepsilon_o n_r m_c^{*2} \mu_c} \quad \text{(Equation 1.36)}$$

where λ is lasing wavelength and μ_c is the carrier mobility. The carrier mobility is associated with the scattering time and effective mass of carriers [36, 87].

At threshold condition, Equation 1.10 becomes:

$$\eta_{in} \frac{J_{th}}{qd} = \left(An_{th} + Bn_{th}^2 + Cn_{th}^3\right) \quad \text{(Equation 1.37)}$$

$$J_{th} = \frac{qd}{\eta_{in}} \left(An_{th} + Bn_{th}^2 + Cn_{th}^3\right) \quad \text{(Equation 1.38)}$$

$$J_{th} = \frac{qd}{\eta_{in}} \frac{n_{th}}{\tau(n_{th})} \quad \text{(Equation 1.39)}$$

$$\frac{1}{\tau_{(n_{th})}} = \frac{1}{\tau_r} + \frac{1}{\tau_{nr}} = \frac{1}{\tau_r} + \left(\frac{1}{\tau_{SRH}} + \frac{1}{\tau_{Aug}}\right). \qquad \text{(Equation 1.40)}$$

Rewriting Equations 1.39 and 1.40, injected current density becomes:

$$J_{th} = \frac{qd}{\frac{\tau_{nr}}{\tau_r + \tau_{nr}}} n_{th} \left(\frac{1}{\tau_r} + \frac{1}{\tau_{nr}}\right) \qquad \text{(Equation 1.41)}$$

$$J_{th} = \frac{qd}{\tau_{nr}} n_{th} \left(\frac{1}{\tau_r} + \frac{1}{\tau_{nr}}\right)(\tau_r + \tau_{nr}) \qquad \text{(Equation 1.42)}$$

$$J_{th} = \frac{qd}{\tau_{nr}} n_{th} \frac{(\tau_r + \tau_{nr})}{\tau_r \tau_{nr}} (\tau_r + \tau_{nr}) \qquad \text{(Equation 1.43)}$$

$$J_{th} = qd \frac{(\tau_r + \tau_{nr})^2}{\tau_r {\tau_{nr}}^2} n_{th} \qquad \text{(Equation 1.44)}$$

Using equation 1.32 and 1.44,

$$J_{th} = qd \frac{(\tau_r + \tau_{nr})^2}{\tau_r {\tau_{nr}}^2} (n_{tr} + \frac{\alpha_i + \alpha_m}{\Gamma g'}) \qquad \text{(Equation 1.45)}$$

1.6.5 Light power output and efficiency

The output emission is mostly spontaneous and amplified spontaneous emission below the threshold. However, as the injected current increases above the threshold level, the emitted light becomes a stimulated emission. Equation 1.10 can be written as:

$$\eta_{in} \frac{J_{th}}{qd} = R(n_{th}) + v_g\, g(n_{th}) S \qquad \text{(Equation 1.46)}$$

$$\eta_{in} \frac{J}{qd} = \left(An_{th} + Bn_{th}^2 + Cn_{th}^3\right) + v_g\, g_{th} S \qquad \text{(Equation 1.47)}$$

$$S = \eta_{in} \frac{J - J_{th}}{qdv_g\, g_{th}} \qquad \text{(Equation 1.48)}$$

where S is photon density.

$$\frac{1}{\tau_p} = v_g(\alpha_i + \alpha_m) = v_g \Gamma g_{th} \quad (Equation\ 1.49)$$

where τ_p is photon lifetime.

The output intensity (P_{out}) is given by:

$$P_{out} = \eta_i \frac{\hbar\omega}{q} \frac{\alpha_m}{\alpha_i + \alpha_m} (I - I_{th}), \quad \text{(Equation 1.50)}$$

where the current I = (wLJ), L is the cavity length, and w the width of the device. The external efficiency (η_e) can be calculated by:

$$\eta_e = \frac{\frac{dP_{out}}{dI}}{\frac{\hbar\omega}{q}} = \eta_i \frac{\alpha_m}{\alpha_i + \alpha_m} = \eta_i \frac{\ln\left(\frac{1}{R}\right)}{\alpha_i L + \ln\left(\frac{1}{R}\right)}. \quad \text{(Equation 1.51)}$$

The external efficiency depends on the internal efficiency, internal loss, and external loss of cavity.

1.7 Research statement

The goal of this study is to investigate the optical characterization of GeSn material and demonstrate optical pumped edge-emitting GeSn lasers. Alloying tin into germanium at different Sn compositions establishes a new class of direct material from group IV semiconductors with great monolithic features and compatibility with CMOS processing Si-based lasers for integrated photonics. A systematic study for GeSn at different Sn composition and GeSn layer(s) thickness is necessary to develop high quality of GeSn material with a direct bandgap for laser devices. Due to the tunability of the GeSn bandgap, there are tremendous opportunities to achieve GeSn lasers covering a wide range of wavelength in the short- and mid-infrared for optoelectronic applications.

1.8 Outline of dissertation

The motivation and basic information about group IV material, directness and indirectness of the bandgap, and Si-based group IV lasers have been explained in the introductory chapter. The remainder of the dissertation is divided into six chapters. Chapter 2 includes growth information, material and optical characterization techniques and setups. Moreover, the design, fabrication, and device characterization with setups are included. Chapter 3 describes a systematic study of thin GeSn alloys up to 12% with a complete photoluminescence (PL) and Raman study. Furthermore, n-type doped GeSn films studies are included. Chapter 4 shows the material and optical study of thick GeSn films with high-quality material for high performance emitting devices. Chapter 5 describes the initial optically pumped GeSn laser. The growth of GeSn samples with material and optical studies are contained within. The edge-emitting GeSn laser devices fabrication and characterization are described. Chapter 6 presents a complete set of GeSn laser samples with different thicknesses and Sn compositions. The material and optical characterization of GeSn are described. The GeSn laser device fabrication, characterization, and performance are included. Chapter 7 gives the summary, conclusion, and suggested future work.

Chapter 2. Growth, fabrication, and experimental setup

In this chapter GeSn growth method, material and optical characterization techniques, device fabrication and characterization processes, and characterization setups are presented.

2.1 Growth and material characterization

2.1.1 Growth information

The thin and thick GeSn films in this study were grown using an ASM Epsilon® 2000 Plus reduced pressure chemical vapor deposition (RPCVD) system [ASM America, Phoenix, AZ, http://www.asm.com/]. Different growth parameters such as carrier and precursor gases, growth temperature, growth pressure and growth time have been implemented to achieve samples with various thickness, composition, and doping levels.

2.1.1.1 Thin and doped GeSn films

The thin $Ge_{1-x}Sn_x$ films investigated in this study were grown on a 700 nm strain-relaxed Ge buffer layer on Si substrate. The growth temperature was kept below 450 °C to be compatible with Si CMOS processing. GeH_4 and $SnCl_4$ were used as Ge and Sn precursor gases, respectively. For the n-type doped samples, PH_3 precursor gas was employed. Details of the growth information are reported in Ref. 90.

2.1.1.2 Thick GeSn films

Thick GeSn films were also grown in a similar process on a 700 nm strain-relaxed Ge buffer on Si substrate, followed by the growth of thick GeSn layer using a pre-calibrated growth recipe below 450 °C. The growth was completed with a 10 nm Ge cap layer as a cap on top of the

structure. It is noteworthy that the samples were grown in a single run epitaxy process. The thick GeSn samples were between 400 to 1100 nm. In order to achieve relaxed GeSn film and reach a higher Sn composition, two or more layers of GeSn were grown on some samples. The detailed information about the material growth is reported elsewhere [91-92].

2.1.2 Material characterization

2.1.2.1 Transmission electron microscopy (TEM)

A high-resolution field emission TEM with a 300 kV acceleration voltage was used for investigating the crystal structure, layer thickness, and the defect characteristics of $Ge_{1-x}Sn_x$ films. The correcting lenses allow imaging at a resolution ~0.1 nm by correcting the aberration. The TEM technique provides information about material quality, thickness, and the number of layers for each sample. The TEM images present four layers: Si substrate, Ge buffer, defective GeSn, and defect free GeSn layers as shown in Figure 2.1.

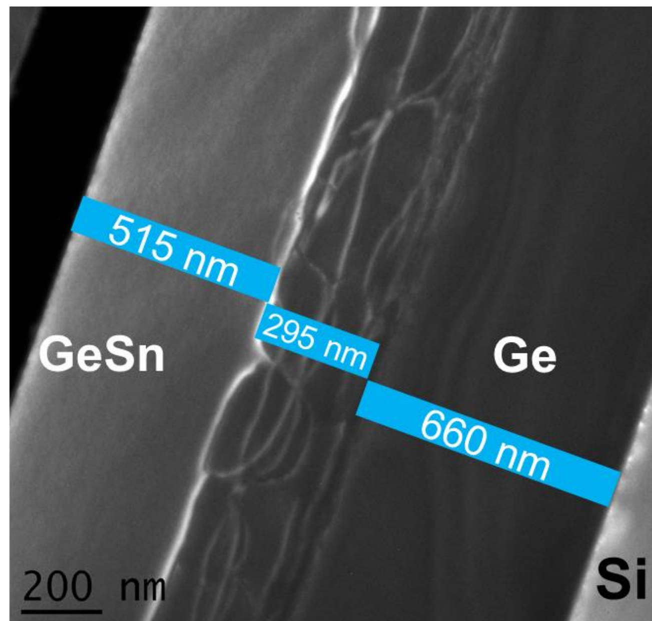

Figure 2.1. TEM image showing the different layers of GeSn/GeSn/Ge/Si structure of thick $Ge_{0.919}Sn_{0.081}$ sample [92]

2.1.2.2 X-ray Diffraction (XRD)

The crystallinity, lattice constant, Sn composition, and strain of the films were investigated by analysis of the data measured by a Phillips X'pert PRO XRD system [PANalytical, USA, http://www.panalytical.com/Xray-diffractometers.htm]. The 2θ-ω (rocking curve) XRD scan was used to show the peaks of different layers of a GeSn/Ge/Si sample. The peaks from (004) plane scan represent Si substrate, Ge buffer, and GeSn layers from 69° to 64.5°. The lower angle refers to higher lattice constant according to Bragg's law. Reciprocal-space mapping (RSM) XRD was performed to calculate the lattice constant, strain, and relaxation of GeSn films. Both 2θ-ω and RSM measurements are presented in Figure 2.2. Figure 2.2(a) shows the peaks belonging to Si substrate, Ge buffer, and GeSn layers. The RSM measurements from the $(\bar{2}\bar{2}4)$ plane provides information about in-plane ($a_{\parallel}$) and out-of-plane ($a_{\perp}$) lattice constants that can be used to calculate the lattice constant of GeSn layer as shown in Figure 2.2(b). Additionally, the contour plot illustrates the relaxation of the GeSn films as it can be seen in the figure there are two layers of GeSn formed on Ge buffer layer. The bottom layer has lower Sn composition than the top one. Both layers show a high degree of relaxation.

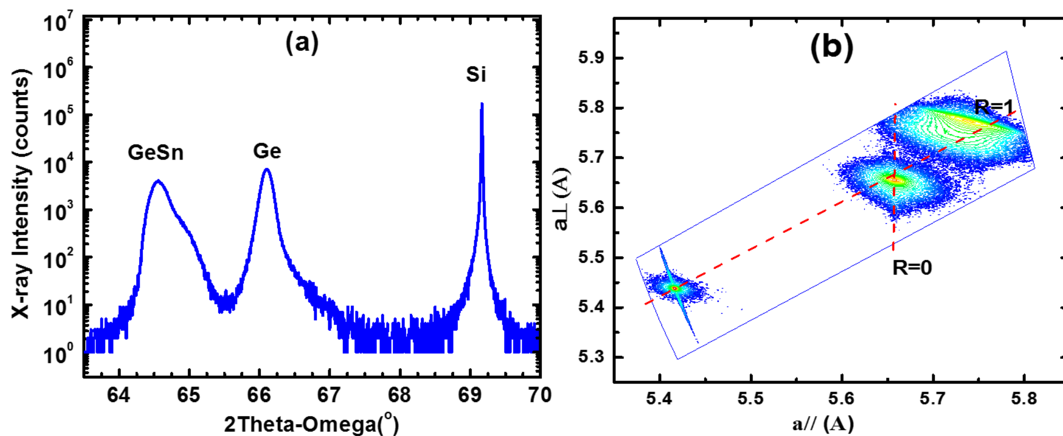

Figure 2.2. XRD measurements of relaxed thick $Ge_{0.882}Sn_{0.118}$ sample. (a) 2θ-ω XRD scan from (004) plane; the peak at 69° shows Si substrate, 66° is the Ge buffer, and 64.5° is the $Ge_{0.882}Sn_{0.118}$ peak. (b) RSM contour plot from $(\bar{2}\bar{2}4)$ plane represents the superposition of bottom and top GeSn layers, which are both almost relaxed.

2.1.2.3 Secondary ion mass spectrometry

Secondary ion mass spectrometry (SIMS) is one of the most powerful techniques that is used to analyze the composition of semiconductors and other solid materials. It is considered the most sensitive technique for depth profiling with lower detection limits in the range of 10^{14} to 10^{15} cm^{-3}. SIMS was used to determine the composition of Si, Ge, and Sn in GeSn films, and the thickness of each layer for multilayer GeSn samples. Figure 2.3 illustrates the composition and thickness of Ge and Sn in a $Ge_{0.825}Sn_{0.175}$ sample.

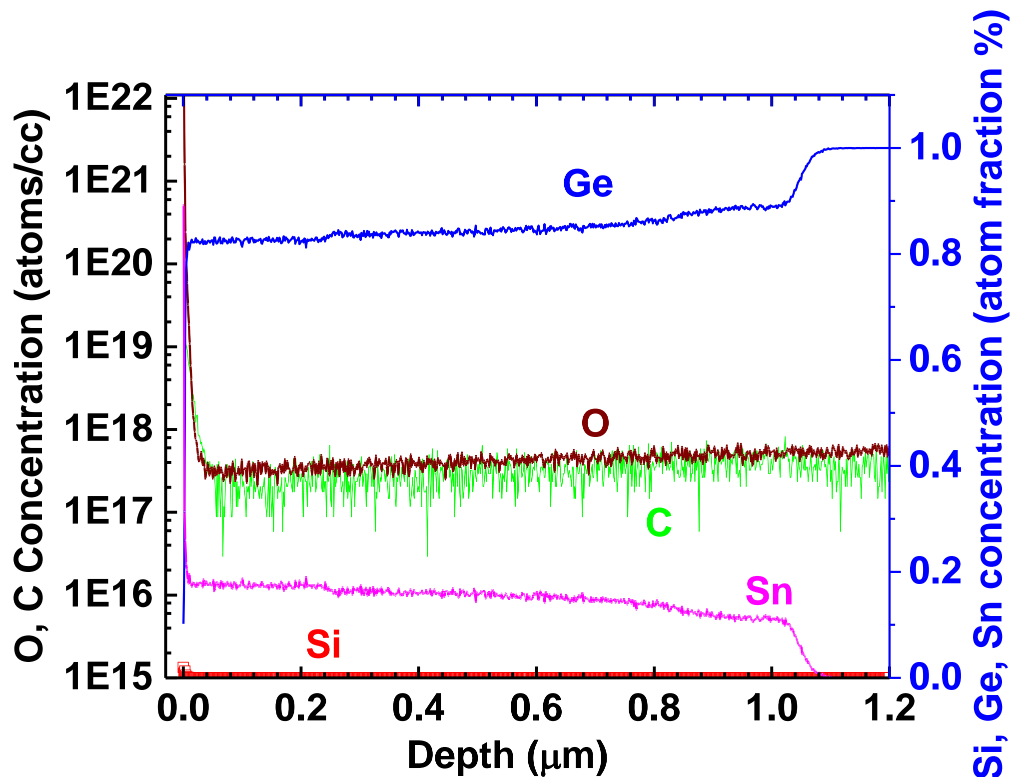

Figure 2.3. SIMS results show the mole fraction versus depth of Si, Ge, and Sn in a $Ge_{0.826}Sn_{0.174}$ sample. Also, SIMS shows the atomic concentrations of oxygen and carbon incorporated in the film through the growth process.

2.1.3 Optical characterization and setups

There are different types of techniques are used to characterize optical properties of materials, such as photoluminescence, ellipsometry, transmission spectroscopy, absorption

spectroscopy, Raman spectroscopy, and reflectance. These techniques are used to provide information about bandgap energy, intensity, incorporation of elements in the alloys, refractive index, absorption coefficient, etc. Many of these measurements were used for this study. However, the main focus was on PL and Raman spectroscopy.

2.1.3.1 Raman spectroscopy and Raman setup

Raman spectroscopy

Raman spectroscopy is a technique that is used to measure the crystallinity of solids. It is used to detect the strain in semiconductor materials or devices. The interaction between incident light and materials generates scattered light that contains both incident light and the scattered light with a small difference in the wavelengths that comes from the interaction between light and materials. Raman scattering is the interaction between the incident light and optical phonons. Raman scattered light is very weak; therefore, the monochromatic light resource is used for Raman spectroscopy measurements. Lasers with low power are mainly used as light sources for Raman measurements [93].

Raman setup

Raman spectroscopy was performed at room temperature using a He:Ne laser operating at 632.8 nm with the output power of 10 mW. Moreover, a diode-pumped solid-state (DPSS) continuous-wave (CW) laser operating at 532 nm with output power of 50 mW was used for Raman measurements. A nitrogen cooled Si-CCD array was used as a detector with wavelength coverage from 190 to 800 nm. The fluorescent background impacts Raman measurements; therefore, the setup was covered to eliminate the room light and enhance the intensity. Figure 2.4

illustrates Raman spectroscopy setup. Many optical components, such as mirrors and lenses, were used to control the path of lasers and optimize the collected scattered light from samples. Filters were used to avoid the detector damage.

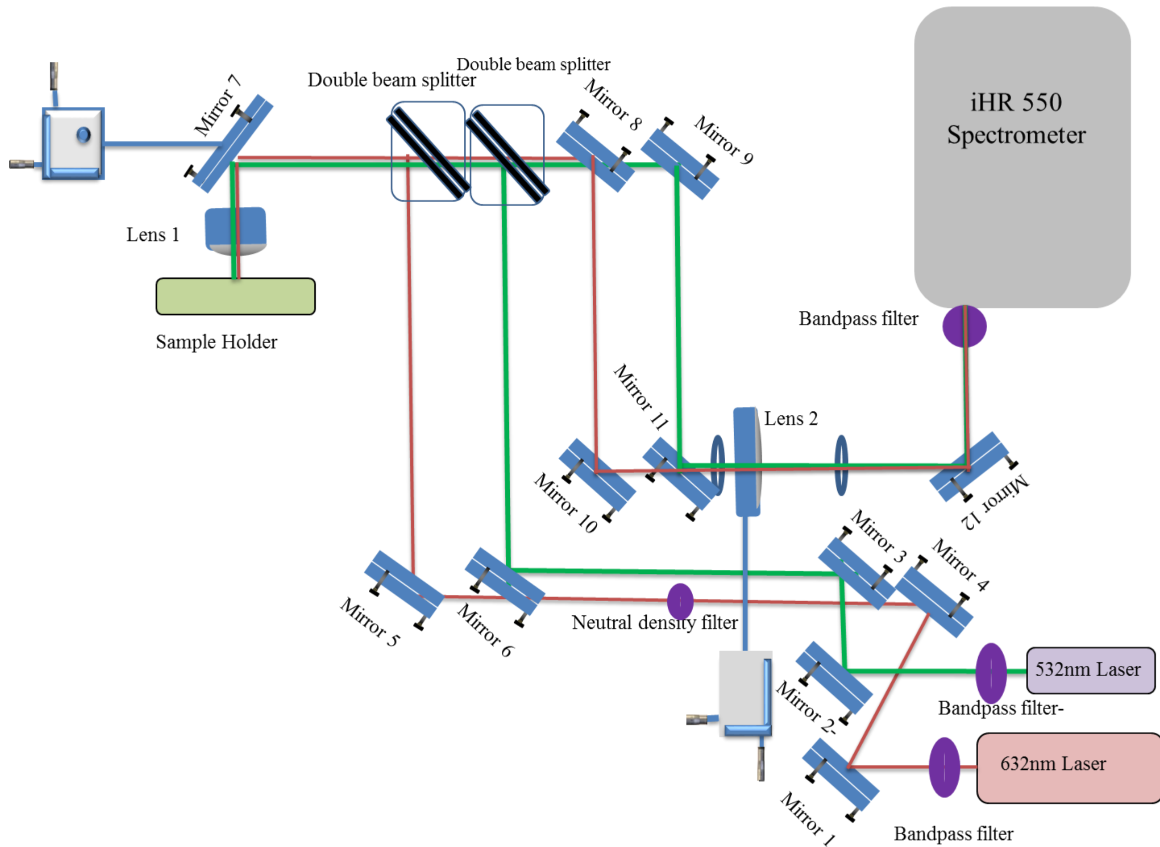

Figure 2.4. Schematic diagram of Raman spectroscopy setup.

Raman measurements were done for all GeSn alloys to show the effect of Sn compositions and strain on Raman peak shift of the GeSn films. By increasing Sn at%, the Ge-Ge Raman peak shifted to higher wavenumbers. Figure 2.5(a) and (b) show that the Raman peak was shifted from 4.96 cm^{-1} in a 7.3% Sn sample to 11.2 cm^{-1} for a Sn composition of 17.5%.

These samples were selected fully strain relaxed to show the Sn composition effect on Raman peak as Sn% was increased.

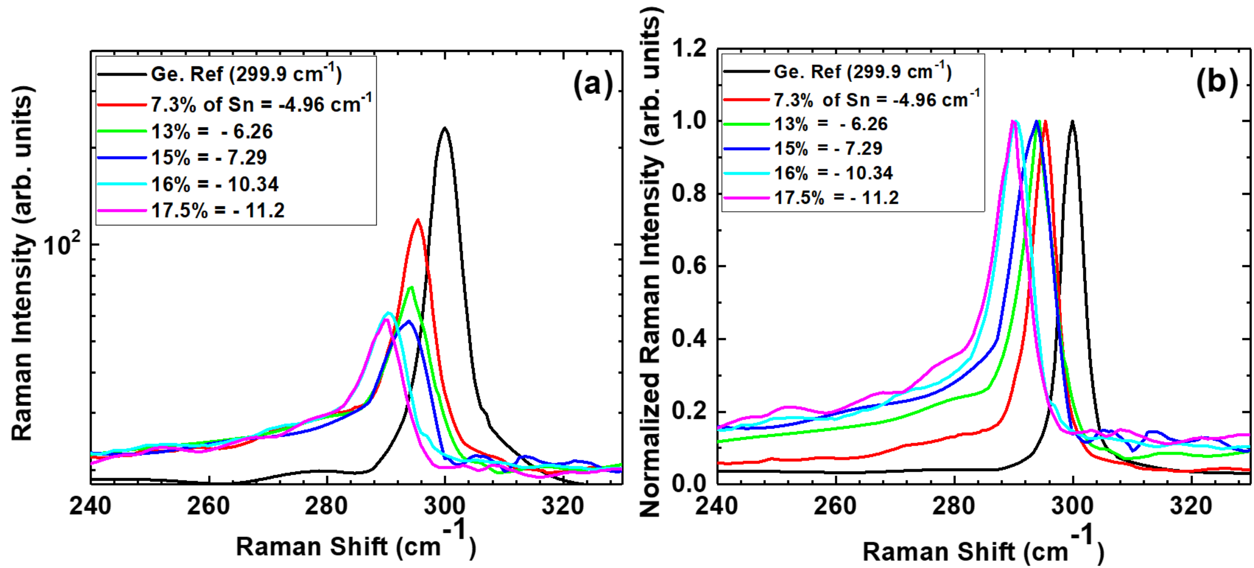

Figure 2.5. Raman shifts for thick relaxed GeSn samples from 7.3% to 17.5% at room temperature. (a) Decrease in the intensity of Raman peaks by increasing Sn incorporation. (b) Normalized Raman intensity showing the shift toward shorter wavenumbers by increasing Sn incorporation.

2.1.3.2 Photoluminescence characterization and PL setup

Photoluminescence (PL)

Photoluminescence (PL) is defined as a non-destructive technique. It is used to study and determine the impurities in semiconductors. Much information regarding different types of impurities can be provided using PL. However, the only photons that are generated by radiative recombination can be detected using the PL technique. Non-radiative recombination processes such as Shockley-Read-Hall and Auger do not emit light. Electron-hole pairs that are optically generated by radiative recombination process can be measured by the internal efficiency.

The internal PL efficiency (η_{int}) can be written as

$$\eta_{int} = \int_0^d \frac{\Delta n}{\tau_{rad}} \exp(-\beta x)\, dx \approx \int_0^d \frac{\Delta n}{\tau_{rad}} dx \qquad \text{(Equation 2.1)}$$

where Δn is the excess minority carrier density, d is the sample thickness, β is the absorption coefficient, and τ_{rad} is radiative recombination lifetime.

The excess minority carrier density depends on flux density of photons, reflectance, and mechanisms of recombination processes. Moreover, the absorption coefficient is different depending on the type of materials and wavelength of excited optical sources such as lasers. The penetration depth of excited source increases with increasing the wavelength [93].

The internal efficiency of indirect bandgap semiconductors is low due to the Shockley-Read-Hall and Auger recombination that takes place with a high percentage of the total recombination processes. Moreover, non-radiative recombination has more impact at room temperature. Therefore, low-temperature PL measurements are preferred to characterize emission light from semiconductors because, at low temperature, the radiative recombination dominates compared to non-radiative recombination.

PL setup

A diode-pumped solid-state (DPSS) continuous-wave (CW) laser operating at 532 nm with output power of 500 mW was used as an excitation source. In order to further investigate the optical transition characteristics, a high-frequency laser with 5 ns pulse width at 45 kHz repetition rate operating at 1064 nm was used as the pumping source, which featured deeper penetration depth and provided higher carrier injection compared to a 532 nm CW laser. A CW fiber laser with 1550 nm was used to study PL at higher penetration depth and for samples with many layers in the structure. Moreover, a femtosecond laser with tunable wavelength provided

more opportunities to explore the emission at several excitation wavelengths. Emissions from samples were collected by a spectrometer, and the collected light was then sent to the detector.

Three different detectors were employed to cover all ranges of emission: first, an extended indium gallium arsenide (InGaAs) photodetector (high signal-to-noise ratio) with cut-off 2.3 µm; second, a lead sulfide (PbS) detector (low signal-to-noise ratio) covered the range from 0.3 to 3 µm; third, an indium antimonide (InSb) detector (high signal-to-noise ratio) with a cut-off wavelength 5 µm. Both InGaAs and InSb detectors were cooled using liquid nitrogen (N_2). A lock-in technique was used to amplify the electric signal that was generated by detectors. In addition, a long-pass filter was placed in front of the spectrometer entrance to eliminate the scattered laser light. For temperature-dependent PL measurements, a closed cycle cryostat with helium gas was used. The schematic diagram of PL setup is shown in Figure 2.6.

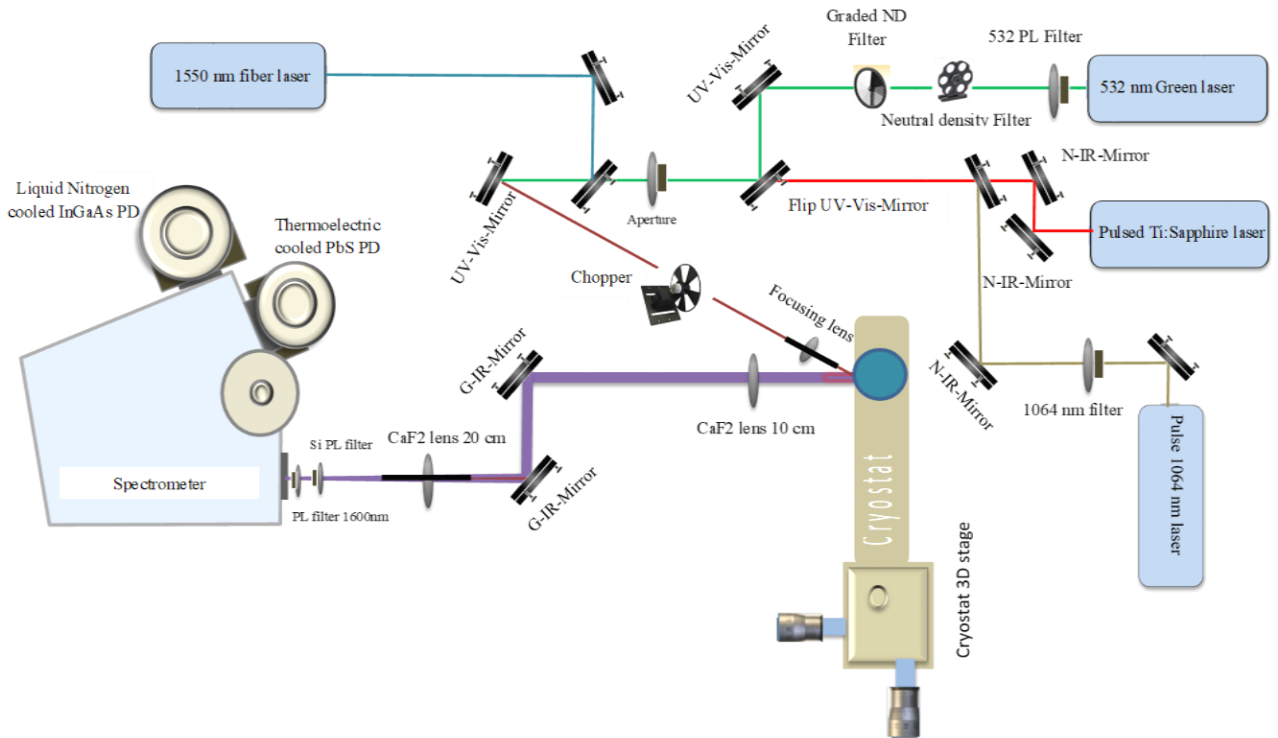

Figure 2.6. Schematic diagram of PL setup with several lasers sources.

PL measurements provide information about bandgap energy, directness and indirectness of transitions, and quality of materials. PL was intensively used to investigate GeSn alloys from 0 to 17.5% Sn compositions. The peak position of normalized PL intensity of GeSn films shifted to longer wavelength (red shift) with increasing the Sn composition as shown in Figure 2.7. The PL spectra range was from around 1.55 μm at 0% Sn composition to 3.4 μm for 17.5% Sn GeSn alloys at room temperature. At Sn composition less than 6%, there were two peaks corresponding to indirect and direct transitions of GeSn alloys. At 6% to less than 10%, there was only one peak, but it was broad because of the indirect and direct transition overlap. However, there was only one peak for samples with Sn higher than 10%. There were extra peaks shown at 2600 and 3000 nm due to the water absorption.

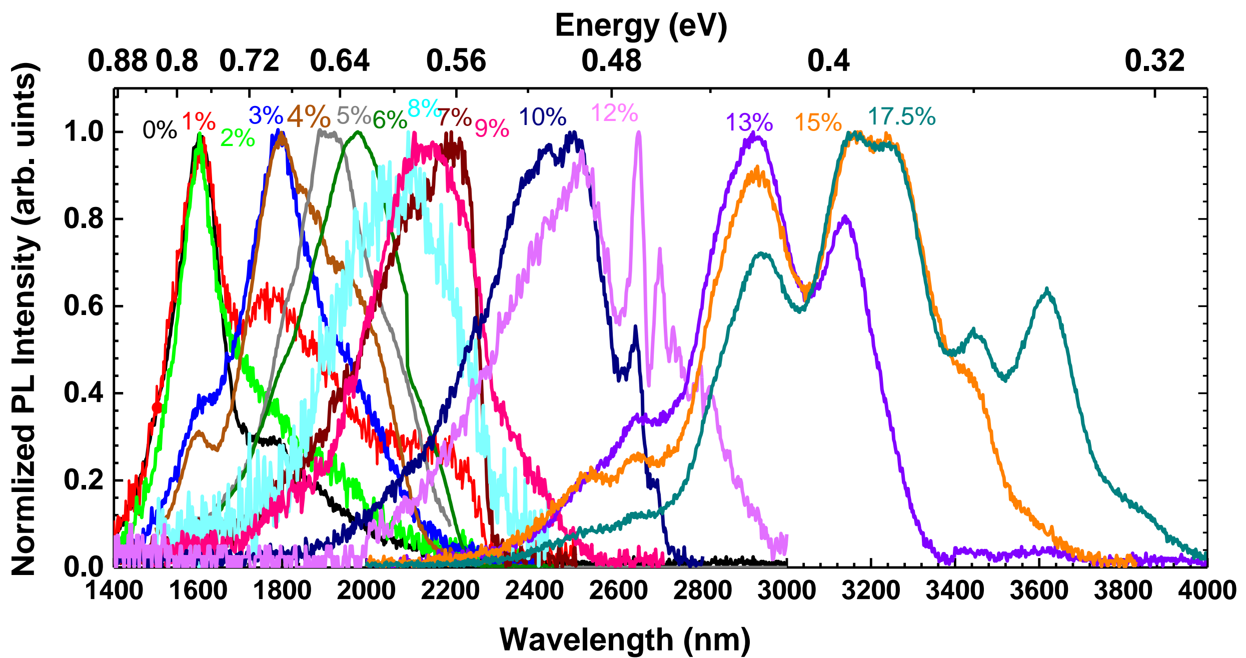

Figure 2.7. Normalized PL intensity of different Sn compositions from 0 to 17.5% of GeSn alloys at 300 K.

2.2. Fabrication processes of GeSn laser devices

2.2.1 Device design

Optically pumped lasers were designed into strip waveguides. Five waveguide widths were designed with a width of 1 to 5 µm. The separation between each two strips was 200 µm. This design provided a good opportunity to study different waveguide widths for each set of measurements. Figure 2.8 presents the fabricated waveguides using the designed mask.

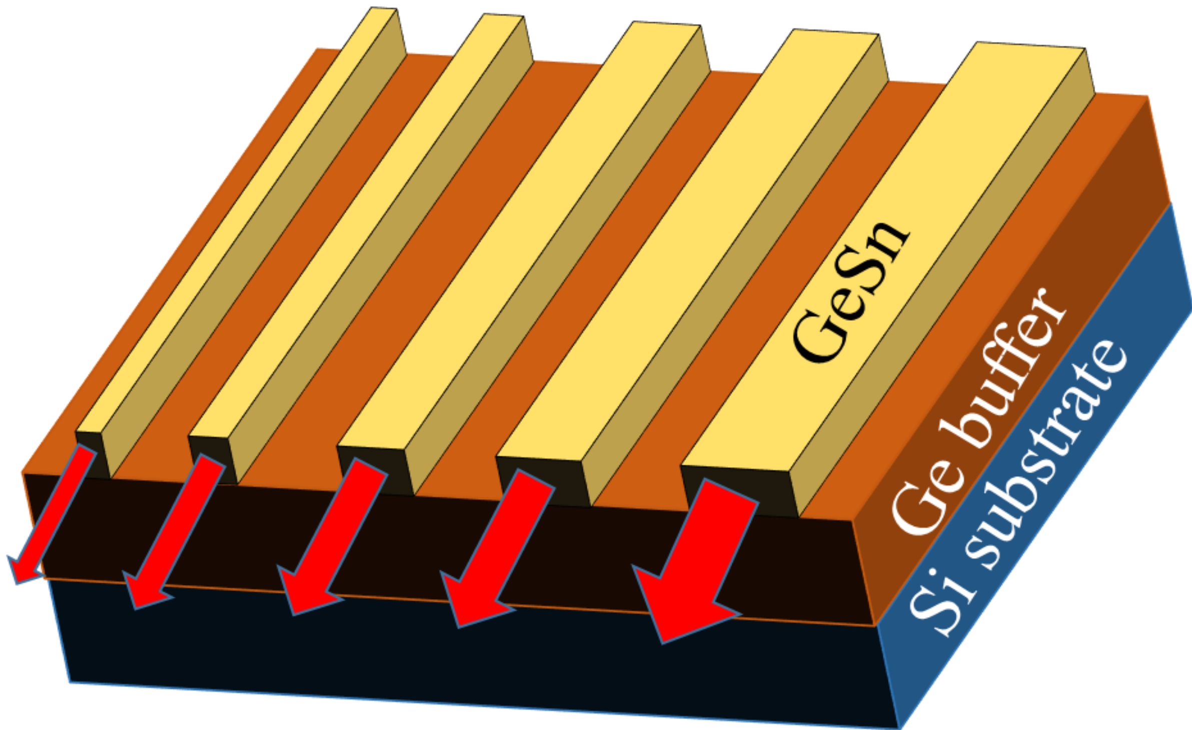

Figure 2.8 Schematic diagram showing the fabricated GeSn waveguides using the designed mask with several widths (1, 2, 3, 4, and 5 µm).

2.2.2 Wet etching

The samples were fabricated into a ridge waveguide with 1, 2, 3, 4, 5 µm widths for optical pumping characterization. A low-temperature wet chemical etching process was used for this research. Using a mixture of $HCl:H_2O_2:H_2O$=1:1:10 at 0 °C, smooth sidewalls were achieved. The average etching rate was ~20 nm/min. The etching depth was 800 nm. Due to the lateral etch, the waveguide widths at the top were measured to be between 2.5 to 3.5 µm, while the bottom was 5

μm for 5 μm width devices. Moreover, similar lateral etch behavior was observed for narrower devices (1, 2, 3, and 4 μm). An extensive etching study showed that the etching rate was almost constant at 20 nm/min regardless of the Sn composition. However, it did provide a smooth sidewall that could slightly reduce optical scattering loss for the waveguide structure. Therefore, the wet etching process developed in this study offered a robust recipe for the fabrication of GeSn-based devices. In Figure 2.9, scanning electron microscope (SEM) images show the $Ge_{0.882}Sn_{0.118}$ laser device for both sidewalls and facets. (More SEM images for GeSn laser devices are shown in Chapter 6.)

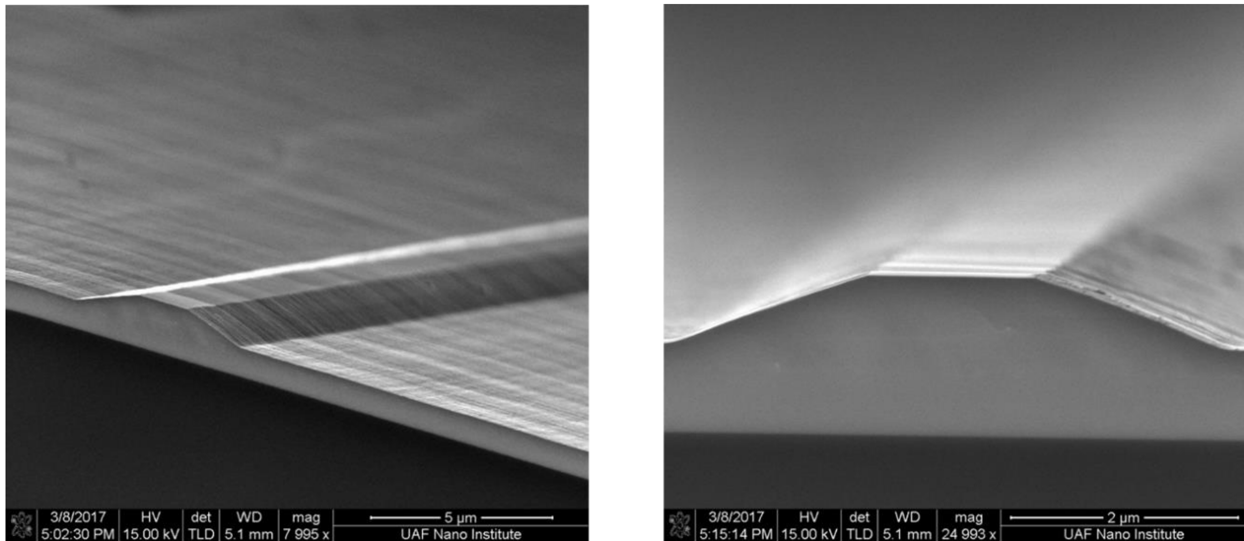

Figure 2.9. SEM images using wet etching method for the $Ge_{0.882}Sn_{0.118}$ laser device for both sidewalls and facets.

2.2.3 Dry etching

Inductively coupled plasma (ICP) etching was performed using an SLR ICP system [Plasma-Therm, USA, http://www.plasma-therm.com/about.html]. The pressure was set to 10 mTorr. The N_2 and BCl_3 flow rates were 25 sccm and 20 sccm, respectively. The bias power was 100 W and ICP power was 500 W. The etching rate was 175 nm/min. Figure 2.10 illustrates

the facets and sidewalls of a $Ge_{0.903}Sn_{0.097}$ laser device that was fabricated using dry etching. By comparison between wet and dry etching results in Figures 2.9 and 2.10, the dry etching provided parallel sidewalls which meant the width of the top waveguide was the same as the bottom. A waveguide width as low as 1 µm could be achieved using this dry etch method. In comparison, the wet etch waveguide would lose the pattern with widths below 3 µm (More SEM images for GeSn laser devices are shown in Chapter 6.)

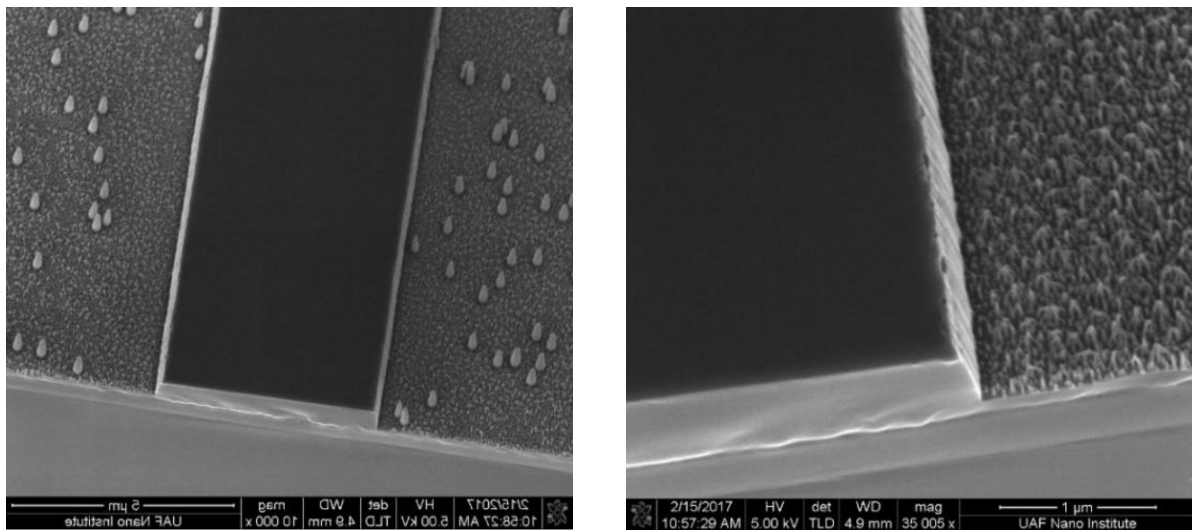

Figure 2.10. SEM images using dry etching method for the $Ge_{0.903}Sn_{0.097}$ laser device for both sidewalls and facets.

2.3 Lapping and cleaving processes

After the fabrication processes, the fabricated samples (1cm x 1cm) were lapped from the backside (Si substrate) to below 100 µm of thickness. The purpose of lapping was to cleave the laser devices to obtain better facets and could be easily done. From the cleaving practice, it was found that flat facets were difficult to obtain on small samples (1 cm x 1 cm) after cleaving. This was due to the uneven pressure applied onto the sample. This issue could be resolved by using samples with thinner thickness, typically below 100 µm for Si. After that, the devices were

cleaved to different cavity lengths which depended on the target of measurements. The GeSn laser devices characterized in this study were cleaved from 250 to 2000 μm as cavity lengths. Scribes and sharp knives were used for cleaving waveguides of GeSn.

2.4 Optical pumping setup and device characterization

Optically pumped GeSn laser devices were measured using the optical pumping setup shown in Figure 2.11(a) and (b). A set of GeSn laser devices were loaded inside the cryostat. The cryostat was connected to the pump station to create a vacuum environment that helped for low-temperature measurements. Both liquid helium (He) and liquid nitrogen (N_2) were used for low-temperature measurements. Several lasers shown in Figure 2.11(a) were used to test the devices. However, the optically pumped GeSn laser results were achieved using a pulse laser with 1064 nm wavelength and 45 kHz repetition rate. The pulse width of this laser was 6 ns. Both InGaAs and InSb photodetectors were used for the measurements of the devices. The type of detector used depended on the wavelength range of laser devices being tested. Several steps were taken to achieve better alignment and high intensity from the devices.

Edge-emitting GeSn laser devices were measured in this research. The optically pumped technique was used to test GeSn laser devices for several characteristics, such as L-L curves, spectrum, modes, and temperature operation. The GeSn laser devices were designed with different cavity lengths and widths to achieve lasing and investigate the threshold, optical gain, and to optimize device behavior. Two types of etching were used to fabricate the devices, wet and dry etching. Furthermore, several compositions, thicknesses, and number of layers of GeSn were explored to understand the behavior of GeSn lasers.

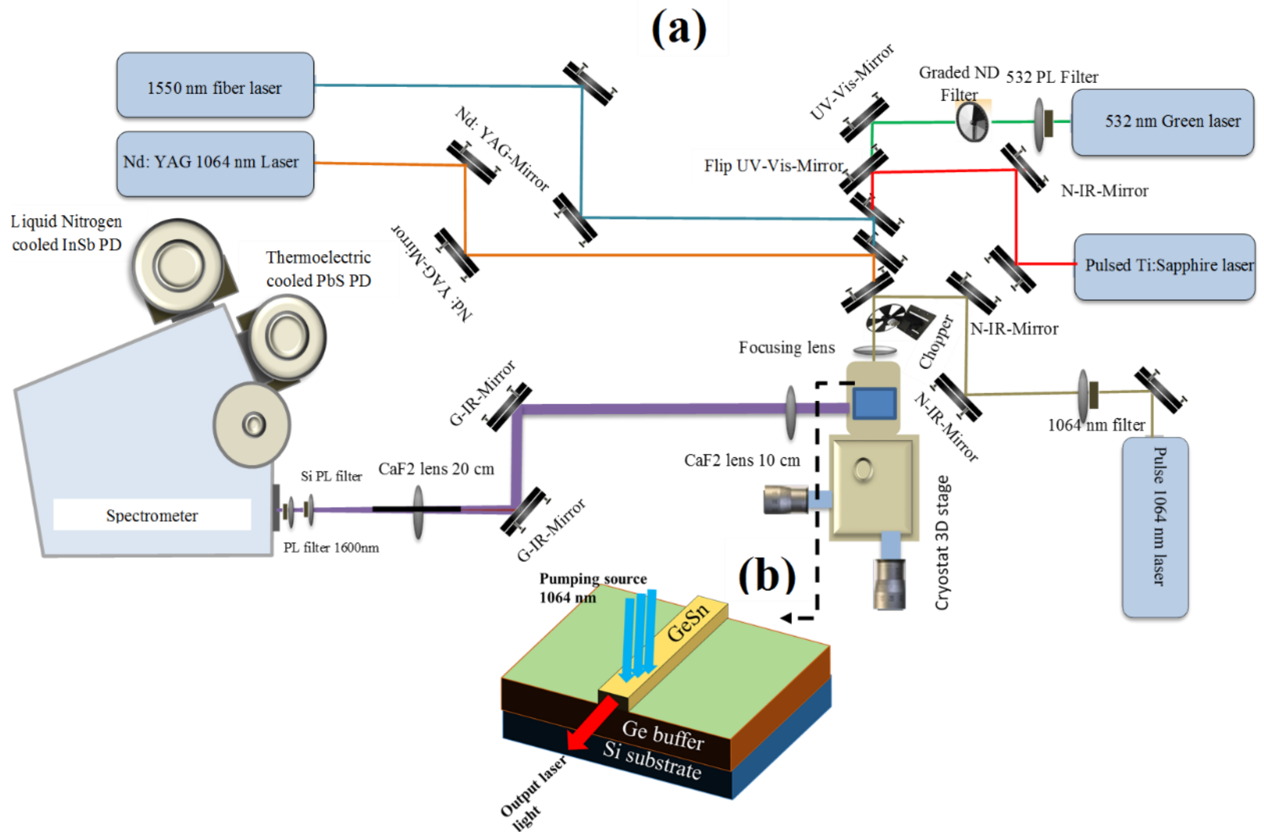

Figure 2.11. Schematic diagram illustrating (a) optical pumping setup for laser device measurements and (b) how a GeSn laser device was uploaded and measured inside the cryostat.

Chapter 3. Optical characterization of thin GeSn films

3.1 Introduction

Silicon-based materials and their optoelectronic devices are of great interest due to the scalable incorporation with current Si complementary metal-oxide-semiconductor (CMOS) processes [14]. Among the various material systems that could be integrated on Si, the $Ge_{1-x}Sn_x$ alloy has attracted much attention recently due to the following reasons; (1) capability of monolithic integration on Si; (2) availability of direct bandgap material [15]; and, (3) tunable bandgap covering broad shortwave- and mid-infrared (IR) wavelength range. The preliminary study in the analysis of optical properties of $Ge_{1-x}Sn_x$ alloy has been reported by several research groups [94-100]. However, the overall results are still less satisfactory due to the lack of systematic investigation on a set of $Ge_{1-x}Sn_x$ alloys with uniform material quality and various Sn compositions.

In this chapter, a systematic study of high-quality $Ge_{1-x}Sn_x$ thin films is presented. The thickness and strain of the thin film, the Sn composition, and the defect spreading were investigated by transmission electron microscopy (TEM), x-ray diffraction (XRD), and secondary ion mass spectrometry (SIMS). Optical characterization for unintentionally (boron) doped $Ge_{1-x}Sn_x$ alloys with Sn compositions from 0 to 12% was performed. Room temperature Raman and photoluminescence spectra showing a gradually shifted peak towards smaller wavenumber and longer wavelength, respectively, as Sn composition increased were obtained indicating the bandgap was altered by the Sn incorporation. Temperature-dependent PL spectra showing the variation of peak position and intensity were analyzed, which revealed the bandgap structure properties (indirectness or directness). Moreover, the n-type doped $Ge_{1-x}Sn_x$ alloy samples were studied to compare with the unintentionally doped samples (similar Sn

composition). The bandgap narrowing for n-type doped samples was observed. Understanding the fundamental optical properties of $Ge_{1-x}Sn_x$ alloy could provide a strong guidance for the design of future $Ge_{1-x}Sn_x$ based optoelectronic devices [16].

3.2 Material characterization

A typical cross-sectional TEM image of a $Ge_{0.9}Sn_{0.1}$ sample is shown in Figure 3.1. The Si substrate, Ge buffer, and GeSn layer are clearly identified. The film thicknesses of Ge buffer and GeSn layers were measured at 700 and 150 nm, respectively. It can be seen that the threading dislocations were localized at the Ge/GeSn interface, resulting in the low defect density in the GeSn film. The high quality of the material is attributed to the optimized growth recipe.

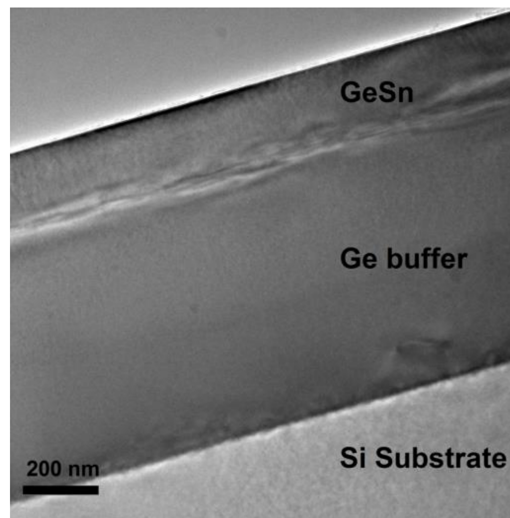

Figure. 3.1. Cross-sectional TEM image of Si/Ge/$Ge_{0.9}Sn_{0.1}$ film shows that the threading dislocations are trapped at the Ge/GeSn interface, resulting in a high-quality GeSn layer [16].

The 2θ-ω XRD scan of the GeSn samples from (004) plane is shown in Figure 3.2(a) and (b), for the unintentionally doped and n-type doped samples, respectively. The peaks at 69° and 66° are attributed to the Si substrate and the Ge buffer layer, respectively. The peaks that were observed between 66°-64° are from $Ge_{1-x}Sn_x$ thin films. The clearly resolved peak shifted toward

lower angles as the Sn composition increased. Since the position of the peak was determined by both the Sn composition and the strain, the peak of the 7% Sn sample was located at a higher angle than that of the 6% Sn sample due to the smaller compressive strain in the 7% sample [16].

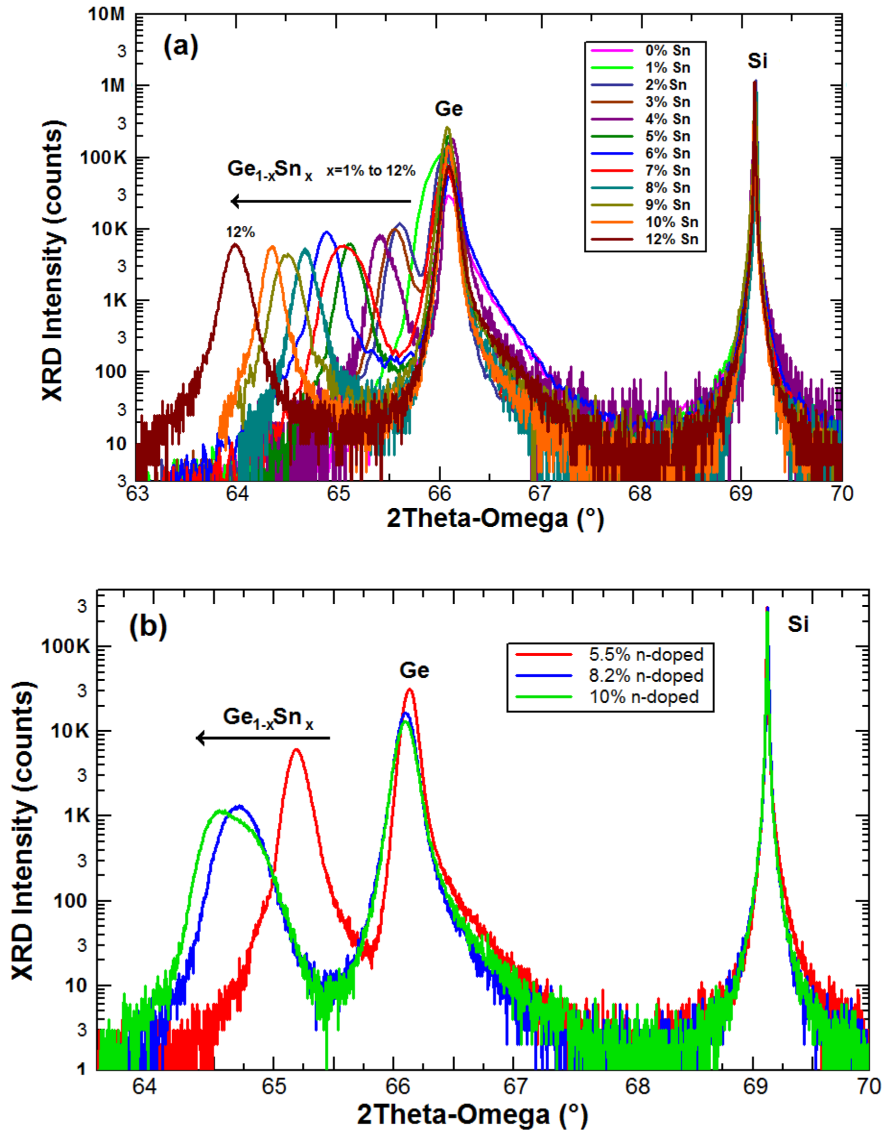

Figure 3.2. 2θ-ω XRD scan from (004) plane for (a) unintentionally doped and (b) n-type doped samples. The peak at 69º shows Si substrate and the peaks between 66-64º belong to $Ge_{1-x}Sn_x$ films [16].

The lattice constant of the GeSn films was calculated from the reciprocal space map (RSM, not shown here), based on the strain that could be determined, as listed in Table 3.1. The negative

value of strain indicated compressive strain, which was observed for each sample. As the Sn composition increased, the compressive strain increased due to the increased lattice constant of GeSn. On the other hand, the sample with thicker GeSn film exhibited lower strain because of the gradual relaxation as the layer thickness increased.

Table 3.1. Summary of measurement results of samples [16].

Sn Composition	GeSn Thickness (nm)	Strain	Doping	Doping Concentration (cm^{-3})
0 (Ge)	300 (Ge)	0	Unintentionally p-type doped (boron)	1E17
1%	327	-0.0002		
2%	40	-0.0022		
3%	128	-0.0024		
4%	70	-0.0050		
5%	83	-0.0052		
6%	96	-0.0082		
7%	100	-0.0045		
8%	90	-0.0080		
9%	117	-0.0101		
10%	59	-0.0116		
12%	150	-0.0093		
5%	225	-0.0054	n-type doped (phosphorus)	6.5E19
8%	276	-0.0059		1E19
10%	338	-0.0050		2.9E18

3.3 Raman spectroscopy

Raman spectroscopy measurements were taken for each sample. Figure 3.3(a) and (b) show the Raman spectra for unintentionally and n-type doped samples, respectively. In Figure

3.3(a), as Sn composition increased, the Ge-Ge peak shifted from 299.9 cm^{-1} (0% Sn) to 292.6 cm^{-1} (12% Sn). This can be explained by the change of the bond energy of the Ge atoms in the lattice due to the incorporation of Sn. The Ge-Sn peaks were identified ranging from 260.3 cm^{-1} (3%) to 254.3 cm^{-1} (12%). For samples with Sn compositions of 1 and 2%, the intensity of Ge-Sn peak was relatively weak and therefore could not be identified. In Figure 3.3(b), the shift of Ge-Ge peak was observed, and Ge-Sn peaks can be identified. Increasing the Sn composition shifted the peak toward smaller wavenumbers; while the compressive strain shifted the Raman peaks toward higher wavenumbers. Therefore, the relaxed GeSn sample with 12% Sn would have a smaller wavenumber peak than a compressively strained one. The similar Raman peak shift tendency was also reported in Refs. 101-102.

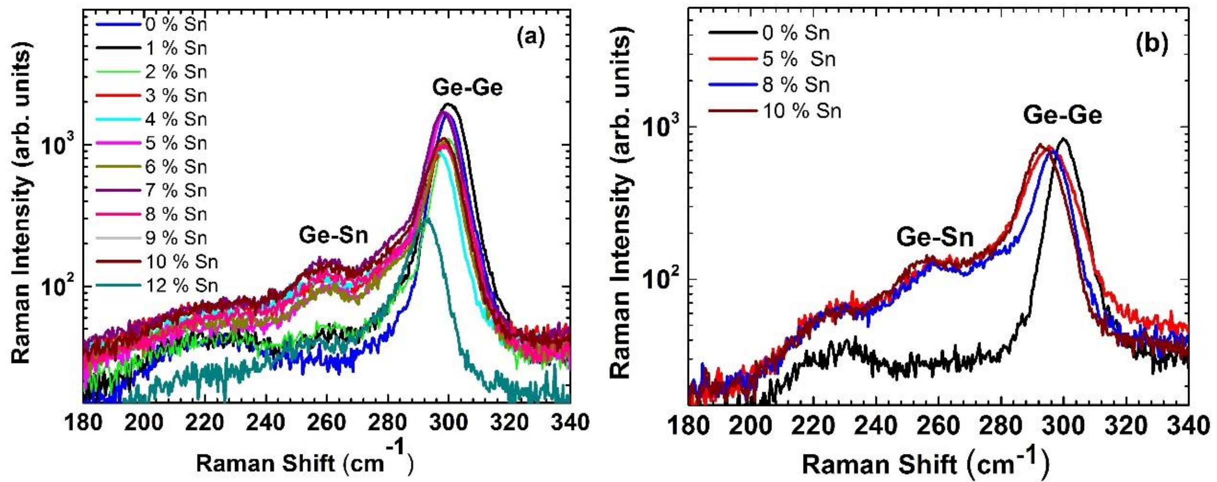

Figure 3.3. Raman spectroscopy for (a) unintentionally doped and (b) n-type doped samples. The Ge peak position is located at around 299.9 cm^{-1}, while the GeSn peak was identified ranging from 260.3 cm^{-1} to 254.3 cm^{-1} [16].

Also, the peak position showed a slight difference compared to the unintentionally doped sample with the similar Sn composition, which may be due to the heavy doping that alters the Ge atoms bond energy. The peak position of each sample is summarized in Table 3.2.

Table 3.2. Raman shift of Ge-Ge and Ge-Sn bonds for unintentionally and n-type doped samples [16].

Sn composition	Doping	Ge-Ge(cm^{-1})	Ge-Sn(cm^{-1})
0%	Unintentionally p-type doped (boron)	299.9	N.A.
1%		299.8	N.A.
2%		299.8	N.A.
3%		298.4	260.3
4%		295.9	257.9
5%		298.6	261.6
6%		298.1	261.8
7%		298.2	260.7
8%		297.9	262.0
9%		297.7	262.1
10%		297.9	259.2
12%		292.6	254.3
5%	n-type doped (phosphorus)	294.9	257.9
8%		295.9	258.7
10%		292.8	255.7

3.4 Photoluminescence of thin GeSn films

Normalized PL spectra of the unintentionally doped GeSn thin films with Sn compositions from 0 to 12% at room temperature are shown in Figure 3.4(a). As Sn composition increased, the PL peak shifted toward longer wavelengths, indicating the reduced bandgap energy due to the incorporation of Sn.

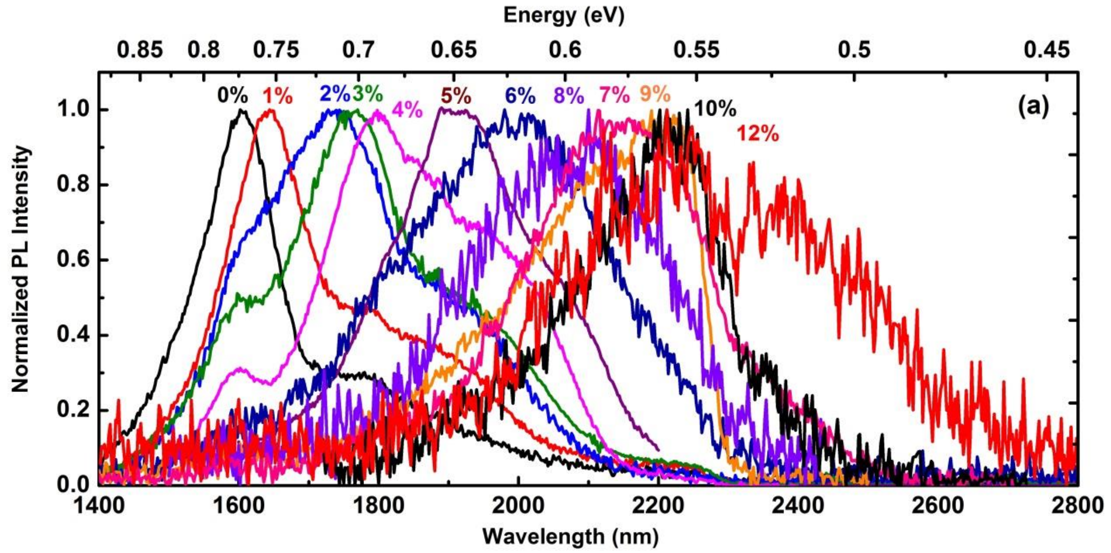

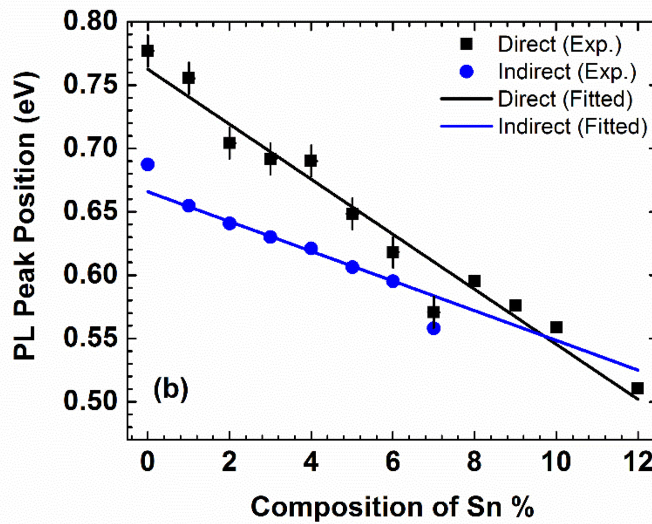

Figure 3.4. (a) Normalized PL spectra of the unintentionally doped GeSn thin films with Sn compositions from 0 to 12% at room temperature. (b) PL peak position attributed to the bandgap as a function of Sn composition [16].

For the samples with lower Sn compositions (less than 8%), two emission peaks were clearly observed, corresponding to the indirect and the direct bandgap transitions, respectively. While for the samples with higher Sn compositions, the indirect and direct peaks could not be identified due to the small separation between the indirect and direct bandgap energies, resulting

in a single peak PL spectrum with broad peak line-width. In addition, the indirect-to-direct transition occurs at the Sn composition of 10% [15], beyond that the GeSn alloy becomes the direct bandgap material, and therefore only direct peak with narrowed peak line-width can be observed. Note that the noisy PL spectra of GeSn samples with Sn compositions from 8 to 12% was due to the use of PbS detector, which features 3.0 μm cut-off but with low signal-to-noise ratio. The GeSn sample with 12% Sn composition had lower quality compared to other samples. Therefore, the room temperature PL spectrum looks noisier compared to the rest of the samples. Low signal to noise ratio caused a fluctuation in the room temperature PL of that sample. However, for extracting the PL peak position with Gaussian function, only one peak was considered based on theoretical study [16].

Using a Gaussian fitting method, the PL peak position was extracted for each sample, which indicates the bandgap energy of $Ge_{1-x}Sn_x$, as shown in Figure 3.4(b). The solid and open symbols were extracted by Gaussian fitting and the linear lines were fitted curves showing the indirect-to-direct transition. As Sn composition increased, both indirect and direct bandgap energies reduced with a more rapid decrease of direct bandgap than indirect bandgap, leading to the reduced bandgap energy separation from 89.5 meV (0% Sn) to 12.6 meV (7% Sn). Only one peak could be observed for the samples with Sn compositions from 8 to 12%, which was due to the large spectra overlap of indirect and direct bandgap transitions (8 and 9% Sn samples) or the directness of the GeSn material (10 and 12% Sn samples). The indirect-to-direct transition point was located at the Sn composition slightly below 10%, which agrees well with Ref. 15; however, for relaxed GeSn samples, the transition point could happen for Sn compositions around 6%. The deviation between the Gaussian fitting points and the fitted lines was mainly due to the strain of the samples.

Figure 3.5(a) and (b) show the typical temperature-dependent PL spectra for unintentionally doped GeSn samples with Sn compositions of 5 and 12%, respectively. Each curve is stacked for clarity. In Figure 3.5(a), at 300 K, a high energy peak at 0.648 eV and a low energy shoulder at 0.606 eV were observed, which are associated with the direct and indirect bandgap transitions, respectively. The strong direct peak indicates that the direct bandgap transition dominated the PL at room temperature. As the temperature decreased, both the direct and indirect peak decreased with the direct peak dropping more rapidly than the indirect peak, resulting in the indirect bandgap transition dominating the PL below 200 K. At 10 K, the direct peak almost disappeared and only the indirect peak was observed. This can be explained by the fact that less electrons occupy the Γ-valley as a result of reduced thermal excitation from the lower L-valley at lower temperature.

The PL peak position and integrated PL intensity against temperature are plotted in Figure 3.5(c). The bandgap energy increased as temperature decreased, which follows the Varshni relation [103]. The integrated PL intensity decrease at low temperature was observed. While GeSn with 5% Sn is an indirect bandgap material, this PL intensity drop was expected. Although at low temperatures the defects are less active and radiative recombination should be enhanced, the number of available phonons for the indirect bandgap recombination decreased leading to a reduction of the PL intensity. A peak at 2250 nm was observed and its position and intensity were unchanged with temperature. That peak may be related to a defect, such as dislocation in the Ge buffer layer [104, 105]. Further investigation is needed to understand the type of the defect and the source of the emission. In Figure 3.5(b), at 300 K, a single peak at 0.558 eV was observed, which is assigned to the direct bandgap transition. At 300 K, non-radiative recombination centers suppress the PL intensity. As the temperature decreased, the line-

width kept decreasing while the peak intensity increased. At 10 K, a single peak with narrow peak line-width was observed. The PL peak position and integrated PL intensity against temperature are plotted in Figure 3.5(d), which reveals the direct bandgap material of GeSn with 12% Sn [15]. Since the Γ-valley minimum is lower than that of L-valley in direct bandgap GeSn, most electrons tend to populate on Γ-valley. Therefore, the indirect transition was dramatically reduced, resulting in the single peak PL spectra [16].

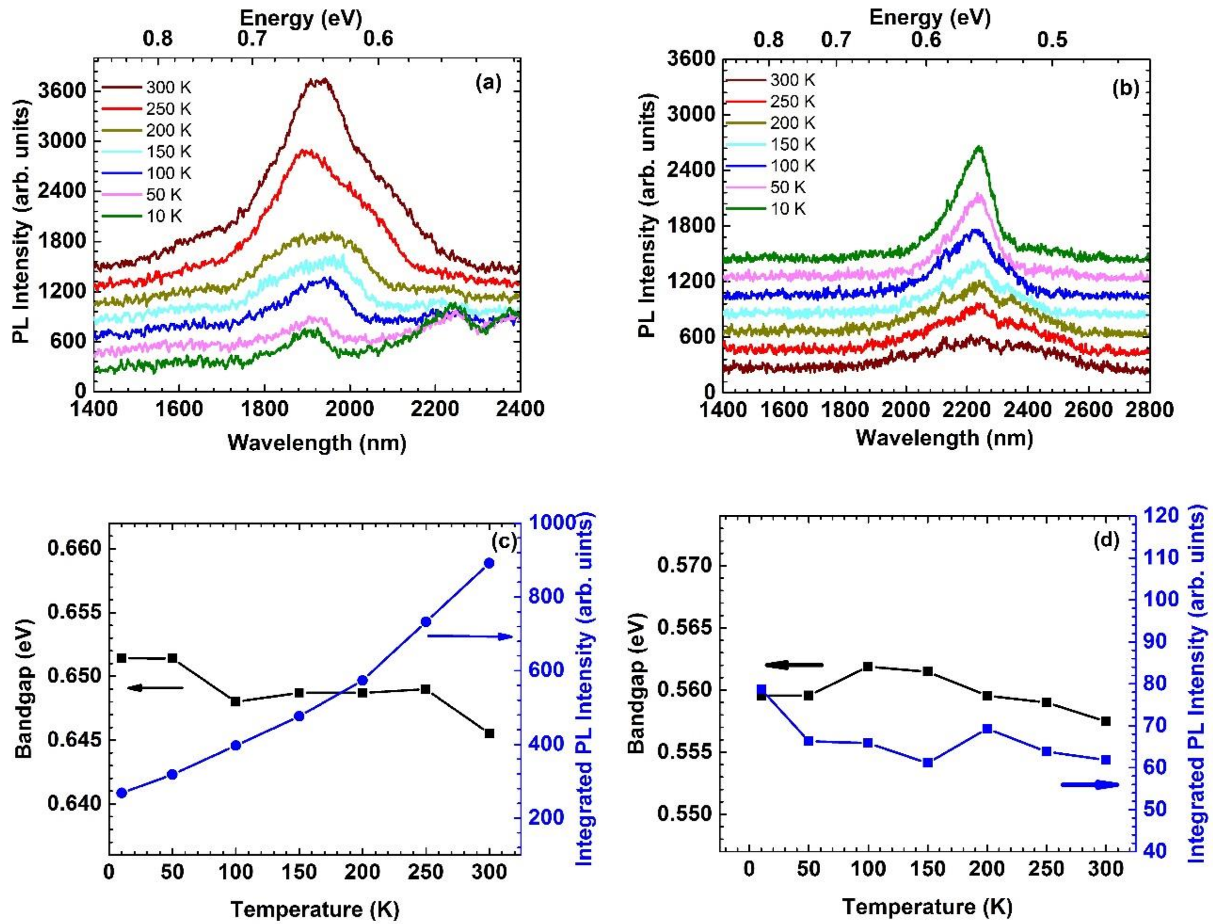

Figure 3.5. Temperature-dependent PL for GeSn samples with several Sn compositions. (a) 5% and (b) 12%. Extracted bandgap energy and integrated PL intensity as a function of temperature for samples with Sn compositions of (c) 5% and (d) 12% [16].

3.5 The impact of n-type doing on bandgap and intensity

The PL behavior of the n-type doped GeSn samples with Sn compositions of 5, 8, and 10% was investigated. Normalized room temperature PL spectra of n-type doped GeSn samples and their comparison with unintentionally doped samples with similar Sn composition are shown in Figure 3.6(a), (b) and (c), respectively. The direct bandgap shrinkage due to the n-type doping was observed as 42, 23 and 36 meV for 5, 8 and 10% Sn samples, respectively.

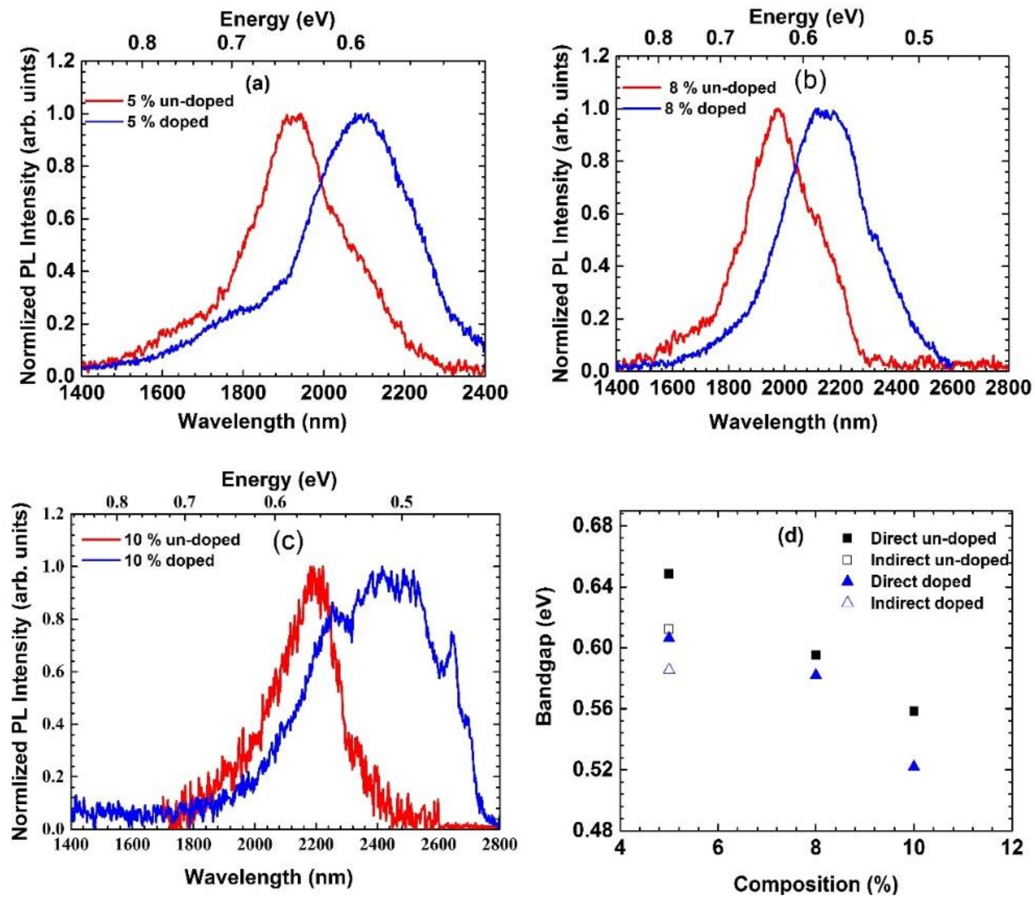

Figure 3.6. Comparison of the normalized PL spectra between the unintentionally doped and n-type doped GeSn samples with Sn compositions of (a) 5%, (b) 8%, and (c) 10% at room temperature. The indirect and direct bandgap shrinkages are summarized in (d) [16].

For 5% Sn sample, indirect bandgap shrinkage of 27 meV was obtained as well. The bandgap comparison is summarized in Figure 3.6(d). It is worthy to point out that since this was the first time that the doping induced bandgap shrinkage in the GeSn material has been observed,

more investigation is needed for further understanding of the mechanism. It can be seen that the Sn composition, material strain, and doping concentration all play a part for the bandgap altering [16].

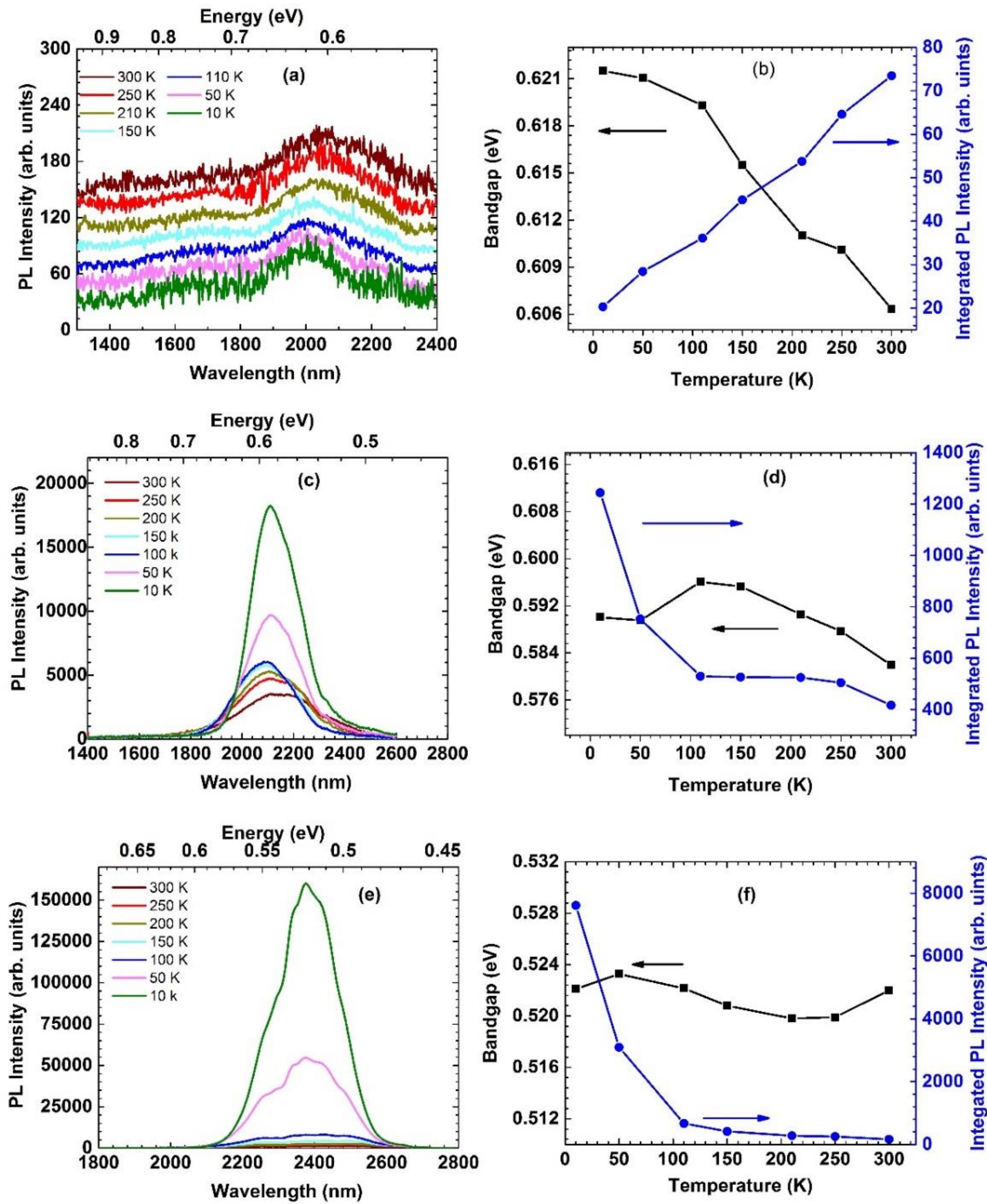

Figure 3.7. Temperature-dependent PL spectra for n-type doped GeSn samples with several Sn compositions. (a) 5%, (c) 8%, and (e) 10%. The corresponding bandgap shift and integrated PL intensity against temperature are plotted in (b), (d) and (f), respectively [16].

Furthermore, temperature-dependent PL spectra were obtained for n-type doped GeSn samples, as shown in Figure 3.7(a), (c) and (e) for Sn compositions of 5, 8, and 10%, respectively. Each curve is stacked for clarity. The temperature-dependent PL peak positions and integrated PL intensities were extracted by Gaussian fitting and are plotted in Figure 3.7(b), (d) and (f) for each sample, respectively. All samples exhibited bandgap increase as the temperature decreased which follows the Varshni relation. The fluctuation of data shown in Figure 3.7(d) and (f) are mainly due to the fitting error of Gaussian distribution.

For the 5% Sn sample, the integrated PL intensity decreased as temperature decreased, indicating the indirectness of the material. While for the 8 and 10% Sn samples, the integrated PL intensities increased at low temperature, showing the direct bandgap material behavior, which suggests the directness of the material. Specifically, the integrated PL intensity of the 10% Sn sample at 10 K is more than 40 times higher than that at room temperature. This fact may be favorable for the design of a GeSn laser [16].

3.6 Summary

Material and optical characteristics were studied for both unintentionally doped and n-type doped $Ge_{1-x}Sn_x$ samples with Sn compositions up to 12%. TEM and XRD show that the grown samples were consistent with the growth target in terms of the film thickness and Sn composition. The room temperature PL spectra exhibited gradual shifts of emission peaks toward longer wavelengths as Sn composition was increased. The temperature-dependent PL spectra revealed the indirectness and directness of the GeSn material. Moreover, the bandgap shrinkage was observed for the n-type doped GeSn sample for the first time.

Chapter 4. Thick GeSn Films with High Quality and Material Gain

4.1 Introduction

In order to improve the performance of the GeSn-based optoelectronic devices, which is mainly determined by the material quality, optimization of material growth method is the major decisive factor. Generally speaking, the deterioration of GeSn material quality takes place when: 1) the Sn composition becomes high (~10%); and/or, 2) the film thickness increases (larger than the critical thickness, which is determined by the Sn composition). However, the high Sn composition and the thick film are desired due to the following reasons: 1) the high composition of Sn results in more directness of the material, therefore, the direct bandgap transition is enhanced which provides a favorable radiative recombination for the emitters such as LEDs and lasers; 2) the high composition of Sn allows the operation wavelength of the devices to cover broader infrared range; 3) the thicker GeSn layer offers a favorable light absorbance, which is desirable for the photo-detection devices including photoconductors and photodiodes; and, 4) the thicker layer leads to the relaxation of the material. Compared to the compressively strained material, the GeSn devices fabricated with strain-relaxed films feature longer wavelength operation with the same Sn composition.

In this chapter, GeSn alloys grown on Ge-buffered Si substrate using a unique reduced pressure chemical vapor deposition (RPCVD) technique with $SnCl_4$ and GeH_4 as Sn and Ge precursors, respectively, are discussed. The material characterized by transmission electron microscopy (TEM) and x-ray diffraction (XRD) showed that the GeSn layers with the thickness ranging from 400 nm to 1 μm and Sn composition up to ~11% were obtained. The low defect density indicated the high material quality. Moreover, the temperature-dependent photoluminescence (PL) spectra showed that a longer emission wavelength was achieved due to

the strain relaxation compared to thin GeSn film (< 200 nm) samples with the same Sn composition. The PL intensity of the thick GeSn samples was enhanced compared to the previously studied thin GeSn films [16].

4.2 Material Characterization

Figure 4.1 shows a typical cross-sectional TEM image of sample C, $Ge_{0.9195}Sn_{0.0805}$. For the Ge buffer layer; it is clear that most of the defects were trapped at the Ge/Si interface and not propagated across the Ge layer, resulting in high material quality. For the GeSn layer, two distinct layers were clearly observed. The 150 nm-thick bottom layer over the Ge buffer layer was defective with a high density of threading dislocations.

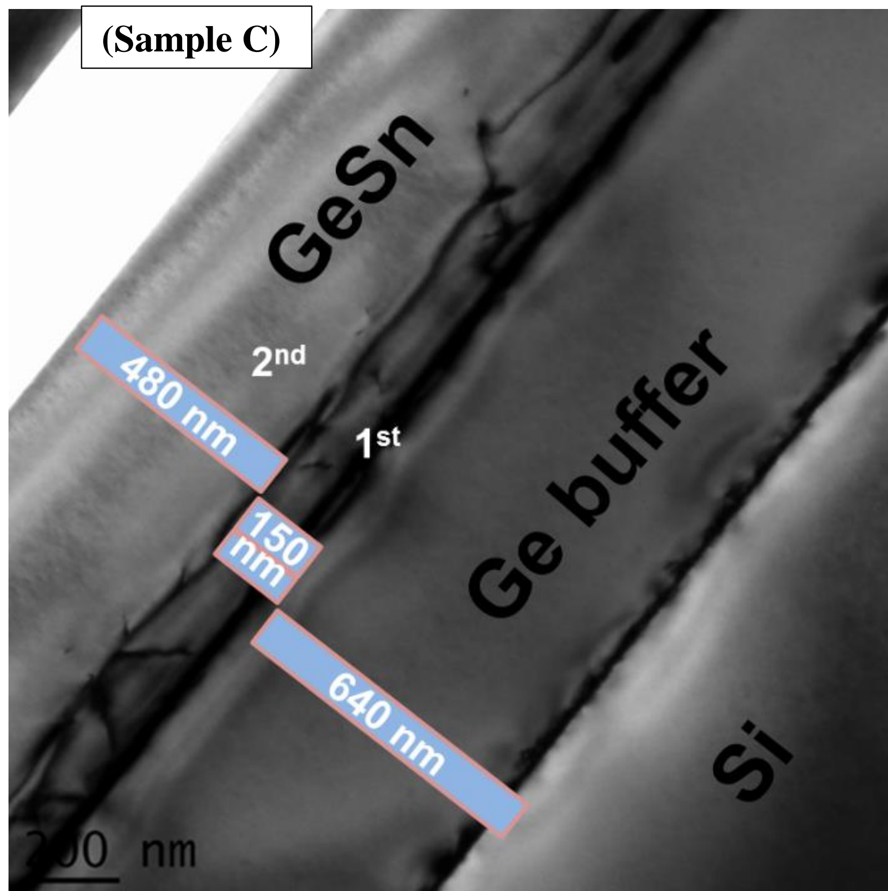

Figure 4.1. Cross-sectional view TEM image of sample C, $Ge_{0.9195}Sn_{0.0805}$.

This was mainly due to the lattice mismatch between the GeSn alloy and the Ge buffer. However, the formation of threading dislocation loops prevented propagation of the defects to the 480 nm-thick GeSn top layer, resulting in an almost defect-free GeSn layer with high quality. Note that the Sn compositions in GeSn bottom and top layers were measured as 6.89% and 8.05%, respectively. The Sn composition of the layers was calculated using Vegard's law, after finding the lattice constant of the top and bottom layers. The lattice constant of the bottom layer was found by fitting the peak in the shoulder of the 2θ-ω curve, as well as locating the peak position for the bottom layer in the RSM contour plot. The higher Sn composition in the top GeSn layer was attributed to the ease of Sn incorporation in a relaxed GeSn lattice. As shown in Table 4.1, the two-layer characteristic of GeSn alloy was not observed in sample A with 5% Sn, while it was formed in samples B, C, D, and E.

Table 4.1. Summary of GeSn sample, composition, thickness and relaxation [106].

Sample #	Sn composition (%)		Total GeSn thickness (nm)	Relaxation (%)
	GeSn bottom layer	GeSn top layer		
A	Single GeSn layer with 5.12% Sn		420	72
B	6.43	6.92	500	80
C	6.89	8.05	630	85
D	8.81	9.73	700	96
E	8.95	10.90	970	84

Formation of this layer is due to the presence of compressive strain before reaching the critical thickness. Higher Sn content films have larger lattice mismatch with the Ge buffer layer

and, therefore, induce higher compressive strain in the films. As a result, more Sn incorporation is observed after relaxation; while for low Sn composition films, since the critical thickness has not been reached, the formation of two-layers is not observable [107].

However, as a slight gradient in the Sn composition was observed, it was negligible to be considered as two layers in the 5% sample. Therefore, the intermediate layer did not form in the 5% Sn sample (A), was slightly formed in the 7% (B), and increased as the Sn incorporation increased up to 11% (E) [106].

A 2θ-ω XRD scan was performed on the GeSn samples from the (004) plane, as shown in Figure 4.2. The peaks were aligned at 69° which showed the reflection from the Si substrate. The peak at 66° referred to the Ge buffer layer. The Ge-cap layer peak was observed as a shoulder on the right side of the Ge buffer layer peak. The shifts in Ge-cap peak position to higher angle was due to the pseudomorphic growth of Ge on larger lattice size GeSn layer that caused a reduction in the out-of-plane lattice constant of the Ge cap layer. The GeSn peaks were observed at the angles from 64° to 66° depending on the Sn composition. As Sn composition increased, the GeSn peak shifted toward a lower angle. A shoulder was observed at the higher angle side of the GeSn peaks for samples B, C, D, and E, which reflects the formation of two GeSn layers. In order to calculate the film relaxation, the in-plane and out-of-plane lattice constants of each layer were obtained by performing a reciprocal space map (RSM) scan. The typical RSM contour plot of sample D is shown in Figure 4.2 inset. The Ge cap layer was observed as a separate plot from the Ge buffer since it experienced tensile strain. The broadened contour plot of GeSn indicated the existence of two layers, as annotated in Figure 4.2 inset. The GeSn layer was almost fully relaxed according to the calculation of lattice constant [106].

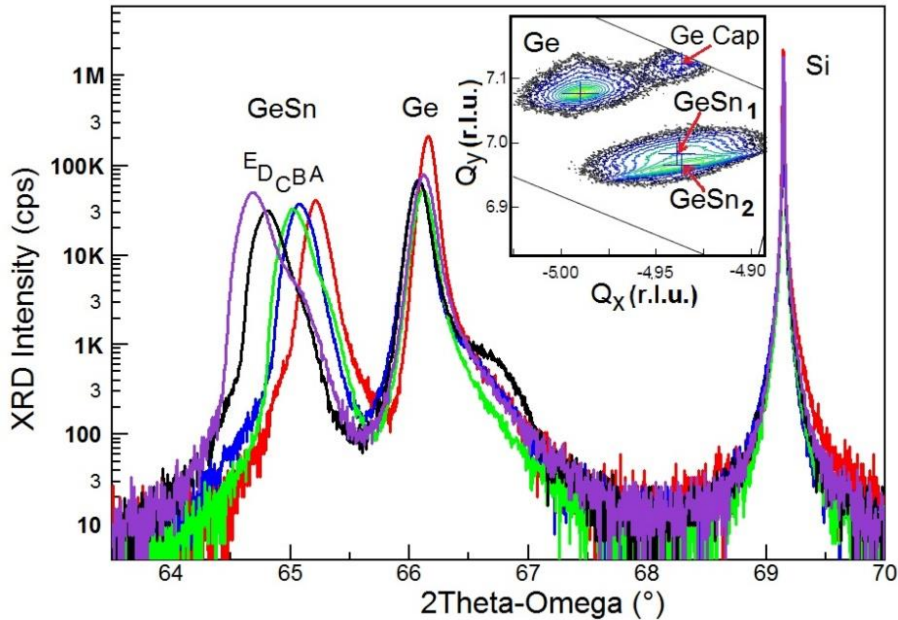

Figure 4.2. The 2θ-ω XRD scan from (004) plane for GeSn samples. The peak at 69º shows Si substrate and the peaks between 65.5-64º belong to GeSn films. (Inset) RSM plot of sample D samples showing the relaxation of GeSn layer [106].

4.2 Optical characterization of thick GeSn film

Figure 4.3 shows the normalized PL spectra of samples A-E at room temperature. The PL peak clearly shows the red shift toward longer wavelengths as the Sn composition increased, which is due to the reduced bandgap energy when more Sn is incorporated. The PL peak position shifted from 2120 nm to 2520 nm for samples A to E, respectively. Since the energy separation between direct and indirect bandgaps is small for each sample according to the theoretical calculation, the PL peaks associated with the direct and indirect bandgap transitions could not be distinguished from the PL spectra. Based on previous study on GeSn PL spectra [96], at room temperature the direct transition dominates the PL, i.e., the PL intensity of direct peak is much stronger than that of the indirect peak; therefore, the main peaks in Figure 4.3 are assigned to the direct bandgap transitions for all samples. Moreover, as the Sn composition increased, the integrated PL intensity (data not shown here) increased. This can be explained by the following: as the Sn composition

increases the direct bandgap edge reduces at a faster rate than the indirect bandgap edge, leading to more electrons populating the Γ valley in the conduction band (CB), which enhances the emission from the direct bandgap transition and, consequently, enhances the integrated PL intensity. On the other hand, for samples B, C, D, and E, since the Sn composition of GeSn bottom layer was lower than that of the GeSn top layer, the GeSn bottom layer could serve as a barrier layer to confine the carriers in the GeSn top layer. Therefore, the PL emission was mainly from the GeSn top layer. In Figure 4.3, a peak at 2660 nm was observed in PL spectra of samples D and E, which was due to the high order diffraction of the 532 nm laser source [106].

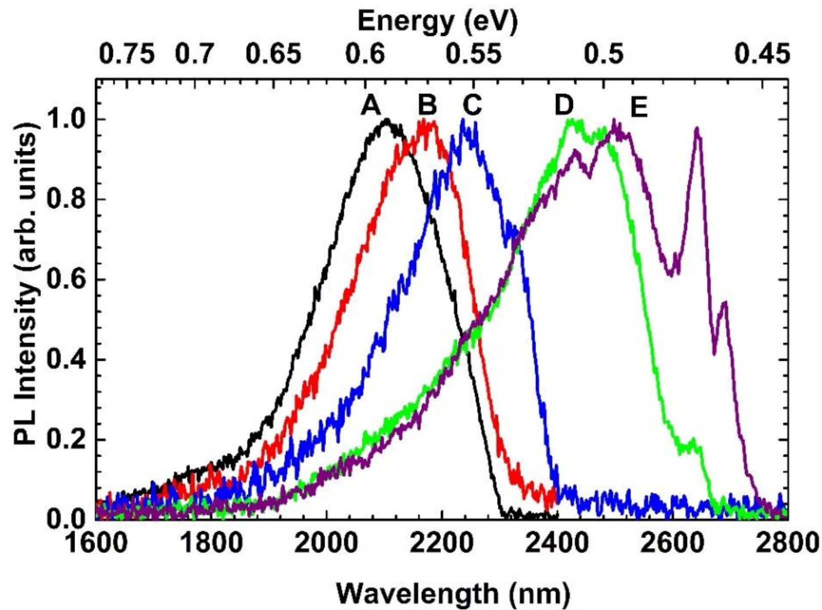

Figure 4.3. Normalized PL spectra of samples A-E at 300 K. As the Sn composition increased, the PL peak shifted toward longer wavelength due to the reduced bandgap energy. The main peaks are assigned to the direct bandgap transitions for all samples [106].

Figure 4.4a shows the comparison of PL spectra between sample C (8.05% Sn for the GeSn top layer) and GeSn thin film (90 nm thickness) with 8% Sn at 10 K and 300 K. The thin film GeSn sample was grown in the same chemical vapor deposition (CVD) reactor with the same precursors and gas flow rate [15]. Since two samples feature very close Sn composition, their

separations of PL peak positions are mainly determined by the strain of the layers. For 8% Sn thin film sample, which experienced the 0.8% compressive strain, PL peaks at 1950 nm and 1970 nm were observed at 10 K and 300 K, respectively. The PL intensity at 10 K is lower than that at 300 K, suggesting an indirect bandgap material. While for sample C, since the relaxed GeSn layer features the smaller bandgap energy compared to the compressively strained one, the PL peaks at a longer wavelength, i.e., 2100 nm and 2250 nm at 10 K and 300 K were observed, respectively. The PL intensity was considerably higher than 8% Sn thin sample, particularly at 10 K. This was because the narrower bandgap resulted in more injected electrons populating the Γ valley at 10 K and 300 K, leading to the increased PL emission intensity. Unlike the 8% Sn thin film sample, the PL intensity at 10 K of sample C was significantly higher than that at 300 K, and the peak linewidth was much narrower at 10 K which indicated that sample C was a direct bandgap material. Achieving direct bandgap GeSn with 8% Sn composition revealed that film relaxation pushed down the gamma valley in the CB lower than the L valley while it was not the case for the 8% strained GeSn thin film [106].

The comparison of PL spectra between thick film which sample D (9.73% Sn for the GeSn top layer) and GeSn thin film (thickness 59 nm and strain 1.16% in Ref. [16]) with 10% Sn at 10 K and 300 K is shown in Figure 4.4b. For the 10% Sn sample, PL peak positions of 2160 nm and 2200 nm were observed at 10 K and 300 K, respectively. This sample showed more directness of bandgap characteristic (higher PL intensity at a lower temperature) since higher Sn was incorporated. For sample D, PL peaks at 2240 nm and 2450 nm were obtained at 10 K and 300 K, respectively. Compared to the emission spectra measured in Ref. 21, which reported a PL peak position of 2250 nm at 20 K with 12.6% Sn sample, sample D in this study showed a similar wavelength of PL peak but with much lower Sn composition; this was attributed to the relaxation

of GeSn material. Moreover, the significantly increased PL intensity at 10 K indicated that sample D was a direct bandgap GeSn material [106].

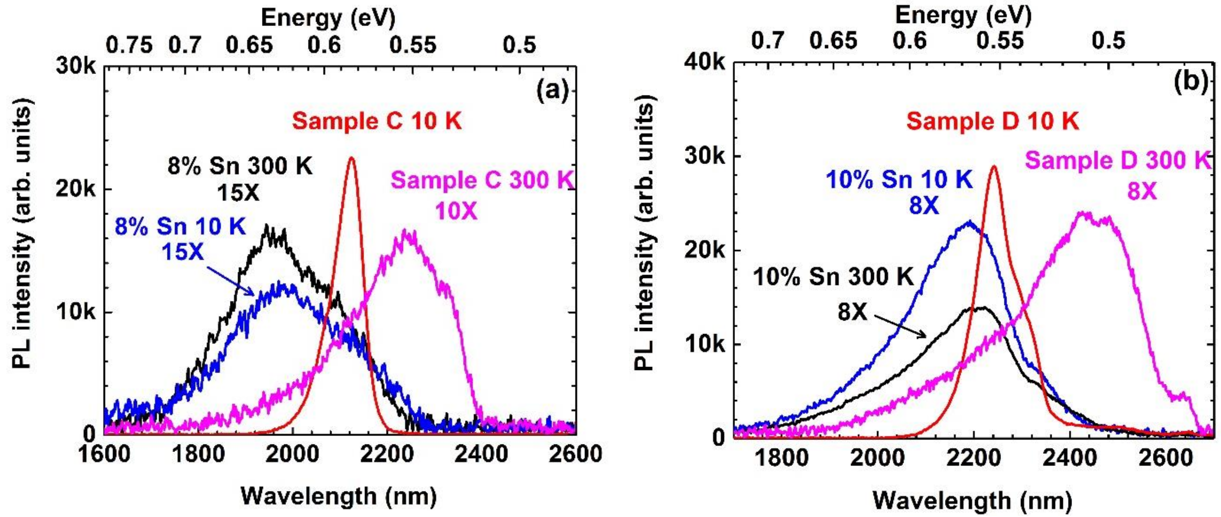

Figure 4.4. Comparison of the PL spectra between the GeSn thin and thick films at 10 K and 300 K. (a) Sample C and 8% Sn sample (90 nm thick); (b) Sample D and 10% Sn sample (59 nm thick) [106].

Temperature-dependent PL measurements were performed on each sample to study the PL characteristics further. The PL spectra at temperatures from 300 K to 10 K of sample A are shown in Figure 4.5a. The PL peak blue-shift at lower temperature was observed as expected nature of temperature-dependent bandgap variation. As the temperature decreased from 300 K, the PL intensity featured a decrease, followed by an increase at temperatures below 100 K. This PL behavior can be explained as follows: since sample A was an indirect bandgap GeSn with small separation energy (less than 1 kT) between the direct and indirect bandgaps at room temperature, the electrons which populated the L valley could be transferred to Γ valley via thermal activation, leading to the strong PL emission at 300 K. As temperature decreased, the number of thermally excited electrons reduced, and, therefore, the PL intensity decreased. Below 100 K, the non-radiative recombination velocity dramatically reduced, resulting in the band filling at L valley

which overcompensated the reduced thermally excited electrons and, consequently, the PL intensity increased [106].

Figure 4.5b shows the PL spectra at temperatures from 300 K to 10 K of sample E. It is clear that the PL intensity features a monotonic increase as the temperature decreases and the peak linewidth dramatically reduced at the lower temperature, confirming that sample E was direct bandgap GeSn. The smooth curve and strong PL emission shown in Figure 4.5b reflect the high material quality.

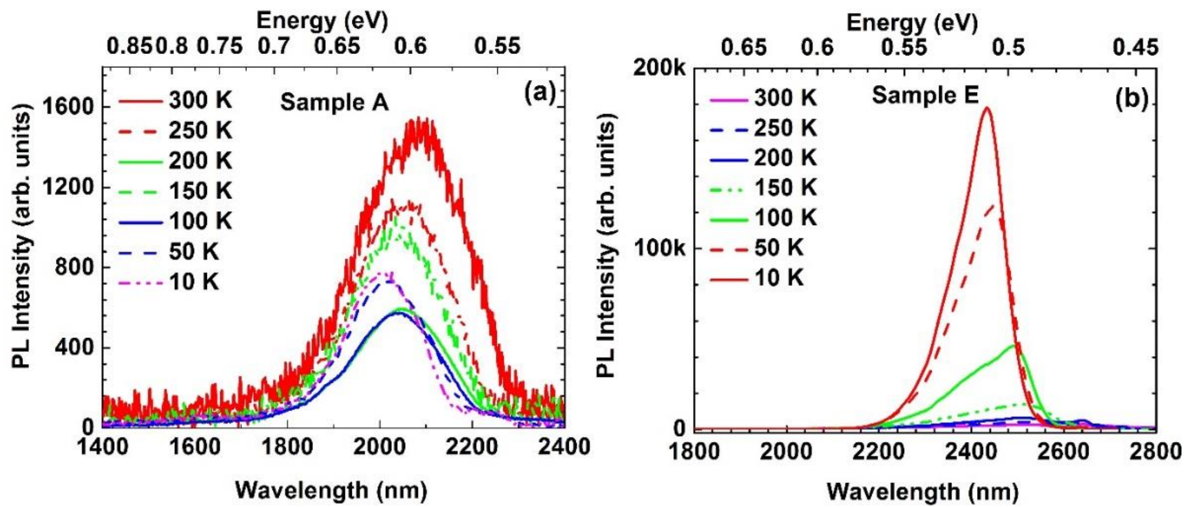

Figure 4.5. Temperature-dependent PL spectra from 300-10 K for (a) sample A and (b) sample E.

4.4 The impact of GeSn layer thickness on the material gain and intensity enhancement

Since based on estimation using the absorption coefficient measured via ellipsometry [108], the penetration depth of 532 nm laser is less than 100 nm, only a small portion of the incident light could reach the GeSn bottom layer. In order to further understand the optical transition characteristic of the samples studied, a 1064 nm high-frequency laser with a penetration depth of ~800 nm was used as the pumping source. Sample E was selected for further analysis as it featured

the highest Sn composition and material quality. Figure 4.6a shows the temperature-dependent PL spectra under the optical injection level of 270 kW/cm^2.

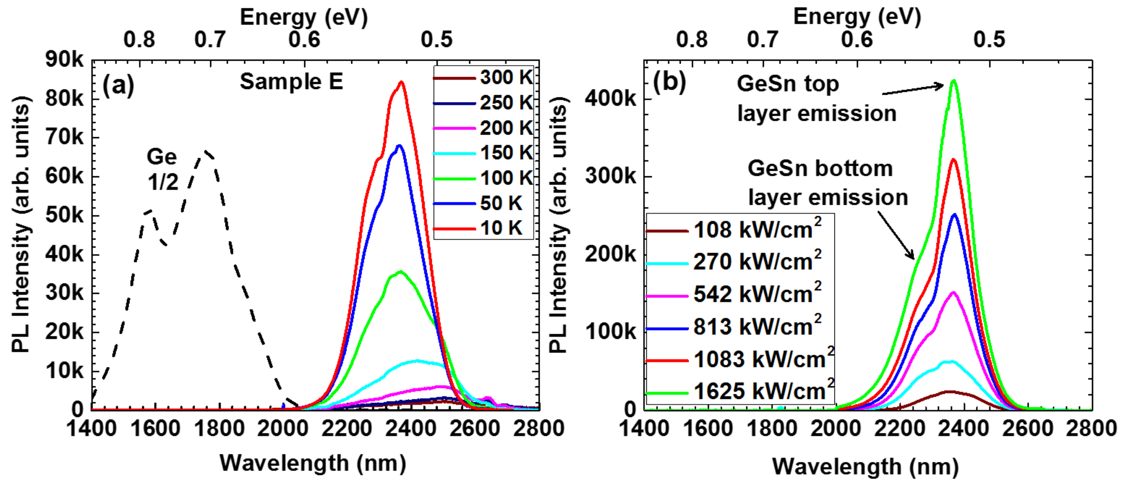

Figure 4.6. (a) Temperature-dependent PL spectra of sample E using 1064 nm high-frequency laser with 5 ns pulse width at 45 kHz repetition rate as the pumping source. The PL of Ge is also plotted for comparison. (b) Pumping power-dependent PL of sample E at 10 K. PL emissions from both GeSn top and bottom layers were observed at high optical injection level [106].

The PL of the Ge wafer reference sample is also plotted for comparison. The PL peak positions were obtained with the same 532 nm CW laser as the pumping source. Note that at the temperatures below 100 K, a shoulder at the higher energy side of the main peak was observed (2150 nm). This feature was assigned to the optical transition in GeSn bottom layer (8.95% Sn). Although the GeSn bottom layer was defective, at a low temperature most defects that act as recombination centers are frozen resulting in the enhanced radiative recombination and, therefore, the emission from GeSn bottom layer contributed to the PL spectra as well. Furthermore, the PL intensity of sample E at 10 K could compete with that of the bulk Ge sample, indicating the extremely high material quality [106].

Power-dependent PL measurement at 10 K was conducted to further confirm the transition from GeSn bottom layer, as shown in Figure 4.6b. At low injection level, only a single peak was

observed that was associated with the emission from the GeSn top layer. As the pumping power exceeded 270 kW/cm^2, a peak at 2250 nm could be observed and became stronger as the pumping power increased. Thus, this peak was assigned to the emission from GeSn bottom layer, at relatively low optical injection, almost all photo-generated carriers were confined in a GeSn top layer, which featured narrower bandgap. As injection level increased, more incident photons were absorbed in GeSn bottom layer, leading to radiative recombination occurring in the GeSn bottom layer before all the carriers transferred to GeSn top layer. However, the major contribution of PL was always from the optical transitions in the GeSn top layer, as can be seen in Figure 4.6b. Furthermore, the peak wavelength shown in Figure 4.6b featured red-shift compared to that shown in Figure 4.6a, which might have been due to the local heating under the high pumping power [106].

4.5 Summary

In conclusion, GeSn films with a thickness range of 400 nm to 1 μm were grown using an industry standard CVD system with commercially available precursors. The material study revealed the existence of two GeSn layers, i.e., bottom defective layer and almost defect-free top layer. Relaxation of strain in the first layer allowed higher Sn incorporation in the top layer. Temperature-dependent PL study showed that the emission wavelength shifted toward longer wavelengths compared to the thin film sample with the same Sn composition. Due to the relaxation of the material, direct bandgap GeSn was achieved with a lower Sn composition of ~8%. The dramatically enhanced PL intensity indicates extremely high material quality. Furthermore, the power-dependent PL study identified the optical transition from both GeSn top and bottom layers.

Chapter 5. Initial optically pumped GeSn edge-emitting lasers

5.1 Introduction

Studies on group-IV GeSn alloys open a venue for the development of gain medium monolithically integrated on Si for laser applications [109-110]. Theoretical calculations revealed that the incorporation of Sn into the Ge lattice reduces the energies between the Γ- and L-valley, and eventually could convert GeSn to a direct bandgap material [19, 111]. A direct bandgap GeSn alloy with Sn composition of 10% was experimentally demonstrated in 2014 [15]. Recent breakthrough on an optically pumped GeSn laser indicated major progress toward a fully integrated solution on the Si photonics platform [21]. The reported edge-emitting devices show lasing operation up to 90 K and have a threshold intensity of 325 kW/cm^2 at 20 K, all pumped with a 1064 nm nano-second pulsed laser. In 2016, the same team obtained the optically pumped GeSn microdisk laser [84] with improved performance such as a reduced threshold of 220 kW/cm^2 at 50 K.

This chapter presents the demonstration of optically pumped GeSn edge emitting lasers based on the Ge/GeSn/Ge double heterostructure (DHS) grown on Si. The significantly lower lasing threshold of 68 kW/cm^2 at 10 K (pumped with a 1060 nm nanosecond pulsed laser) is attributed to the intrinsically relaxed high-quality GeSn alloys grown in a unique chemical vapor deposition (CVD) process using GeH4 rather than other high order Ge-based hydrides as the precursor. The device showed lasing operation up to 110 K, and the laser characteristic temperature (T_0) was extracted to be 65 K [85, 112].

5.2 Material and optical characterization

5.2.1 Material characterization

After growth, the material quality, the layer thickness, the Sn composition, and the strain of the sample were carefully analyzed using TEM and high-resolution XRD techniques. Figure 5.1(a) shows a TEM image of the $Ge_{0.891}Sn_{0.109}$ sample. For the Ge buffer layer, the majority of defects were localized at the Ge/Si interface, indicating the high material quality. For the GeSn alloy, two distinct layers can be clearly observed. i) A 210 nm-thick bottom GeSn layer over the Ge buffer. This layer is defective due to the high density of threading dislocations, which arose mainly from the lattice mismatch between the Ge buffer and the GeSn alloy. The Sn composition in this layer was measured as 8.95%. ii) A 760 nm-thick high quality top GeSn layer above the bottom GeSn layer. Since the threading dislocation loop is formed in the bottom GeSn layer and does not propagate to the top GeSn layer, the top GeSn layer exhibits extremely high material quality. Threading dislocation densities (TDDs) of 3×10^6 cm^{-2} for the top GeSn layer and 2×10^7 cm^{-2} for Ge buffer layer (in a separate control sample with the same Ge thickness) were obtained based on the etch pit density measurement [85].

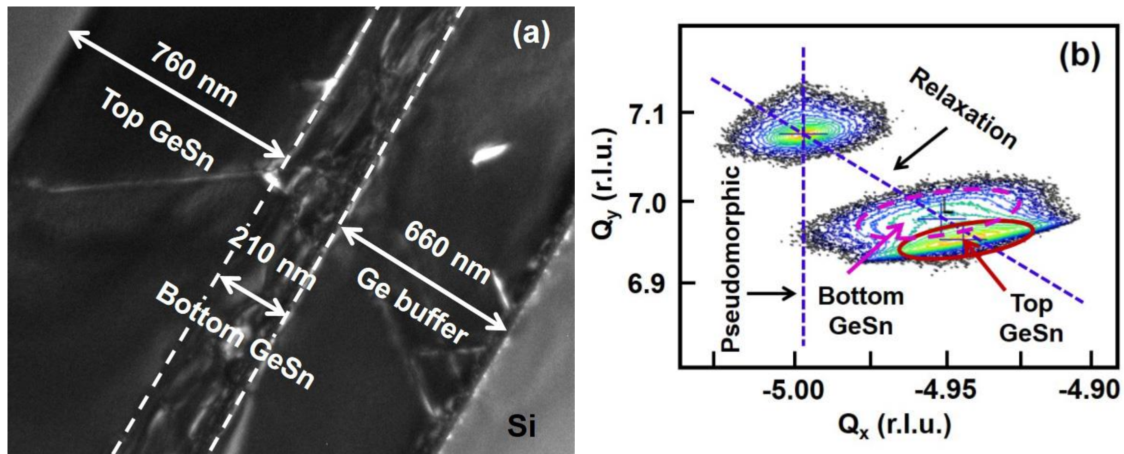

Figure 5.1. (a) Cross-sectional view TEM image (field emission electron gun with accelerating voltage of 300 kV, resolution of ~0.1 nm) showing two distinct GeSn layers: the bottom layer is defective and with lower Sn composition of 8.95% while the top layer is almost defect-free and with higher Sn composition of 10.90%. (b) RSM contour plot showing the superposition of bottom and top GeSn layers, which are both fully relaxed [85].

The Sn composition in the top GeSn layer was measured as 10.90%, which is ~1/5 more than that of the bottom GeSn layer. The higher Sn composition in the top GeSn layer might have been due to the ease of Sn incorporation when the underneath layer is relaxed [113]. The reciprocal space map (RSM) of the sample is shown in Figure 5.1(b). The broadened contour plot of GeSn indicated the existence of two layers. The part annotated by dashed ellipse corresponds to the bottom GeSn layer, whereas the solid ellipse part featuring full relaxation is associated with the top GeSn layer. The XRD rocking curve (data not shown here) showed a clear peak at 64.6^{o} and a shoulder at 64.9^{o}, corresponding to the top and bottom GeSn layers, respectively. The broadened GeSn peak (full-width half maximum of 0.21^{o}) compared to that of Ge peak (0.15^{o}) was due to the superposition of two GeSn layers with different Sn compositions [85].

5.2.2 Photoluminescence characterization

The temperature-dependent photoluminescence (PL) characterization was conducted to investigate the material quality. The PL measurements were performed using a standard off-axis configuration with a 532 nm continuous wave (CW) laser as an excitation source. The detailed PL setup description can be found in Ref. [16]. The PL spectra at temperatures from 300 to 10 K showed that as the temperature decreased, the PL peak intensity significantly increased, (Figure 5.2 inset, top right) revealing a typical characteristic of a direct bandgap material [96]. The PL emission wavelength of 2510 nm was observed at 300 K (no other emission was observed below 1800 nm), which featured a longer wavelength compared to a previous PL study of this group for a thin film sample with the same Sn composition [16]. This was mainly due to the relaxation of the GeSn resulting in a narrower bandgap. As the temperature decreased, the PL peak blue-shift

was observed, as shown in the Figure 5.2 inset (bottom, only selected temperatures shown for clarity). The full width at half maximum (FWHM) of each peak, extracted using Gaussian fitting, monotonically decreased as the temperature decreased. At 10 K, the extracted PL spectrum FWHM was 133 nm (28 meV) and was 1/4 of that of 300 K.

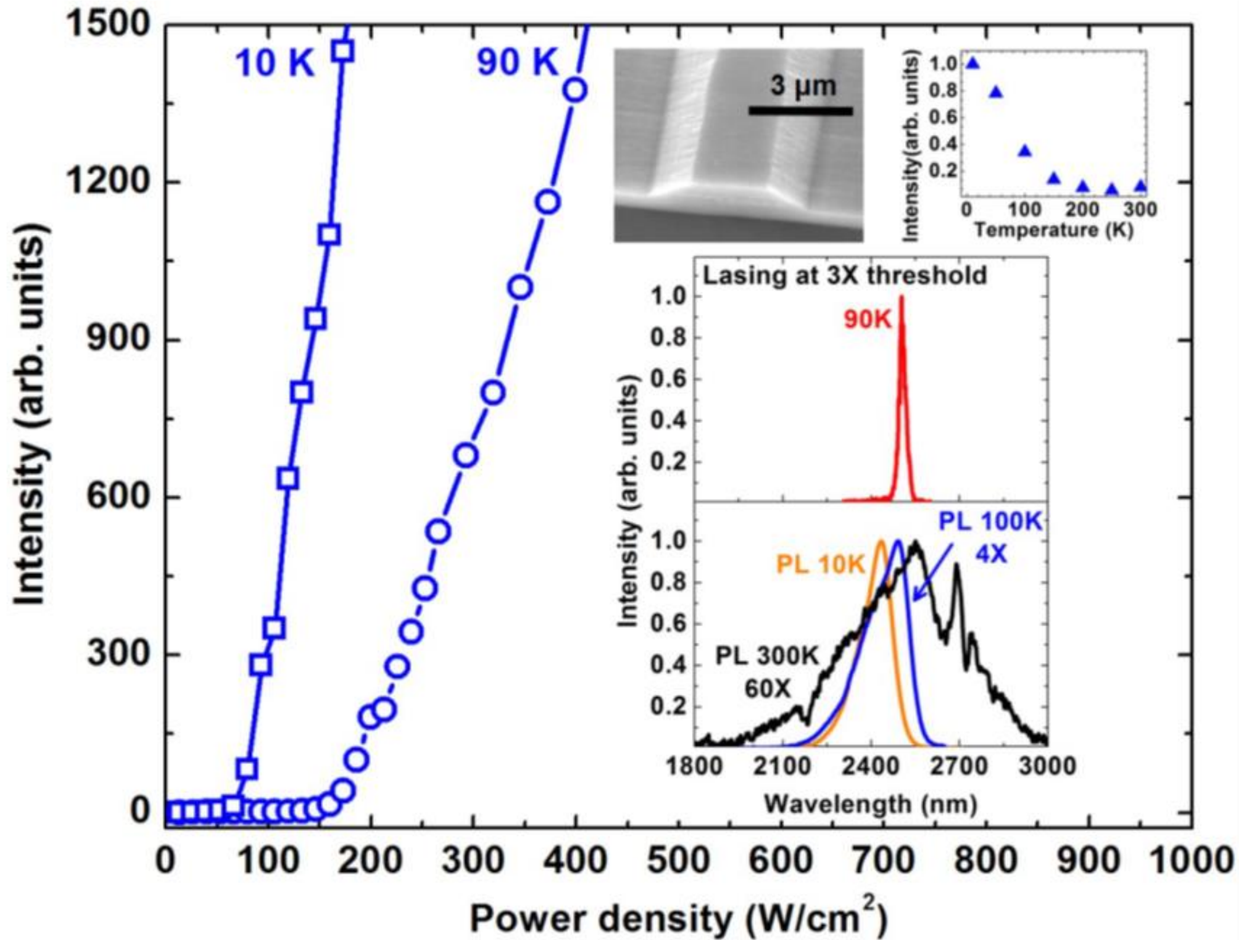

Figure 5.2. L-L curves of the 600 μm-long edge-emitting device at 10 and 90 K. Inset: (top left) SEM image of ridge waveguide device fabricated by a wet etching process; (top right) Temperature-dependent integrated PL intensity indicates the direct bandgap material of GeSn; (bottom) Optically pumped lasing spectra at 90 K. The PL spectra of the bulk sample at 10, 100, and 300 K are also plotted for comparison [85].

5.3 Fabrication process and device preparation

The sample was fabricated into a ridge waveguide with 5 μm width for optical pumping characterization. A low-temperature wet chemical etching process was developed in this study.

By using a mixture of HCl: H_2O_2: H_2O=1:1:10 at 0 °C, smooth sidewalls were achieved as shown in Figure 5.2 inset (top left). The average etching rate was ~20 nm/min. The etching depth was 800 nm. Due to the lateral etch, the waveguide width at the top was measured as 3 μm, while at the bottom was measured as 5 μm. Extensive etching study showed that the etching rate was almost constant at 20 nm/min regardless of the Sn composition. In addition, the wet chemical etching process did provide a smooth side wall, which could slightly reduce optical scattering loss for the waveguide structure. Therefore, the wet etching process developed in this work offered a robust recipe for the fabrication of GeSn-based devices. After etching, the sample was lapped down to ~70 μm followed by cleaving to form the mirror-like facets [85].

5.4 GeSn laser devices measurements

Devices with cavity lengths of 300, 600, and 1100 μm were investigated in an optical pumping experiment. The optical pumping characterization was performed using a pulsed laser operating at 1060 nm with 45 kHz repetition rate and 6 ns pulse width. The laser beam was collimated to a narrow stripe (~20 μm width and 0.3 cm length) via a cylindrical lens to pump the GeSn waveguide structure. Since the spatial intensity profile of the laser beam featured Gaussian distribution, the knife-edge technique was applied to determine the pumping power density [114-115]. The device was first mounted on a Si chip carrier and then placed into a continuous flow cryostat for low-temperature measurement. The emission from the facet was collected by a spectrometer and then sent to a thermoelectric-cooled lead sulfide (PbS) detector with the cut-off at 3.0 μm. The integrated emission intensity was measured by setting the grating at zero order.

5.5 Evidence of achieving GeSn lasers

Figure 5.2 shows the laser-output versus pumping-laser-input (L-L) curves of the 600 μm-long device at 10 and 90 K. The threshold characteristic was clearly observed. The threshold values were measured as 68 and 166 kW/cm^2 at 10 and 90 K, respectively. The low resolution (1 nm) directional emission spectrum measured at 3 times the threshold at 90 K is plotted in Figure 5.2 inset (red peak). The FWHM of the peak is 26 nm (5.1 meV). Compared to the FWHM of the PL peak at 10 K (28 meV), the dramatically reduced line-width further confirmed the lasing characteristic. The emission spectrum measured at 10 K (not shown) also revealed a similar FWHM of 28 nm (5.6 meV), which is comparable with that of previously reported GeSn lasers [21]. The laser operating wavelengths were determined as 2476 and 2503 nm at 10 and 90 K, respectively [85].

In order to further investigate the lasing mode characteristics, the device with a cavity length of 300 μm was studied. The L-L curve of the device at 10 K is plotted in Figure 5.3 shows a threshold of 106 kW/cm^2. The high-resolution spectrum (0.1 nm, spectrometer limit) measurement was performed for the device operating at 2x and 5x threshold (Figure 5.3 inset). Due to the relative large area of the cavity facet, the device spectra showed a typical multimode lasing characteristic. The spectrum taken under 2x threshold showed multi-peaks located between 2400 to 2500 nm. As the pumping power increased to 5x the threshold, most peaks grew and the overall intensity increased.

The 1100 μm-long device was selected for a detailed temperature dependent characteristic study since the longer length cavity reduced the mirror loss and therefore enabled the exhibition of the intrinsic characteristics of the material. The L-L curve showed that the lasing operation could reach as high as 110 K, as shown in Figure 5.4. The measured thresholds

ranged from 87 to 396 kW/cm^2 at temperatures from 10 to 110 K. The characteristic temperature, T_0, was further studied. By fitting the temperature-dependent lasing threshold, T_0 was extracted as 65 K, as shown in Figure 5.4 inset. T_0 was also extracted from L-L curves of 300 and 600 μm-long devices as 78 and 90 K, respectively [85].

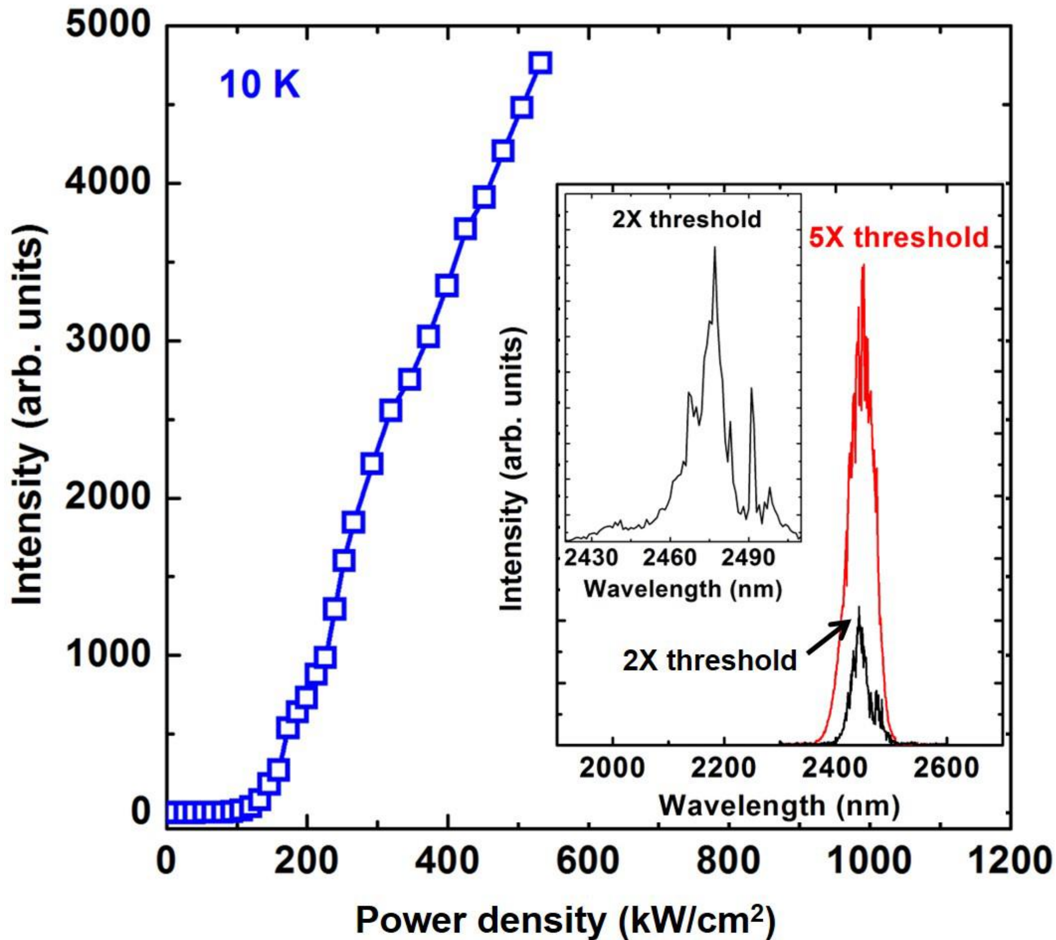

Figure 5.3. L-L curves of the 300 μm-long edge-emitting device at 10 K. Inset: The high-resolution spectra under 2× and 5× threshold pumping power [85].

Since many factors such as facet quality, waveguide quality, and cavity length could cause variation of T_0, 65 K was conservatively chosen as the feature T_0 for the GeSn laser in this study. The characteristic temperature measured at low-temperature range provides useful

information to benchmark the material with the early phase development of III-V material for laser applications. For example, according to earlier studied III-V optically pumped lasers, the reported T_0 were 100 and 129 K for InP/InGaAsP/InP and GaAs/AlGaAs/GaAs DHS devices, respectively [116,117].

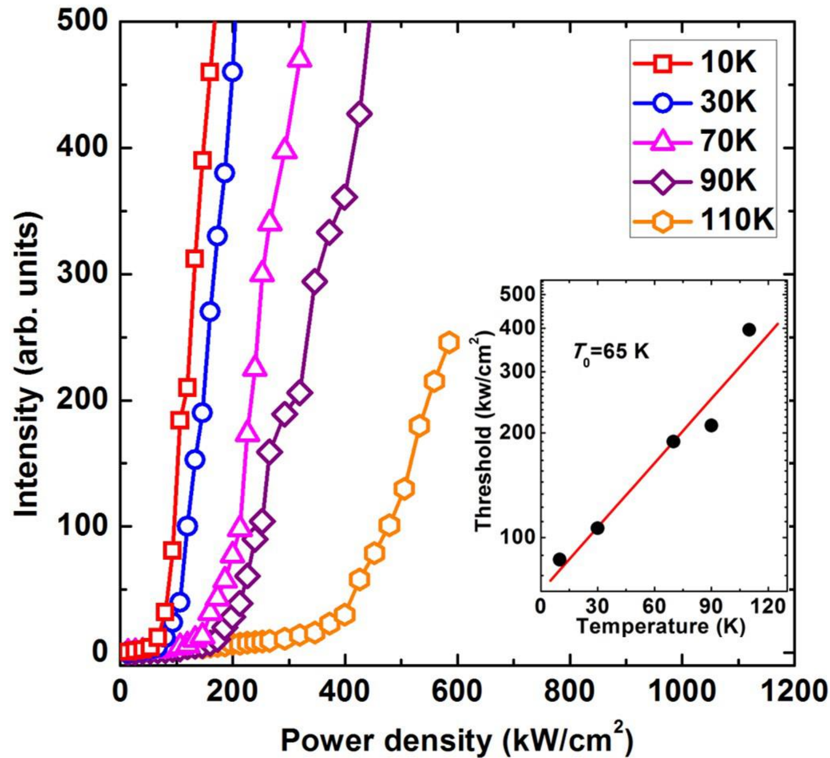

Figure 5.4. L-L curves of the 1100 μm-long edge-emitting device taken at the temperatures from 10 to 110 K. Inset: Laser threshold versus temperature for the purpose of fitting T_0 [85].

5.6 Band structure and modes profile

To shed light on lasing behavior, the band structure and the waveguide mode profile were calculated. Figure 5.5(a) shows the band structure of the sample at 300 K (not to scale) obtained using the effective mass and 6-band K·P method [80, 118]. It is clear that both GeSn top and bottom layers are direct bandgap. The conduction band (CB) barrier heights at Ge buffer/bottom GeSn, bottom/top GeSn, and top GeSn/Ge cap interfaces were calculated as 24, 37 and 55 meV,

respectively, indicating that the DHS provides electron confinement at both Γ- and L-valleys. However, considering the thermal energy at room temperature (~26 meV), the barrier of Ge buffer layer does not offer sufficient electron confinement [85].

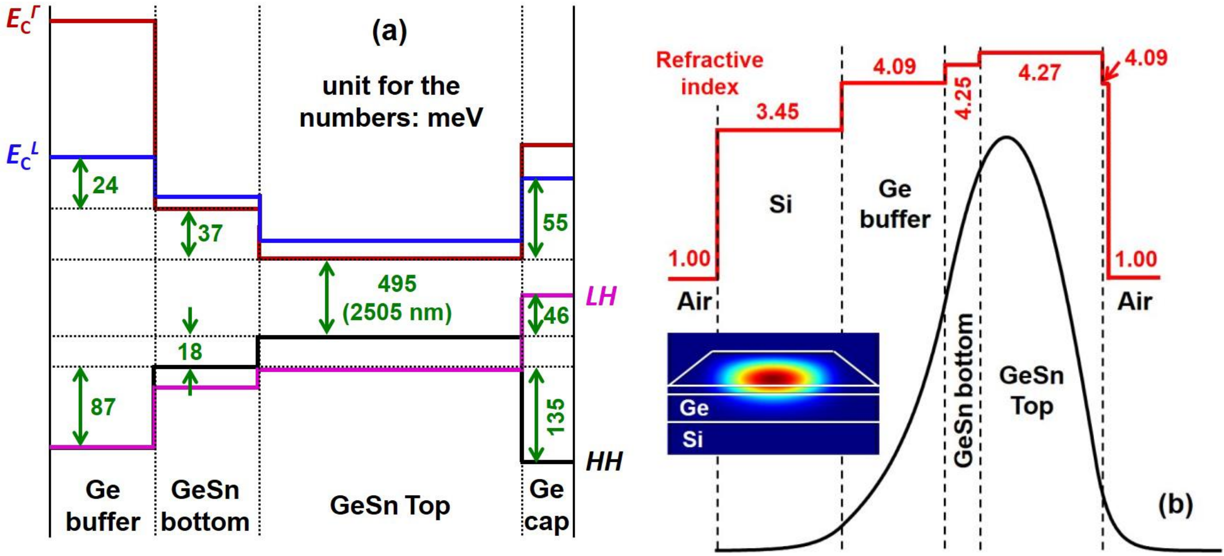

Figure 5.5. (a) Band structure of the sample at 300 K (not to scale; unit for the numbers: meV). (b) Profile of the fundamental transverse electric (TE_0) mode. The refractive index of each layer is plotted to indicate the optical confinement. Inset: cross-sectional profile of TE_0 mode [85].

Within the valence band (VB), the heavy holes (HHs) were confined in GeSn with barrier heights of 87 and 135 meV between the Ge buffer/GeSn layers, and the GeSn/Ge cap layers, respectively. However, due to the 1.5% tensile strain of Ge cap layer, the light-hole (LH) band was lifted well above the HH band, resulting in insufficient LH confinement since the LH minimum of Ge cap layer was 46 meV above the HH minimum of the top GeSn layer. But since the thickness of Ge cap layer was as thin as 10 nm, only a small fraction of LHs is confined in this layer. Hence, the majority of transitions took place in GeSn layers.

Figure 5.5(b) shows the pattern of fundamental transverse electric (TE0) mode obtained using a 2D mode solver. The input parameters for the calculation were the layer stack of the waveguide with an etching depth of 800 nm and the refractive index of each layer, which was

obtained from ellipsometry spectroscopy study, as shown in Figure 5(b). Since the wet etching process produced the inclined sidewall, the gradually increased waveguide width from 3 to 5 μm (from top to bottom of 800 nm etch depth) was used for the calculation, as shown in Figure 5.5(b) inset. Due to the relatively thick GeSn layer, the overlap of TE0 mode with GeSn layers was calculated to be 85%, with optical field confinement factors of 67% and 18% for top and bottom GeSn layers, respectively. Since the refractive index of Ge is close to that of GeSn, the optical field penetrates into the Ge buffer layer, resulting in an overlap of the optical mode with Ge buffer layer of 14% [85].

5.7 GeSn laser devices performance

Analysis of the merits of material growth and the device structures leading to the lasing achievement are summarized as follows:

First, the use of GeH4 in GeSn growth provides a favorable relaxation of material, which not only improves the material quality but also makes the direct bandgap GeSn achieved with lower Sn composition.

Second, based on ellipsometry study, the refractive index of GeSn is slightly higher than that of Ge, therefore, the relatively thicker GeSn (~1 μm) and thinner Ge buffer (700 nm) configuration, rather than thin GeSn active layer and thick Ge buffer layer structure, could offer a better optical field confinement in GeSn layer, which increases modal gain.

Third, the Ge/GeSn/Ge DHS structure offers an improved carrier confinement according to the band structure analysis. Note that since the bottom GeSn layer features lower Sn composition compared to the top GeSn layer, at a lower temperature, its wide bandgap confines the carriers in the top GeSn layer and, therefore, prevents them from recombining in the

defective bottom GeSn layer, resulting in more effectively injected carriers and enhanced radiative recombination.

On the other hand, issues regarding the laser performance included:

1- The operating temperature. The maximum lasing temperatures reported in Refs. [21] and [84] with GeSn bulk structure and high-Q micro-disk cavity are 90 K and 130 K, respectively, thus the maximum operating temperature of 110 K with DHS in this work is very reasonable. Since theoretical prediction for the highest achievable lasing temperature for DHS laser is 200 K, [78], there is a little room to increase the operating temperature by optimizing the DHS.

2- The carrier lifetime. So far there has not been systematic work reporting the carrier lifetime of GeSn. Recently, a ultra-fast pumping probe method was used to study the carrier dynamics in GeSn, [119] however, results obtained were inconclusive. A preliminary study was conducted in this research group (Dr. Shui-Qing Yu) on carrier bulk lifetime by using a photoconductor based testing structure, which revealed that the average carrier lifetime ranged from a few tens to hundreds of nanoseconds for bulk GeSn sample with the layer thickness of 500 nm and Sn composition of 9% at different temperatures [120].

3- The cavity length-dependent lasing behavior. Theoretically, longer cavity features lower mirror loss compared to the shorter cavity. The threshold of the 1100 μm-long cavity device should be lower than that of the 600 μm-long cavity device at the same temperature. However, since the reflection facet of the cavity was formed by sample cleaving and the facet plane was not parallel to the growth direction (~35.3^{o} relative to the growth direction) due to the epitaxy layer grown on (100) Si wafer, the facet

conditions for different devices could be different. It is believed that the lower quality facet of the 1100 μm-long cavity device resulted in its higher threshold. Moreover, due to the different conditions of facet cleaving for each device and the complexity of multimode lasing, it was quite difficult to identify the mode spacing in this study.

4- The external quantum efficiency (EQE). The EQE is a key figure of merit in an emitter device. However, since the output emission power could not be accurately measured due to instrument limitations, EQE was not discussed in this work.

5- The mode confinement. The overlaps of fundamental TE mode with the defective bottom GeSn and Ge cap layers were 18% and 14%, respectively, which led to optical loss. This could be improved by growing a relative thicker cap layer to increase the mode overlap with the high quality top GeSn layer.

6- The carrier confinement in the top GeSn layer. The barrier between the top and bottom GeSn layers did not offer sufficient carrier confinement at a higher temperature. This resulted in the thermally activated carrier transfer from top to bottom GeSn layer which led to the non-radiative recombination in the defective GeSn layer and, therefore, increased the laser threshold. At a temperature above 110 K, no lasing was observed due to the dramatically enhanced non-radiative recombination. A viable solution for this issue would be the insertion of a wide-bandgap interlayer between the top and bottom GeSn layers to enhance the carrier confinement in the top GeSn layer.

7- The cap layer selection. The tensile-strained Ge cap layer could not provide effective hole confinement, as the LH minimum of Ge cap layer was above the HH minimum of the top GeSn layer. This increased the recombination process occurring in the Ge cap layer and, consequently, increased the lasing threshold. This issue can be solved by using

an alternative cap layer such as SiGeSn alloy, whose lattice constant and bandgap energy can be engineered separately. The Type-I band alignment with sufficient barrier heights can be achieved by using optimized SiGeSn/GeSn/SiGeSn DHS according to the theoretical study [121].

5.8 Summary

In summary, the Ge/GeSn/Ge DHS laser sample was grown using an industry standard CVD reactor and low cost commercially available precursors in a single run epitaxy process. The use of GeH_4 provided a favorable relaxation for the GeSn material. TEM images showed a two layer GeSn film where a defect-free top GeSn layer was obtained. A wet chemical etching process was developed to fabricate the ridge waveguide with smooth sidewalls achieved. Temperature-dependent characteristics of laser-output versus pumping-laser-input were investigated. Unambiguous lasing operation was observed up to 110 K. The laser mode was analyzed via high-resolution PL spectra, which revealed the multimode operation of the laser. The lasing threshold and operation wavelength were measured as 68 kW/cm^2 and 2476 nm at 10 K, respectively. Based on the temperature-dependent threshold, a characteristic temperature of 65 K was extracted. According to the band structure calculation and the lasing mode profile analysis, an optimized solution for laser structure was proposed which could reduce the lasing threshold and increase the operating temperature. The capability of producing the GeSn laser in a “manufacture ready” process (industry reactor, low-cost precursor, and single run epitaxy process) indicates the great potential of GeSn to be easily adopted by a future foundry for integrated photonics applications when the material is mature.

Chapter 6. Systematic study of GeSn edge-emitting lasers

6.1 Introduction

In the last few years, great achievements were made in Si-based lasers, such as Si Raman laser, Er-doped Si, and Ge lasers that are compatible with CMOS processes [122-123]. However, monolithically Si-based lasers with high efficiency are a challenge. Development of new growth techniques offers opportunities to achieve GeSn lasers with high efficiency. Growing a direct bandgap GeSn with high Sn composition, tunable bandgap, and high material quality provides more control to build GeSn lasers with desirable wavelengths to be involved in complete components of integrated photonics.

In this chapter, demonstration of optically pumped GeSn lasers with a complete set that cover from 2 to 3 μm of wavelength range is presented. Thick and relaxed GeSn films with high quality materials were grown for laser devices. The composition range of Sn in GeSn alloys was from 7.3% to 17.5%. Material characterization was performed on these samples using TEM, XRD, and SIMS techniques. Moreover, temperature-dependent PL was studied to confirm directness and high quality of targeted GeSn samples. GeSn laser devices with several cavities, lengths, and widths were fabricated using both wet and dry etching. Optical pumping measurements were done at different temperatures to characterize the edge-emitting GeSn laser devices. Temperature operation, temperature characteristic, threshold, and modes were explored.

6.2 Growth information, material, and optical characterization

6.2.1 Growth information

Eight GeSn samples were grown using an ASM Epsilon® 2000 (RPCVD) system. The thickness of GeSn layers was from 500 to 1100 nm, and the Sn composition was in the range of

7.3% to 17.5%. The samples included either two or three GeSn layers. There were two approaches used to grow the samples. First, spontaneous-relaxation-enhanced (SRE) incorporation process of Sn was used. The nominal Sn composition was targeted and Sn incorporation up to 12% was reached due to the GeSn relaxation. The second approach was using GeSn as a virtual substrate (VS) to assist the increase of the Sn composition up to 17.5% with high-quality material. Samples A - C were grown with the VS method and samples D - J using the SRE approach. More details of growth techniques were reported in Ref. 92. Table 6.1 shows the information about the thickness of the Ge buffer, Ge cap if it was included, and the thickness and composition of each GeSn layer for each GeSn sample discussed in this chapter.

Table 6.1. Summary of GeSn samples information including Ge buffer thickness, thickness and composition of each layer of GeSn, and Ge cap thickness.

Sample	Ge Buffer Thickness (nm)	1st layer		2nd layer		3rd layer		Ge Cap (nm)
		Sn %	Thickness (nm)	Sn%	Thickness (nm)	Sn%	Thickness (nm)	
A	670	5.6	210	7.3	680			
B	620	8.3	280	9.9	850			10
C	540	9.4	180	11.4	660			10
D	650	10.5	250	14.4	670			
E	640	11.6	210	15.9	450			
F	783	9.8	160	12.7	680	16.6	290	
I	680	10	210	13	450	16.9	170	
J	640	11.9	310	15.5	550	17.5	260	

Each sample in Table 6.1 contained a defective layer on the bottom less than 250 nm in thickness. The second GeSn layer was relaxed and almost free of defects. Moreover, the second GeSn layer had a higher Sn composition and thickness compared to the first GeSn layer. The F, I, and J samples consisted of three GeSn layers. The third GeSn layer had a higher Sn composition than the two bottom layers as shown in Figure 6.1. The highest Sn composition that was achieved was 17.5%. The variety of Sn composition in GeSn samples provided an opportunity to investigate the impact of Sn composition on GeSn lasers to optimize the composition of GeSn active layers according to desirable wavelength and laser output.

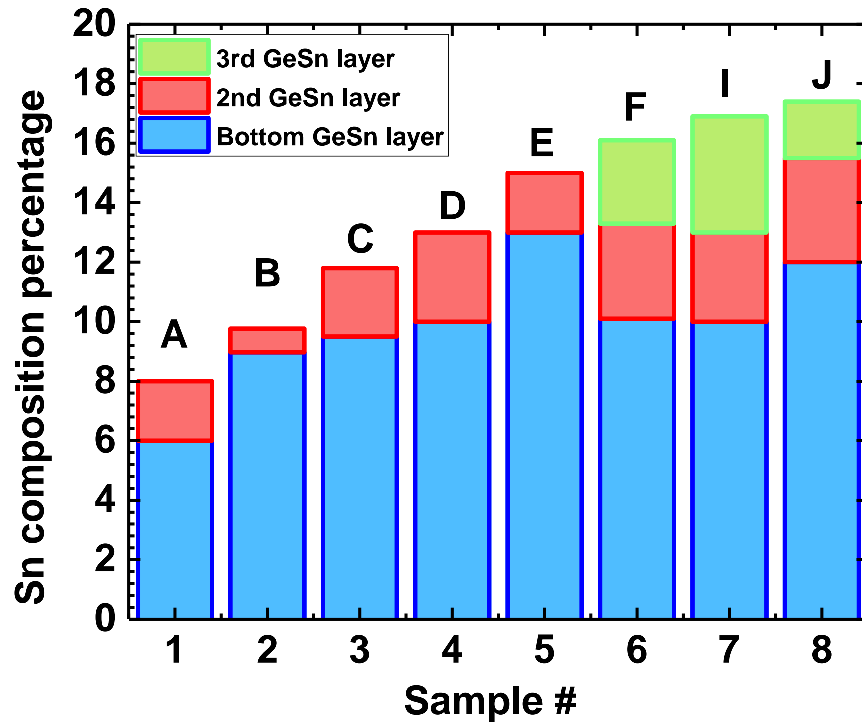

Figure 6.1 Sn composition and GeSn layers for each sample discussed in Chapter 6.

6.2.2 Material characterization

Material characterization such as TEM, XRD, and SIMS was done for all samples in this study to confirm the composition, thickness, and material quality. Figure 6.2 presents the TEM

images for two samples. Figure 6.2(a) shows the TEM image of Sample J with Si, Ge buffer, and GeSn layers. From the TEM image, the interface between Si and Ge shows the majority of defects, and the Ge buffer with 640 nm thickness appears to be high-quality material. The bottom layer of GeSn is a defective layer due to the threading dislocations of lattice mismatch between Ge and GeSn. The TEM image of Sample J shows three distinguishable GeSn layers. The thickness of the defective layer is about 210 nm and 12% Sn composition. The second GeSn layer had higher Sn composition at 15.5% and thickness of about 540 nm. The third GeSn layer was ~ 270 nm thick and had the highest composition of Sn, 17.5%. By using TEM and etch pit density measurements, a TDD of 10^6 cm^{-2} was obtained for the GeSn top layer while the TDD of Ge buffer layer was measured as 10^7 cm^{-2}.

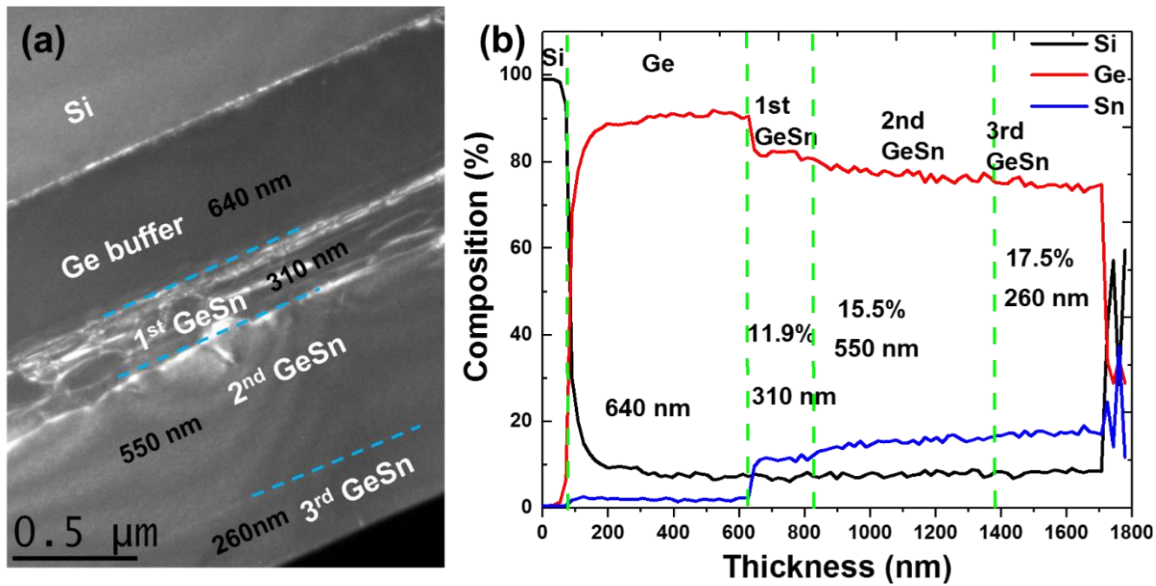

Figure 6.2. (a) The cross-sectional TEM image (field emission electron gun with accelerating voltage of 300 kV, resolution of ~0.1 nm) shows two distinct GeSn layers of Sample J. (b) EDX plot presents the thickness and layer composition of Ge buffer, and three GeSn layers with different thickness and Sn % of Sample J.

The EDX in Figure 6.2(b) presents three layers of GeSn layers and provides information about composition and thickness of each layer of Sample J. There is a distinguishable interface

with high defects between the first and second GeSn layers. However, the interface between the second and third GeSn layers is not defective due to the gradient of Sn composition from 15.5 to 17.5% and the lattice constant of both layers being close.

TEM and EDX were done for other Samples from A to I (not shown) to investigate the quality and confirm thickness and composition. High-quality materials for both two and three GeSn layers of Samples A to I were determined through TEM images. Other material characterization such as XRD, RSM, and SIMS (not shown) were done for all samples to study strain, relaxation of the films, lattice constants, and composition. However, these type of measurements for high quality and thickness and strain-free GeSn films were thoughtfully studied in Chapter 4 and 5. Information using these techniques is provided for Samples A to J in Table 6.1.

6.2.3 Photoluminescence characterization

Achieving lasing from bulk GeSn alloys requires many significant factors to be tested and studied. First, the GeSn samples must be direct bandgap materials. Second, the material quality must be good to reduce the defects. Third, the GeSn film must be thick enough to provide sufficient gain and enhance the confinement of carriers.

PL results at room temperature indicate that the peak position shifted to longer wavelengths as the Sn composition increased as illustrated in Figure 6.3(a). From the PL study, all GeSn samples in Figure 6.3 were direct bandgap with only one main peak for the transition from Γ valley to the valence band. The peak position of direct bandgap GeSn films of these samples at RT covers a wide range of wavelengths starting from 2286 nm for 7.3% (Sample A) to 3225 nm for 17.5% Sn (Sample J). With optimization of the Sn composition and thickness,

wavelengths longer than 3500 nm can be covered. The additional peaks at 2600 and 3000 nm were due to the atmosphere and water absorption. The PL results at 10 K show high intensity with narrower FWHM compared to RT measurements. The peak position at 10 K shifted to a shorter wavelength than the wavelength at RT for the same samples as presented in Figure 6.3(b).

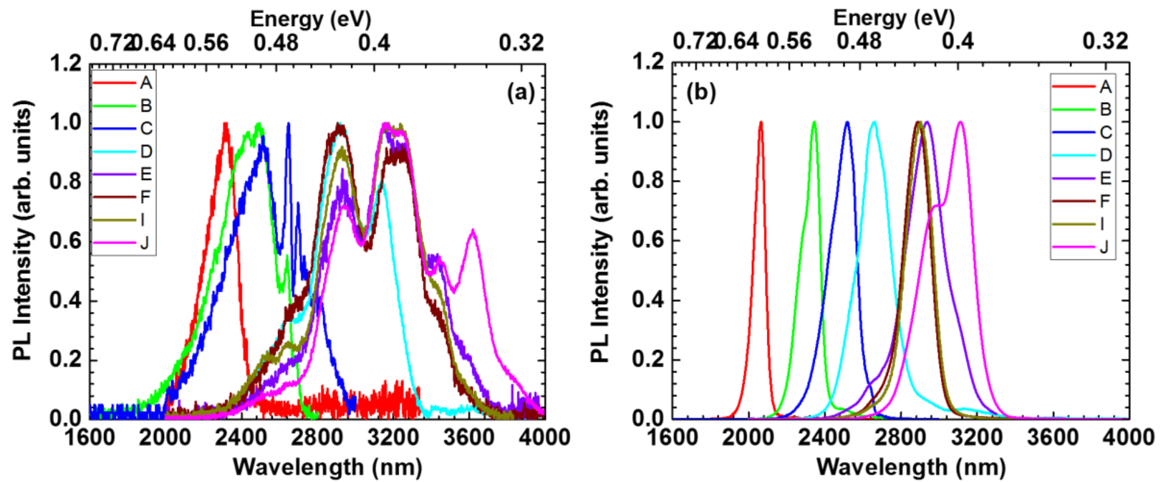

Figure 6.3. Normalized PL spectra of samples A-J at (a) 300 K and (b) 10 K. As the Sn composition increases, the PL peak shifts towards longer wavelength due to the reduced bandgap energy. The main peaks are assigned to the direct bandgap transitions for all samples.

Temperature-dependent PL measurements were done to investigate GeSn samples at different temperatures. The temperature-dependent PL indicated that the intensity at low temperature was tens of times higher than the PL intensity at RT. The FWHM of all samples from A to J at low temperature was narrower than at higher temperatures. The single peak of transition, higher intensity, and narrower FWHM at low temperature are considered as evidence for the directness of the GeSn film bandgap. The temperature-dependent PL for Sample A and J are presented in Figure 6.4. The temperature-dependent PL results of other GeSn Samples from B to I (not presented in this chapter) showed a similar behavior of increasing the PL intensity and

reducing FWHM at a lower temperature. Figure 6.4(a) and (c) illustrate the temperature-dependent of Samples A and J. The integrated PL intensity at 10 K was 40 times greater than 300 K for Sample A and 48 times more for Sample J. Moreover, the integrated PL intensity and FWHM versus temperature of Samples A and J are shown in Figure 6.4(b) and (d). The FWHM at 10 K was three times less than at 300 K for Sample A (around 60.9 meV at 300 K to 16.6 meV at 10 K) and two and a half times less for Sample J (88.6 and 39.9 meV at 300 and 10 K respectively). The integrated PL intensity for both samples increased with decreasing temperature.

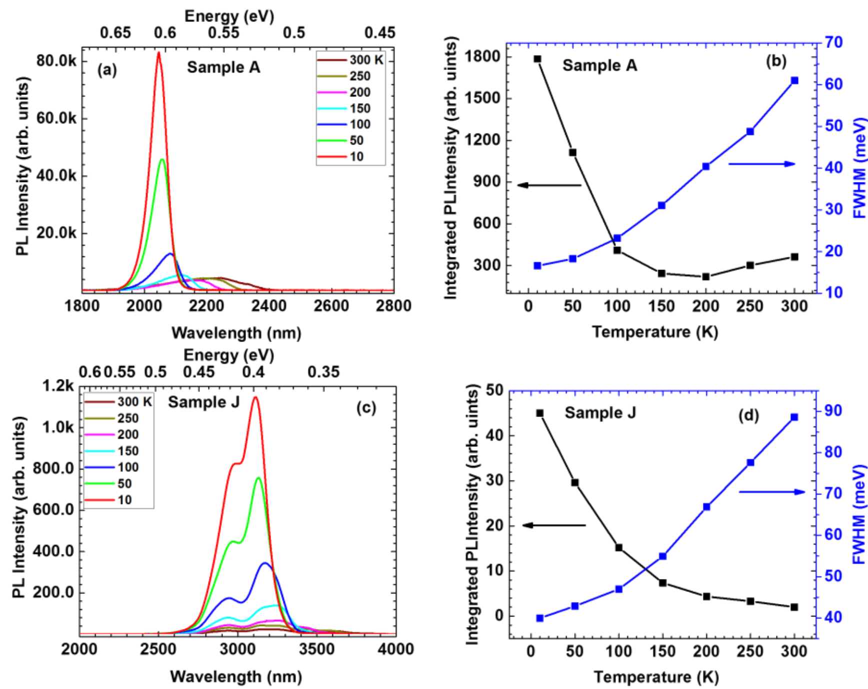

Figure 6.4. Temperature-dependent PL spectra of GeSn for (a) Sample A, (c) Sample J. The corresponding FWHM and integrated PL intensity against temperature are plotted in (b) Sample A, (d) Sample J.

6.3 Device fabrication and measurement conditions

Samples from A-J were fabricated using wet and dry etching at different etching depths depending on sample thickness, structure, and refractive index to optimize etching depth and

obtain a high confinement factor. As a comparison, the width of the top of the device was less than the bottom of the device when the wet etching technique was used. However, using the dry etching method, both the top and bottom sides of the device were almost the same. The etching depth was between 500 to 900 µm using both wet and dry etching techniques. Figure 6.5 shows some SEM images for selected samples to show the facets and sidewalls for both wet and dry etching. The SEM images in Figure 6.5(a) and (b) present the wet etching for Sample C, and (c) and (d) for Sample J. Furthermore, dry etching of Sample B is shown in Figure 6.5(e) and (f).

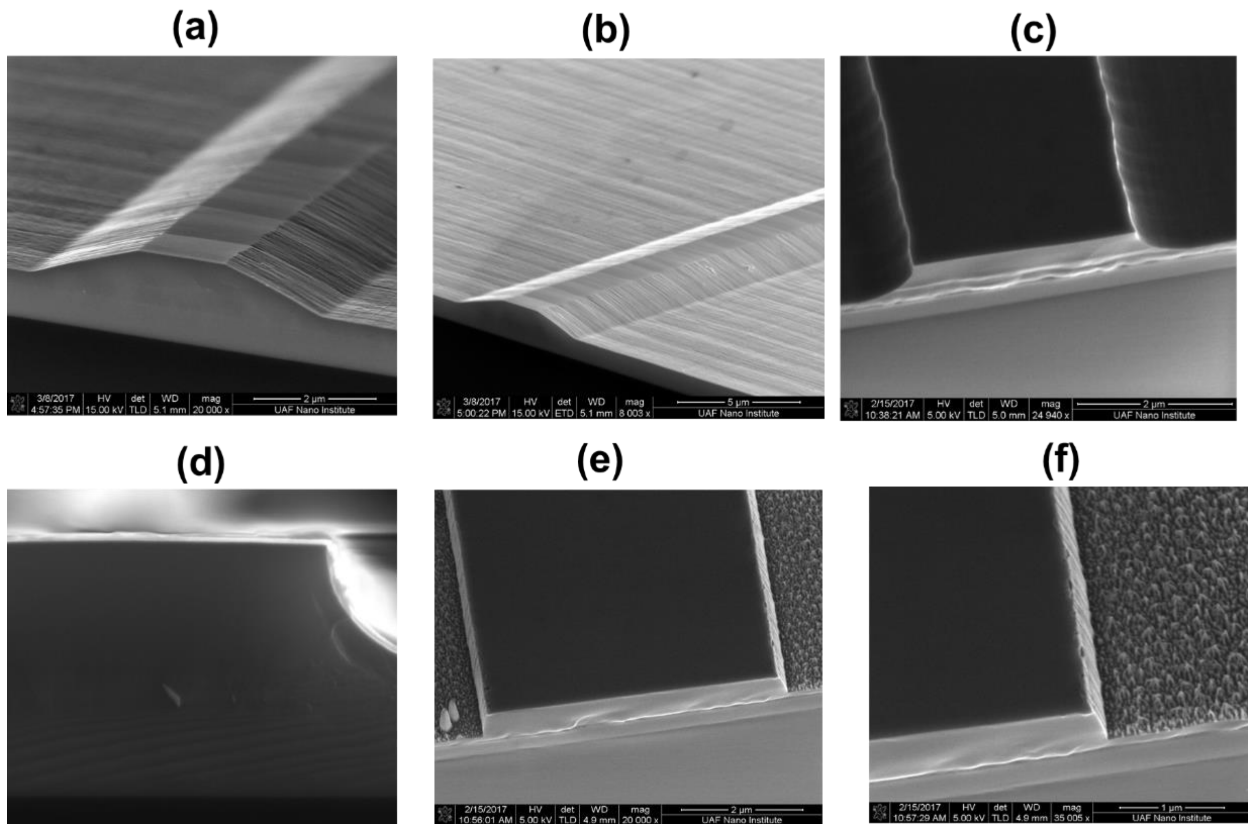

Figure 6.5. SEM images for GeSn laser devices for facets and sidewalls. (a) and (b) wet etching of Sample C; (c) and (d) wet etching of Sample J; and, (e) and (f) dry etching of Sample B.

After the devices were fabricated, lapping processes were applied to reduce the thickness of samples to a few tens of microns. Lapping the samples provided better results with cleaving

processes and was done easily. Cleaving was done for several cavity lengths, such as 250, 300, 400, 500, 600, 750, 1000, 1200 µm, and longer.

A pulse 1064 nm laser was used for optically pumped measurements. The repetition rate of the laser was 45 kHz, and the pulse width was 6 ns. Each set of devices with 1, 2, 3, 4, and 5 µm of width was cleaved with the same cavity length on the same piece of sample. Then three pieces with different cavity lengths were uploaded to the cryostat at the same time. The entire 15 devices were measured under the same conditions to compare the results each time that devices were loaded inside the cryostat. The cryostat was pumped to reduce pressure to assist with the stability of temperature for low-temperature measurements. Both liquid helium and nitrogen were used to test the devices from 10 K or 77 K to the higher temperature operation possible for each device.

6.4 Lasing at different Sn compositions

The samples selected to study the lasing from GeSn samples were with several Sn compositions from 7.3% to 17.5%. The wavelengths corresponding to these GeSn laser samples range from around 2 to 3 µm as shown in Figure 6.6. The lasing wavelength of Sample A was 2070 nm and 2827 nm for Sample J, both at 77 K. The spectra for samples A-J in Figure 6.6(a) were measured from 77 K to 180 K. All samples were lasing at 77 K. However, some samples stopped lasing as the temperature increased. Samples A and I were not lasing at 110 K, and only five samples were lasing at 140 K. Figure 6.6 shows only Sample D and J were lasing at 160 K. The maximum temperature operation was reached by Sample J at 180 K and corresponding wavelength 2987 nm. The lasing wavelength of all samples are summarized in Table 6.2.

Table 6.2. Summary of GeSn laser devices measurements including a lasing wavelength at 77 K, the threshold value at 77 K, temperature characteristic, and temperature operation.

Sample	Laser wavelength (nm)	Threshold (kW/cm^2)	T_0 (K)	Temperature operation (K)
A	2070	300	N.A.	90
B	2400	80	76	140
C	2461	160	103	140
D	2627	138	73	160
E	2660	267	N.A.	100
F	2767	150	84	140
I	2704	96	N.A.	110
J	2827	171	73	180

The reduction of FWHM of GeSn laser spectrum for Samples D and E compared to the linewidth of bulk GeSn spectrum for the same sample and at the same temperature was 3.5 times, and higher. Other samples A-J showed similar behavior. Figure 6.6(b) and (c) illustrates the reduction of FWHM of lasing of Sample D and E comparing to PL of the same sample at 77 K. The FWHM of PL of Sample D was 4.5 times broader than laser spectrum (40.1 meV of PL spectrum to 8.8 meV of laser spectrum). The reduction of linewidth is evidence for lasing behavior. The spectrum laser of Sample J at 180 K had a wavelength operation at 2987 nm. This wavelength was the longest operation wavelength from GeSn lasers was achieved.

6.5 GeSn lasing threshold

The lasing threshold is one of the key points for any laser device. With a lower lasing threshold, the device is more desirable to reduce power consumption and be used for different

applications. There are several factors that can affect the threshold value of any laser such as the type of material, structure, thickness, device dimensions, facets, etc. The threshold values of GeSn laser samples are different depending on thickness, compositions, facets, and sidewalls of the devices.

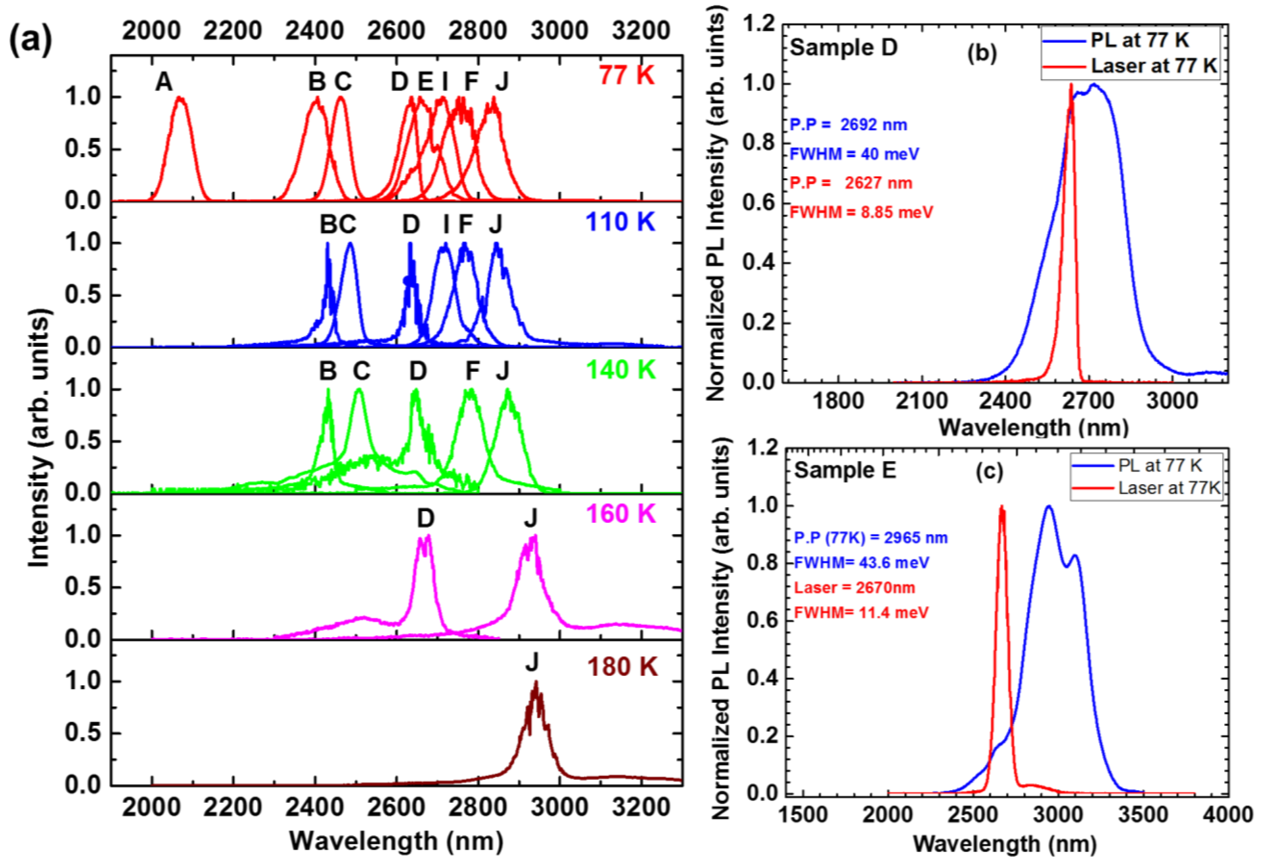

Figure 6.6. GeSn laser performance characterization. (a) Spectra of GeSn lasers fabricated from samples A to J at temperatures from 77 to 180 K. (b) and (c) Lasing spectra at 77 K of samples D and E compared with PL spectra. The lasing peak blue-shifted due to the typical band filling effect.

Figure 6.7(a) presents the lasing threshold of all samples from A-J at the same temperature (77 K). These GeSn laser devices were selected because they had better facets and sidewalls compared to other devices for each sample. At 77 K, the lasing thresholds for all samples were obtained ranging from 80 to 300 kW/cm^2.

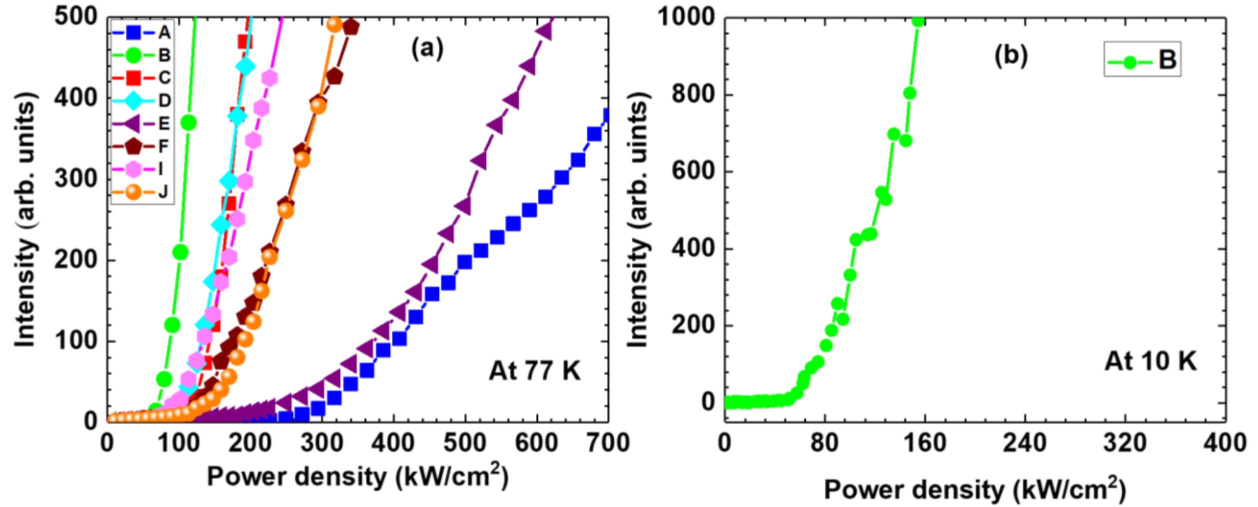

Figure 6.7. (a) L-L curves of Samples A, B, C, D, E, F, I and J versus power density (kW/cm^2) at 77 K. (b) L-L curves of Sample B at 10 K.

The lowest lasing threshold was from Sample B at 80 kW/cm^2 that came from the highest thickness of GeSn active region. The highest threshold was from Sample A at 300 kW/cm^2; sample A had the lower composition, 7.3% Sn. From L-L curve at 10 K, the lowest lasing threshold value was 45 kW/cm^2 at 10 K for Sample B (dry etching) as shown in Figure 6.7(b) with a reduction of 30% below the last lowest reported value 68 kW/cm^2 [85].

6.6 The impact of GeSn film thickness on the GeSn lasers

Studying the impact of the thickness of the GeSn film on the lasing behavior of these materials was important to optimize the structure of each sample with targeted Sn composition. Four GeSn samples, B, D, E, and I, were selected to study the impact of thickness on the lasing behavior. The total thickness of the GeSn layers for these samples were 1000, 910, 590, and 830 nm, respectively. Figure 6.8 presents the laser output versus pumping laser-input (L-L) curves at 77 K to demonstrate the impact of GeSn layer thickness on the lasing performance.

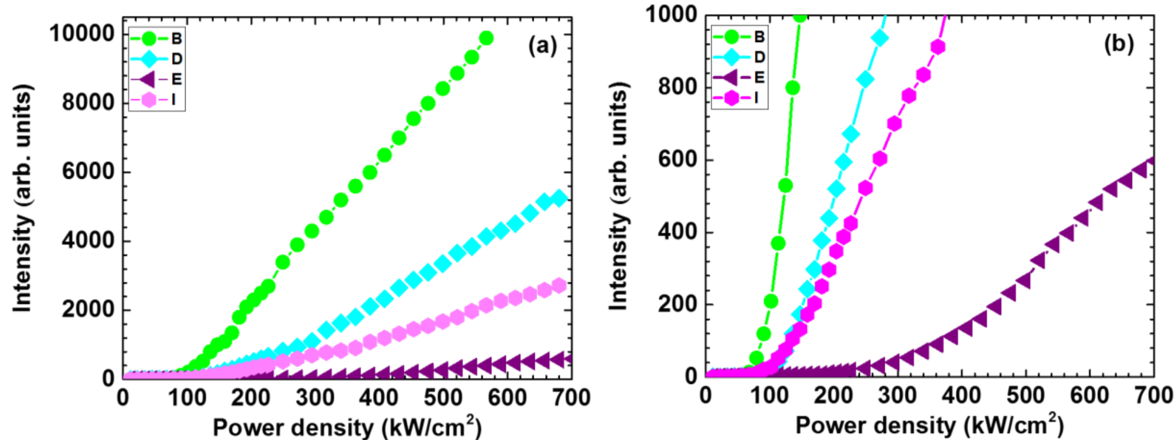

Figure 6.8 L-L curves of Samples B, D, E, and I versus power density (kW/cm^2) at 77 K shows the impact of thickness on threshold and intensity.

From Figure 6.1 and Table 6.1, Sample B had lower Sn composition (9.9%) compared to Samples D, E, and I. Nevertheless, Sample B with greater total thickness (1130 nm) and 850 nm of top GeSn layer showed the lowest lasing threshold of 80 kW/cm^2. In contrast, Sample E, which was the thinner sample with 660 nm of total thickness and 450 nm of top GeSn layer, had the highest threshold, around 267 kW/cm^2. Furthermore, the intensity of Sample B was highest, two times more than Sample D, four times more than Sample I, and 16 times more than Sample E as presented in Figure 6.8. The reasons that thicker GeSn layers show higher intensity and lower threshold can be explained as: (1) the confinement factor becomes greater with increasing the thickness of GeSn active layer for provided refractive index values of similar structures as presented in Figure 5.5 (b); (2) the penetration depth of the 1064 nm laser is more than 1000 nm at low temperature. Therefore, the absorption increases with increasing the thickness, and more carriers are generated.

6.7 Power dependence of lasing spectrum

The GeSn laser spectrum was sensitively studied for Sample A-J at different

temperatures and excited laser power. The measurements of the spectrum of laser provide numerous details about the GeSn laser device performance, such as the intensity, operating wavelength, linewidth, and threshold area. The device of Sample C with 1 mm cavity length and 5 μm width was selected due to the highest value of intensity distinguished FWHM reduction below, at, and above the threshold as shown in Figure 6.9.

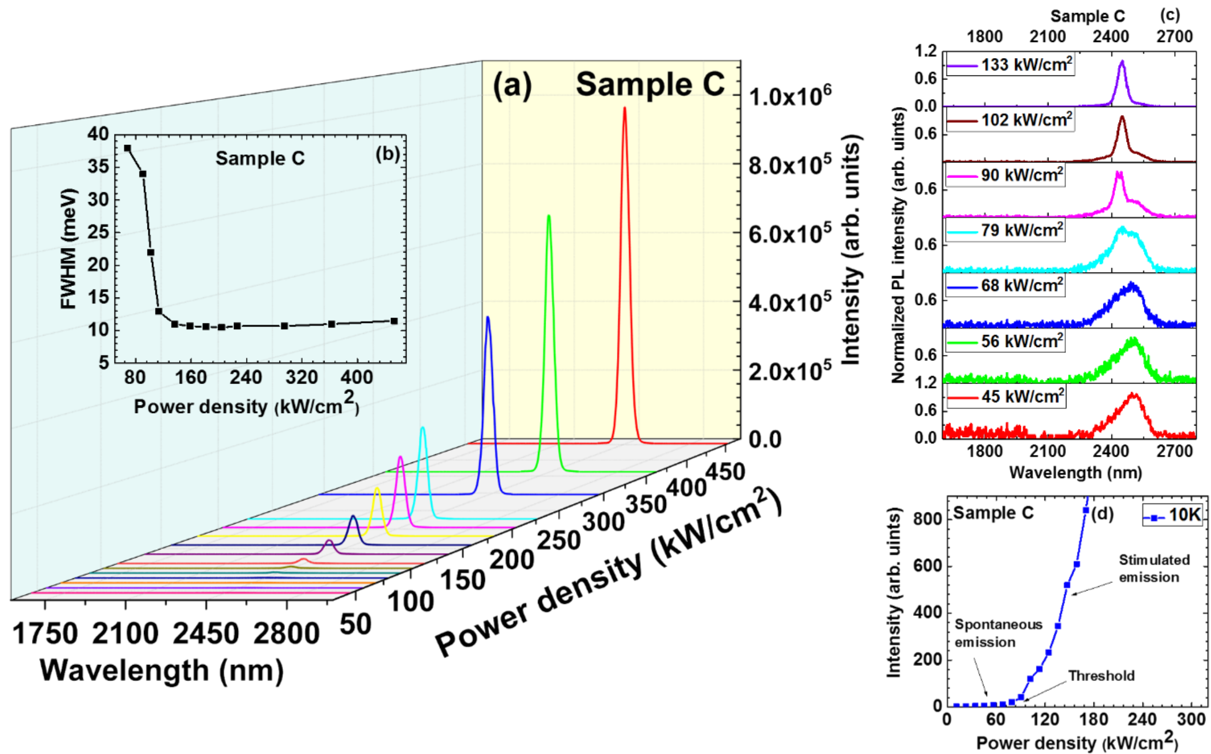

Figure 6.9. The spectrum measurements of Sample C at 10 K. (a) The power-dependent lasing spectrum from 45 to 454 kW/cm^2 of power density. (b) The FWHM of the spectrum at several power densities. (c) The spectrum around the threshold area is changing from spontaneous to stimulated emission of spectrum below above the threshold. (d) The L-L curve shows the output intensity from laser device below, at, and above threshold areas.

The wavelength of laser operation of this device was 2449 nm at 10 K. The intensity increased rapidly with increase in the excited laser power of the laser source as presented in Figure 6.9(a). The integral of the spectra (area under the curve) at 453 kW/cm^2 was 540 times higher than at 45 kW/cm^2.

Figure 6.9(b) shows the linewidth reduction as the power density increased. The FWHM of laser spectra was high below threshold (around 38 meV) and reduced as the threshold level was reached to become a minimum value (10.5 meV) at the lasing point. Then it increased to 11.5 meV as the excited power increased due to the heating effect. The change of spectrum shape, intensity, and linewidth below and around threshold level are illustrated in Figure 6.9(c). Below threshold from 45 to 80 kW/cm^2, the spectrum was due to spontaneous emission. The power density was not enough to inject enough carriers to generate lasing. Therefore, the linewidth was broad, and the intensity was low. Moreover, the internal and external loss was more than gain inside the device. Around 80 kW/cm^2, there was a change in spectrum shape and linewidth, but there was still no lasing. This value was the threshold level. Above the threshold value (80 kW/cm^2), the lasing started, the linewidth became narrower, and the intensity rapidly increased as illustrated in Figure 6.9(d). In this range of power density above the threshold, the net optical gain became higher than the total loss.

6.8 Study of the modes of GeSn lasers

Lasing modes are important to be investigated as evidence of lasing for any laser devices. The modes are generated inside the laser cavity (Fabry-Perot) when the gain becomes more than the loss just above the lasing threshold. There are a lot of modes separated by the distance that can be calculated from the equation:

$$\Delta\lambda = \frac{\lambda^2}{2n_g L} \qquad \text{(Equation 6.1)}$$

Where $\Delta\lambda$ is the mode spacing, λ is the mode wavelength, n_g is the group refractive index, and L is the cavity length. The spacing mode decreases with increasing cavity length. Therefore, due to the limitations of spectrometer resolution, the mode spacing is difficult to calculate for longer

cavity lengths. Moreover, cleaving a short cavity less than 250 µm was a challenge. The modes of GeSn lasers were studied for different samples and at several temperatures and at several resolutions of the spectrometer. The modes at low resolution were measured with cavity lengths between 250 to 500 µm. Figures 6.10 and 6.11 present the modes of Samples B, D, and I at different power densities and temperatures.

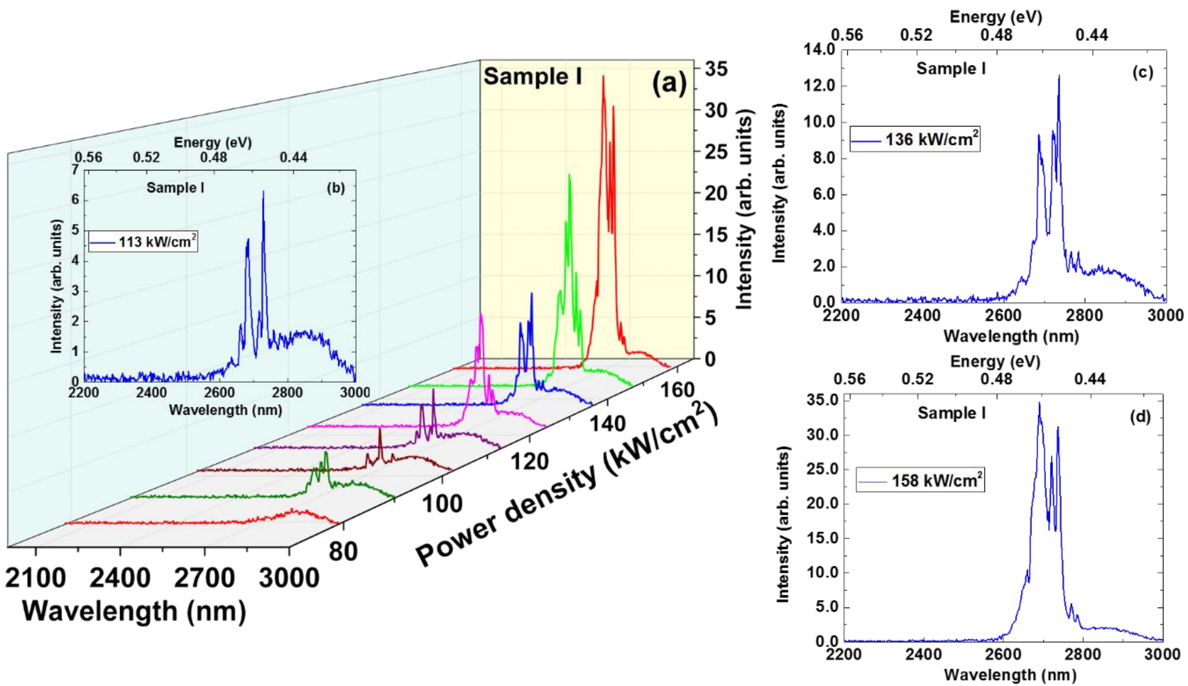

Figure 6.10. The GeSn laser modes at low resolution for Sample I. (a) Spectra at different power excitation to show the modes. (b) Spectra at 113 kW/cm^2. (c) Spectra at 136 kW/cm^2. (d) Spectra at 158 kW/cm^2.

The modes of Sample I at 77 K are shown in Figure 6.10. The low resolution measurements (increment = 2 nm) of Sample I at several power densities are presented in Figure 6.10(a). Below threshold (96 kW/cm2), the spectra were spontaneous emission and there were no mode oscillations inside the cavity. Nevertheless, lasing modes of GeSn started to appear just above lasing threshold with many modes. Then, the intensity of the modes increased as the

power density increased. All power densities were selected between $0.8P_{th}$ (76.8 kW/cm^2) to less than $2P_{th}$ (192 kW/cm^2) to show the modes close to threshold area. As, the power density was increased more than $2P_{th}$, there was only one peak (modes overlap) of lasing emission shown. Figure 6.10(b), (c), and (d), present individual spectra at 113, 136, and 158 kW/cm2 of power density respectively to demonstrate clear low resolution modes. At a pumping power density slightly higher than the lasing threshold, the multi-peaks revealing the lasing modes can be observed clearly. As the pumping power increased, the modes became more pronounced and most peaks grew, resulting in the overall lasing intensity increase.

Figure 6.11 presents low resolution (2 nm) for multimodes of Samples B and D at different temperatures and power densities. These multimodes were measured above the lasing threshold at several temperatures to show the modes of GeSn lasers at various operation temperatures. Figure 6.11(a) illustrates the multimodes of Sample B at 158 $kW/cm^{2,}$ and 110 K. Due to the shift of peak position (red shift) with increasing the temperature, the main peak of lasing wavelength was different at each temperature. Figure 6.11(b) and (c) presents the low resolution multimode of Sample D at 136 and 680 kW/cm^2 and 77 and 150 K, respectively. The linewidth of the mode was around 3 nm as shown in Figure 6.11(b).

The extra PL peak on the left shoulder of spectrum at 2550 nm in Figure 6.11(c) corresponds to the lower GeSn layer due to the high power density of laser source around 680 kW/cm^2. High resolution (0.5 nm) cavity modes for Sample C at 340 kW/cm^2 of power density and 10 K are presented in Figure 6.11(d). The slit width of the entrance and exit of the spectrometer was reduced for high-resolution measurements 1/7 the slit width at low resolution. The spacing between the cavity modes (the distance between the center of two neighbor modes) of GeSn laser device of Sample C was 0.36 meV. This value of spacing between modes is

comparable with the value reported in Ref 21.

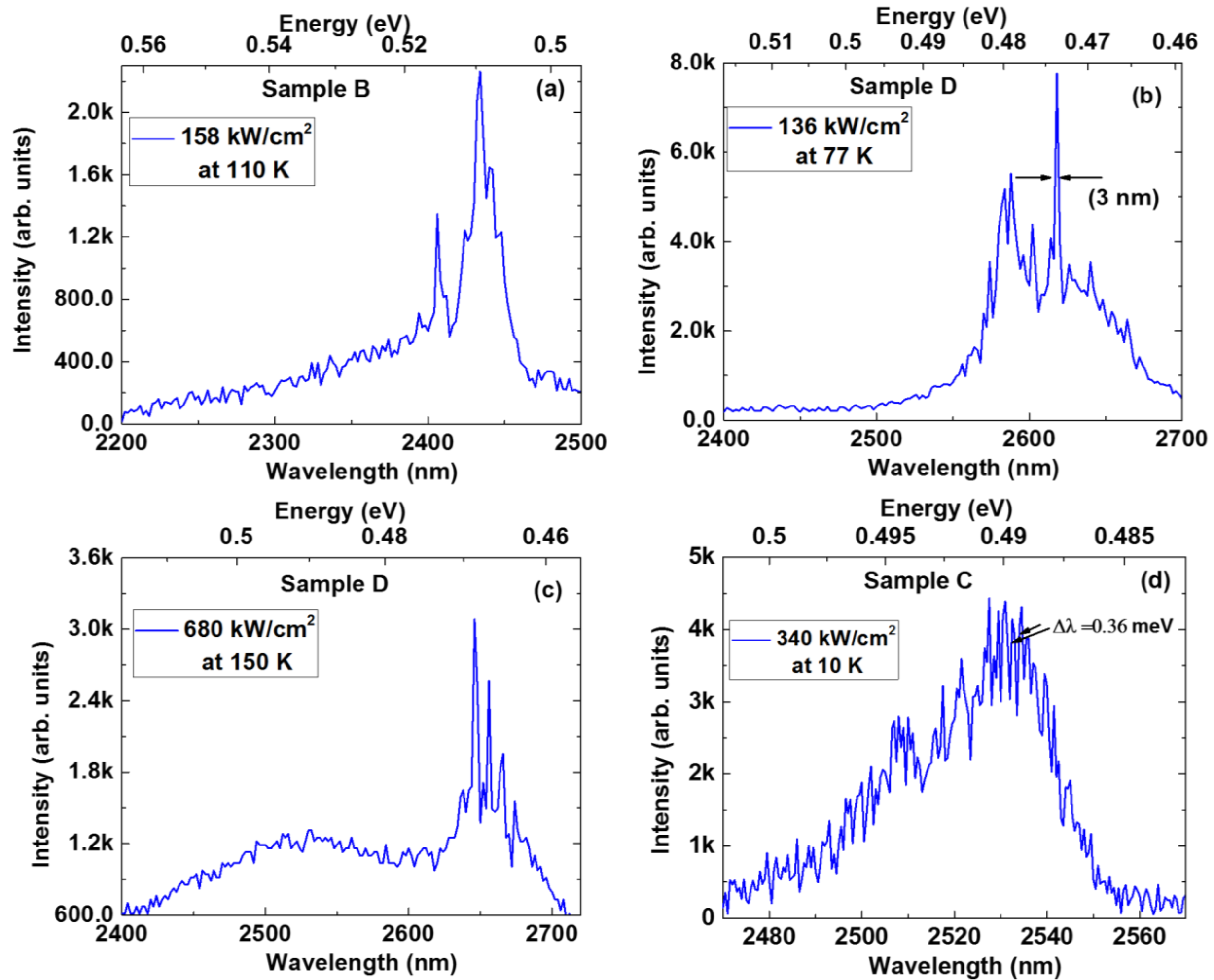

Figure 6.11. The modes measurements of GeSn lasers. At low resolution; (a) Sample B at 110 K. (b), (c) Sample D at 77 and 150 K, respectively. (d) High resolution measurements and 1 mm slit width for Sample C at 10 K.

6.9 Temperature operation of edge-emitting GeSn lasers

Obtaining a laser from a new material such as GeSn is an interesting achievement. However, one of the important factors is to achieve a laser operating at high temperature up to room temperature and higher. Therefore, studying the operating temperature of GeSn lasers was necessary. From theoretical calculations, the maximum operating temperature for GeSn laser from the bulk structure is around 200 K [78].

All samples A-J were measured at different temperatures to understand the trend of GeSn lasing with changing temperature and, also, the maximum temperature that each sample could reach. The first temperature operation of the bulk GeSn laser was reported as 90 K [21], then 110 K [85]. Three samples were selected to show higher temperature operation than what was reported in previous studies. These three, presented in Figure 6.12, were Samples C, D, and J. The maximum temperature operation was 140, 160, 180 K for Samples C, D, and J respectively. The temperature operation of other GeSn laser samples are summarized in Table 6.2. Figure 6.12(a), (c), and (e) show the L-L curves with a range of intensity to demonstrate how the intensity reduces with increasing temperature of the same sample due to nonradiative recombination processes that increase with temperature. The L-L curves also illustrate the threshold increases as the temperature increases because of loss increases (especially internal loss that is related to free carrier absorption). For instance, the threshold of Sample C increases from 122 kW/cm^2 at 10 K to 505 kW/cm^2 at 140 K. Sample C was measured from 10 to 140 K using liquid He. However, both Samples D and F were measured using liquid N_2 due to non-availability of liquid He at the time of the measurements.

The characteristic temperature, T_0, of a GeSn laser is one of the indications of device performance at different temperatures. A large value of T_0 is desirable because the threshold does not change much with temperature. It can be calculated using the following equation,

$$P_{th}(T) = P_{th}(T_a)\, e^{(T-Ta)/T_0}, \qquad \text{(Equation 6.2)}$$

where P_{th} is the power at the threshold and T_a is a chosen temperature. T_0 can be experimentally determined by plotting the threshold versus temperature. The y-axis is plotted as log scale and T_0 is equal to 1/slope as shown in Figure 6.12(b), (d), and (f). Temperature-dependent measurements were done from 10 to 140 K for Sample C using liquid helium and from 77 K to

160 K and 77 K to 180 K for Sample D and J, respectively, using liquid nitrogen. The characteristic temperature was 103 K for Sample C and 73 K for Samples D and J.

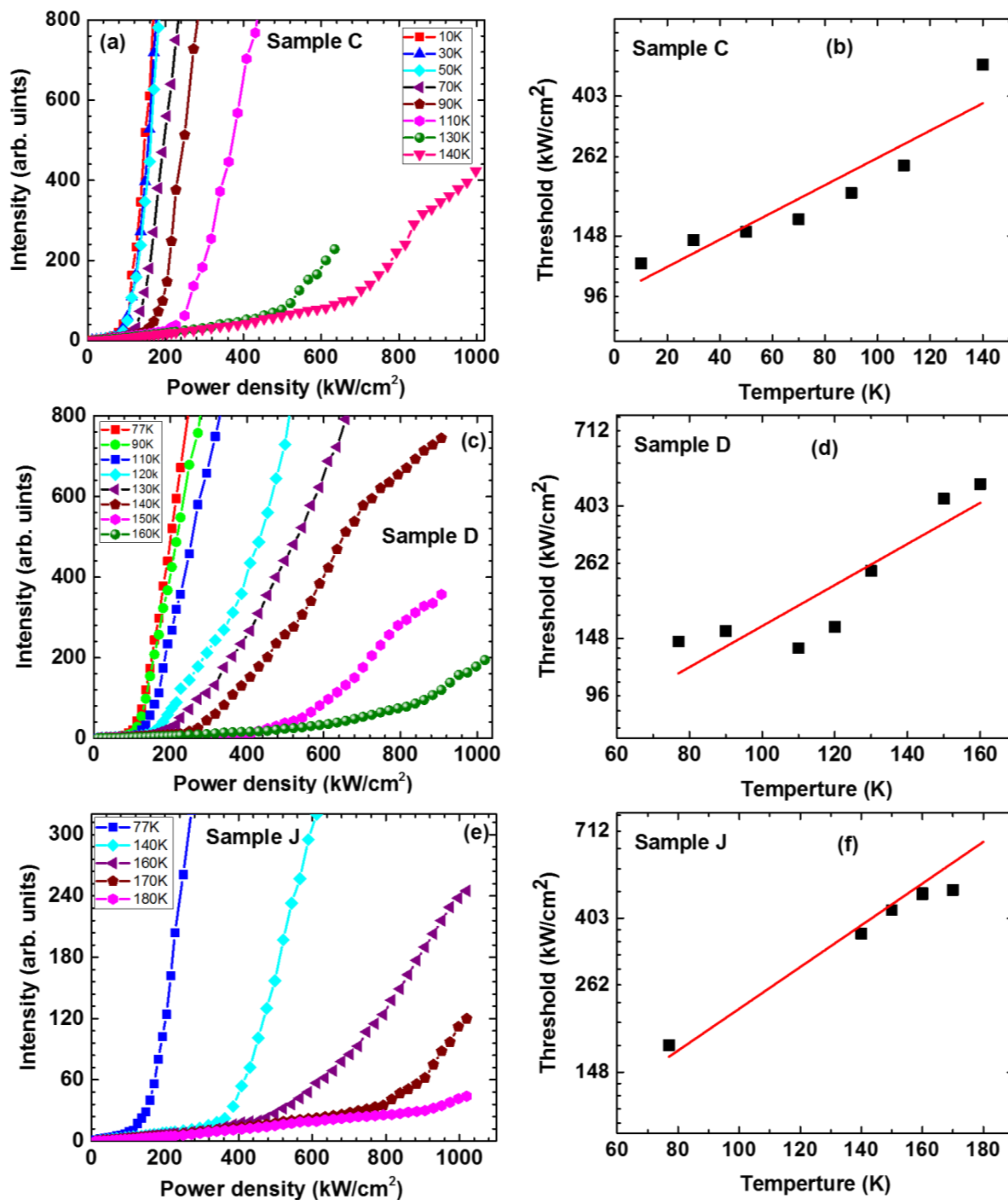

Figure 6.12. Temperature-dependent L-L curves presented for samples (a) C, (c) D, and (e) J. The characteristic temperature shown for samples (b) C, (d) D, and (f) J.

6.10 Band diagram calculation

The band diagram was calculated for Samples D and J using the effective mass and 6-band k·p method at 300 K as shown in Figure 6.13(a) and (b). These calculations were based on Sn composition, thickness, and strain of GeSn layers. The calculation was done for Ge buffer and two layers of GeSn for Sample D, and for Ge and three GeSn layers of Sample J. The E_{cL}, $E_{c\Gamma}$, E_{vhh}, and E_{vlh} represent energy levels of L- and Γ-valleys at conduction band (CB), and heavy hole (hh) and light hole (lh) at valence band (VB), respectively. The direct bandgap energy of 0.476 eV of Sample D agrees well with the measured PL peak position of 2610 nm. For Sample J, there were four layers – Ge buffer, and three GeSn layers with different thickness and Sn composition. The three GeSn layers of Sample J were direct bandgap.

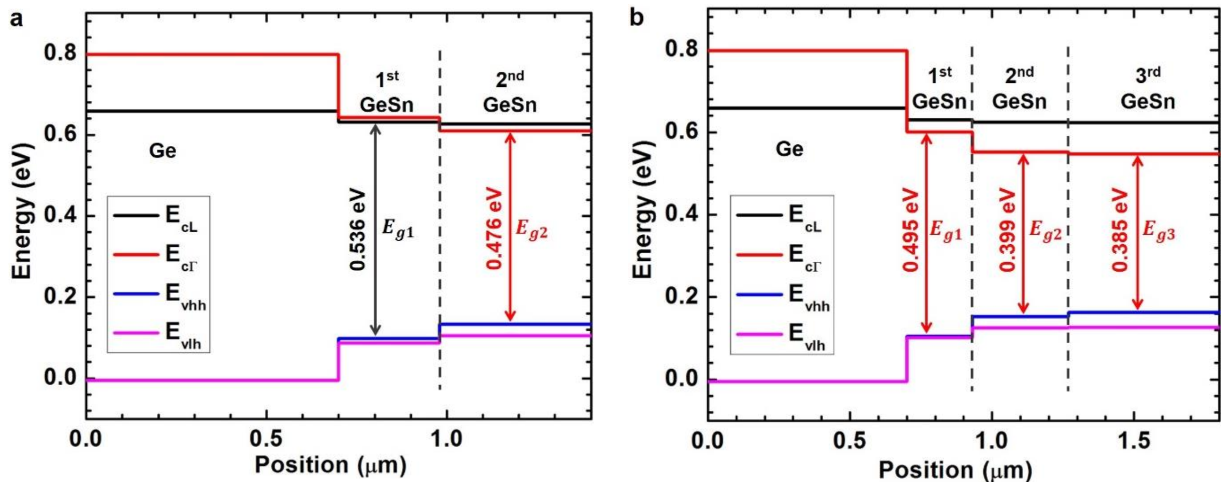

Figure 6.13. Band diagram calculation for Samples (a) D and (b) J at 300 K.

The bandgap energy of the third GeSn layer was less than that of the second layer and the bandgap of the second GeSn layer was less than that of the first GeSn layer as shown in Figure 6.13(b). Therefore, the wavelength corresponding to those layers increased going up to the top layers. Furthermore, there was agreement between the measured and calculated bandgap energy

of the top GeSn layer with PL peak position, 3225 nm. Based on the results of theoretical calculations, Samples A-J show a type-I band alignment with carrier confinement in the top GeSn layer.

6.11 Lasing mode pattern calculation

A 2D mode solver [124] was used to calculate the lasing mode pattern to study the fundamental transverse electric field (TE_0) mode. Figure 6.14 (a) shows the mode pattern of Sample D. The device was etched down to 800 nm of 1 µm total thickness of GeSn layers; the top of the waveguide width was 2 µm and bottom width was 5 µm. The refractive index (n) of Ge is 4.09 and for Si is 3.45. The refractive index of GeSn was chosen from Ref. 108 to be 4.25 for GeSn as presented in Figure 6.14(a). The confinement factor in the GeSn layer was around 85.2%, and 14.4% in the Ge layer for Sample D. Using these refractive index values for Si, Ge, and GeSn, the pattern mode for ideal case (dry etching) with top and bottom device width of 5 µm was calculated for comparison – see Figure 6.14(b).

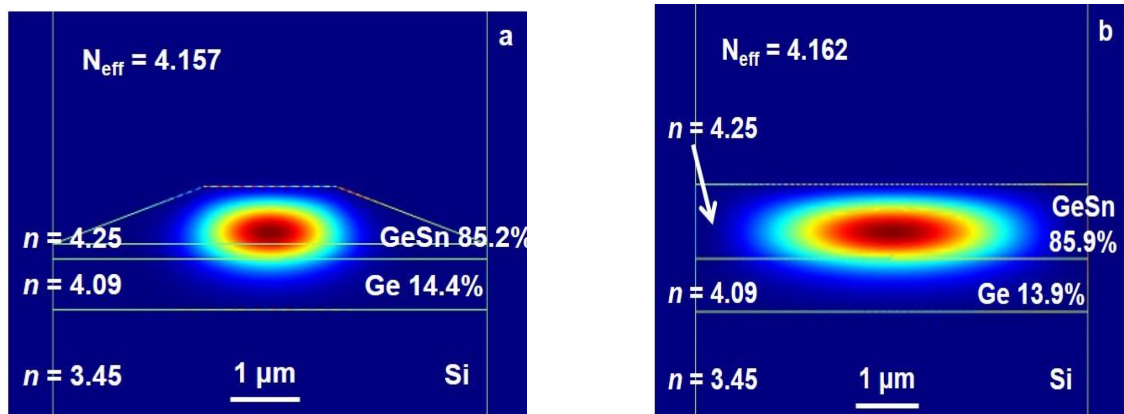

Figure 6.14. Calculated pattern of the fundamental transverse electric mode. (a) An actual device by wet etching and, (b) an ideal of waveguide with 90° sidewall. The N_{eff} is the effective index. The mode overlap difference with the GeSn layer is only 0.7% between two structures.

The confinement in the ideal case was 85.9% in the GeSn layer and 13.9% in the Ge layer. The difference in confinement between the ideal case and the real device of sample D was only 0.7%.

6.12 The performance of GeSn laser devices.

There were hundreds of devices that were tested to check the performance of GeSn lasers using samples with different compositions, thicknesses, and cavity lengths and widths. The longest wavelength operation was achieved from Sample J. The lowest threshold value was obtained from Sample B. The highest temperature operation was 180 K for Sample J; moreover, this is the highest temperature operation for GeSn lasers reported. Sample C showed the highest characteristic temperature at 103 K. The performance of edge-emitting GeSn laser devices is summarized in Table 6.2. Measuring the output power for GeSn laser devices is important as evidence for laser device performance. In the early stage of achieving lasing from new materials, it is difficult to measure output power because of its low value. Some GeSn laser devices showed very high intensity. However, due to the powermeter lower limit of measurement being a few tens of μW and having a high level of noise for the signal, output power measurements were difficult in the range of a few tens of μW. There is work in progress by this research group to measure the output power from GeSn laser devices and will be reported in future publications.

6.13 Summary

Optically pumped edge-emitting GeSn laser devices were investigated with several Sn compositions and active layer thicknesses. All GeSn samples discussed in this chapter were selected to be direct bandgap from 7.3% to 17.5% Sn composition. Some of these samples included two GeSn layers and others had three layers. The total thickness of GeSn layers was

from 500 to 1100 nm. Material characterization such as TEM, EDX, SIMS, XRD, and RSM were used to provide information about thickness, composition, lattice constant, and material quality. The top GeSn layer(s) showed very high material quality. Temperature-dependent PL was done to study the bandgap, enhancement of the intensity, and linewidth of the spectrum of each sample. The wavelengths corresponding to the PL of spectra of these samples covered a wide range from 2 to 3.4 μm. The integrated PL intensity of these samples at 10 K was more 40 times higher than at 300 K for all samples. The GeSn laser devices were designed with waveguide widths from 1 to 5 μm. The GeSn laser devices were fabricated using both wet and dry etching techniques with different etching depths. Several cavity lengths were targeted to be cleaved for each sample to study the behavior of GeSn lasers. The GeSn laser devices were characterized at different temperatures to determine the lasing threshold, lasing wavelength, intensity, temperature operation, and characteristic temperature for each sample. The GeSn lasing wavelengths covered from 2070 nm for Sample A to 2827 nm for Sample J at 77 K. The longest lasing wavelength observed was 2987 nm at 180 K for Sample J. The lowest threshold was obtained from Sample B with 80 kW/cm^2 at 77 K. The highest temperature operation was 180 K for Sample J. Furthermore, the characteristic temperature of 103 K for Sample C was the highest value for all samples.

Chapter 7. Summary and future work

7.1 Summary

The primary focus of this study was on GeSn alloys. The GeSn alloys were investigated from a fundamental understanding of the material to the device level such as lasers.

7.1.1 Thin GeSn films

A systematic study was done for thin GeSn films below 200 nm of thickness and from 0 to 12% Sn composition. Material characterization such as TEM and XRD were used to confirm thickness, strain information, and the composition of each sample. Strain had an impact on the quality of GeSn samples and bandgap as did Sn composition. Raman spectroscopy showed the impact of alloying Sn to Ge. From the PL study for thin GeSn films, GeSn became a direct bandgap at 10% Sn. The bandgap of GeSn reduced as Sn composition increased, and peak position shifted to a longer wavelength. The temperature-dependent PL indicated that the intensity decreased at low temperature for indirect bandgap GeSn and increased for direct bandgap. As the temperature decreased, the wavelength shifted to shorter wavelengths (blue shift). The FWHM decreased as the temperature decreased.

7.1.2 Doped thin GeSn films

N-type doped GeSn films were investigated to show the doping effect on the behavior of GeSn alloys. Material and optical characterization was done for doped GeSn films similar to un-doped GeSn films. Three samples at different Sn compositions and doping concentrations were compared to undoped films with the same % Sn. The bandgap shrunk for doped samples and peak position shifted to the longer wavelength. There was a large enhancement of PL intensity

for doped GeSn samples compared to undoped ones. High PL intensity at low temperature indicates that doped GeSn films are a good candidate for emitting devices.

7.1.3 Thick GeSn film

When the direct bandgap was achieved, next step was to find better material quality of GeSn with enhancement of PL and material gain for emitting device. Thick GeSn films with a thickness greater than 400 nm were thoroughly studied. The thickness of GeSn samples was selected between 400 to 1100 nm. Thick GeSn films showed a high material quality due to the relaxation of film confirmed by material characterization such as TEM (shown in Chapters 4, 5, and 6). From PL study, thick GeSn films showed direct bandgap material behavior at 7.3% Sn composition. Temperature-dependent PL showed very high enhancement in PL intensity. Integrated PL intensity at 10 K was more than 40 times higher at RT. Several laser sources with different penetration depths were used to investigate the effect of thickness on the PL and increase the material gain from thick GeSn films. The power-dependent PL using a 1064 nm laser demonstrated that the intensity was very strong with increasing power density due to the increased absorption inside the GeSn films. These characteristics make GeSn good for achieving lasers.

7.1.4 Optically pumped edge-emitting GeSn laser

Developing new growth approaches, such as spontaneous-relaxation-enhanced (SRE) deposition or using GeSn as a virtual substrate (VS), provided high material quality of GeSn with high Sn compositions. These techniques led to growing a strain relaxed GeSn films from 8 to 17.5% with a total thickness of GeSn layers from 500 to 1100 nm. The GeSn samples were

characterized using both material and optical characterization to provide the needed information about composition, thickness, the number of layers, material quality, bandgap, strain, and intensity of each sample. The GeSn device was designed to be from different strips of width from 1 to 5 µm and the same separation distance between each device. The GeSn devices were fabricated using both dry and wet etching techniques. The calculated mode confinement for both wet and dry etching devices showed there was a small difference between both structures of around 0.7%. The GeSn devices were cleaved for several cavity lengths, depending on the aim of the measurements, to study the impact of cavity length on device performance such as intensity, lasing threshold, and saturation level.

The edge-emitting GeSn laser devices were characterized using both liquid He and liquid N_2 to study the temperature-dependence of these devices. Some devices were measured starting from 10 K to maximum temperature operation of each sample. However, other devices were measured from 77 K to the maximum temperature that device could reach due the unavailability of liquid He during a portion of the research. All devices were compared at 77 K to confirm the device performance at the same temperature. The range of lasing wavelengths from samples with 7.3% to 17.5% Sn was from 2070 to 2827 nm at 77 K. The maximum lasing wavelength was 2987 nm at 180 K from 17.5% Sn sample, which is longest lasing wavelength which has been reported. The lowest lasing threshold was 45 kW/cm^2 from 9.9% ample at 10 K, and 80 kW/cm^2 at 77 K, which is the lowest threshold reported in literature for GeSn lasers. The highest temperature operation of GeSn laser device was 180 K for 17.5% Sn sample. Moreover, the highest characteristic temperature was 103 K for 11.4% Sn sample. Low and high-resolution modes were studied. The spacing mode of sample C was 0.36 meV at power density 340 kW/cm^2 and 10 K.

7.1.5 Summary of Key Observations

- Thin GeSn film with a thickness below 150 nm is a direct bandgap around 10% Sn composition alloying to Ge.
- The PL intensity of thin GeSn films increased at low temperature for direct bandgap and decreased for indirect bandgap.
- The linewidth of GeSn spectra decreased with decreasing temperature for direct bandgap.
- Raman spectroscopy showed a Raman shift to shorter wavenumber with increasing incorporation of Sn due to the change of lattice constant of GeSn alloys.
- N-type doping shrinks the bandgap of GeSn compared to the same composition of Sn in undoped GeSn films.
- The PL intensity of doped GeSn film is higher than un-doped GeSn film at the same Sn composition.
- The thick GeSn films above 400 nm of thickness shows high-quality material compared to lower than 400 nm thickness due to the relaxation of GeSn film with increasing the thickness of the GeSn layer.
- Most of the defects were seen in the first layer of GeSn around 200 nm of thickness; the top GeSn layer(s) was almost strain- and defect-free.
- There was a big enhancement in the PL intensity of thick GeSn films; some samples showed the integrated PL intensity at 10 K was 50 times more than the value at RT.
- GeSn material of more than 400 nm thickness was a direct bandgap at 7.3% Sn due to the relaxation of films.

- Thick GeSn samples (> 400 nm) indicated that GeSn films are a good candidate for lasing because of the high gain through increasing the power excitation injection of the laser source.
- Optically pumped edge-emitting GeSn lasers were achieved from thick bulk GeSn as active regions.
- GeSn lasers were achieved at different Sn compositions and GeSn thicknesses.
- The laser wavelength operation covered from 2 to 3 μm. The longest GeSn laser operation wavelength was 2987 nm at 180 K.
- The lowest lasing threshold value achieved, 45 kW/cm^2 at 10 K, was 30% lower than the previous lowest reported value, 68 kW/cm^2 [85].
- The highest temperature operation of GeSn laser was 180 K.
- The highest value of characteristic temperature was 103 K.

7.2 Future work

Achieving lasers from group IV semiconductors will require a lot of attention in developing these lasers. Optically pumped lasers from bulk GeSn are the first main step. There are several directions which need to be followed and are explained in the following suggestions.

7.2.1 Optimize the bulk GeSn lasers using DHS

There are many factors that impact the bulk GeSn lasers, such as the thickness of each layer and the composition of the active region. From experimental results of GeSn lasers, the samples that have structures with a Ge cap show better results due to the enhancement of carrier confinement. However, optimizing the thickness of Ge layer can improve the performance of

DHS of bulk GeSn lasers. The enhanced carrier confinement is the main factor in reducing lasing threshold and increasing the efficiency and output power of devices.

7.2.2 Study of doped GeSn lasers

From PL study, doping strongly impacts the PL intensity and shrinks the bandgap of GeSn. Therefore, the study of the doped GeSn lasers is attractive for several reasons. First, the lasing wavelength from doped GeSn is longer than that for undoped GeSn of the same Sn composition. Second, the temperature operation can be increased toward a room temperature.

7.2.3 Quantum Wells GeSn lasers

The QW structure is desirable for semiconductor lasers. There are many interesting characteristics for QWs to be used as the active region of lasers. First, QWs have better carrier confinement. Second, the lasing threshold of QW lasers is very low compared to the bulk structure. Third, it can operate at room temperature. Fourth, the linewidth of the laser is narrower due to the transition between the very defined quantized energy of levels in the well area. Several types of GeSn QW laser structures have been theoretically designed and investigated. These structures are designed to obtain Type-I band diagram direct bandgap GeSn to be used as an active region for lasers. Many groups have experimentally investigated both single and multi- QW GeSn with different types of barriers, such as GeSn, SiGeSn, or Ge. The barriers increase quantum confinement. However, the barrier should be designed with the exact composition of each element to be lattice matched between wells. The quantum well structures help with reducing lasing threshold and reaching to RT operation. Demonstrating QW GeSn lasers will be a great achievement for developing integrated photonic applications.

7.2.4 Electrically injected GeSn lasers

Obtaining electrically injected GeSn lasers is the final target for all previous achievements of GeSn lasers. Electrically injected lasers are more complicated due to the need for doping and building of NIP or PIN structures. Many NIP/PIN GeSn structures were investigated for LEDs applications [109]. However, no electrically injected GeSn laser has been demonstrated yet. There is a need for direct bandgap GeSn layers with enough doping concentration for n- and p-type doping. However, recent achievement of optically pumped GeSn for bulk and micro-disk will lead toward to demonstrating the first electrically injected GeSn laser.

References

[1] R. Soref, “Applications of silicon-based optoelectronics,” *MRS Bull.*, vol. 23, no. 4, pp. 20–24, 1998.

[2] R. A. Soref, “The Impact of Silicon Photonics,” *IEICE Trans. Electron*. E91-C, 129–130, 2008.

[3] R. A. Soref, S. J. Emelett, and W. R. Buchwald, “Silicon waveguide components for the long-wave infrared region,” *J. Opt. A: Pure Appl*. Opt. 8, 840–848, 2006.

[4] H. Rong, A. Liu, R. Jones, O. Cohen, D. Hak, R. Nicolaescu, A. Fang, and M. Paniccia, “A continuous-wave Raman silicon laser,” *Nature* 433, 292–294, 2005.

[5] J. Liu, X. Sun, R. Camacho-Aguilera, L. C. Kimerling, and J. Michel, “Ge-on-Si laser operating at room temperature,” *Opt. Lett*. 35, 679–681, 2010.

[6] R. E. Camacho-Aguilera, Y. Cai, N. Patel, J. T. Bessette, M. Romagnoli,L. C. Kimerling, and J. Michel, “An electrically pumped germanium laser,” *Opt. Express* 20, 11316–11320, 2012.

[7] W. Hu, B. Cheng, C. Xue, H. Xue, S. Su, A. Bai, L. Luo, Y. Yu, and Q. Wang, “Electroluminescence from Ge on Si substrate at room temperature,” *Appl. Phys. Lett*. 95, 092102, 2009.

[8] S.-L. Cheng, J. Lu, G. Shambat, H.-Y. Yu, K. Saraswat, J. Vuckovic, and Y. Nishi, “Room temperature 1.6 μm electroluminescence from Ge light emitting diode on Si substrate,” *Opt. Express* 17, 10019–10024, 2009.

[9] A. W. Fang, H. Park, O. Cohen, R. Jones, M. J. Paniccia, and J. E.Bowers, “Electrically pumped hybrid AlGaInAs-silicon evanescent laser,” *Opt. Express* 14, 9203–9210, 2006.

[10] H. Liu, T. Wang, Q. Jiang, R. Hogg, F. Tutu, F. Pozzi, and A. Seeds, ““Long-wavelength InAs/GaAs quantum dot laser diode monolithically grown on Ge substrate,” *Nat. Photonics* 5, 416–419, 2011.

[11] H. Yang, D. Zhao, S. Chuwongin, J.-H. Seo, W. Yang, Y. Shuai, J. Berggren, M. Hammar, Z. Ma, and W. Zhou, “Transfer-printed stacked nanomembrane lasers on silicon,” *Nat. Photonics* 6, 617–622, 2012.

[12] Z. Wang, B. Tian, M. Pantouvaki, W. Guo, P. Absil, J. Campenhout, C. Merckling, and D. Thourhout, “Room-temperature InP distributed feedback laser array directly grown on silicon,” *Nat. Photonics* 9, 837–842, 2015.

[13] S. Chen, W. Li, J. Wu, Q. Jiang, M. Tang, S. Shutts, S. N. Elliott, A. Sobiesierski, A. J. Seeds, I. Ross, P. M. Smowton, and H. Liu, “Electrically pumped continuous-wave III–V quantum dot lasers on silicon,” *Nat. Photonics* 10, 307–311, 2016.

[14] R.A. Soref and L. Friedman, “Direct-gap Ge/GeSn/Si and GeSn/Ge/Si heterostructures,” *Superlattices Microstruct*. 14,189, 1993.

[15] S. A. Ghetmiri, W. Du, J. Margetis, A. Mosleh, L. Cousar, B. R. Conley, L. Domulevicz, A. Nazzal, G. Sun, R. A. Soref, J. Tolle, B. Li, H. A. Naseem, S. -Q. Yu, “Direct-bandgap GeSn grown on silicon with 2230 nm photoluminescence,” *Appl. Phys. Lett*., vol. 105, no. 15, p. 151109, 2014.

[16] S. Al-Kabi, S. A. Ghetmiri, J. Margetis, W. Du, A. Mosleh, M. Alher, W. Dou, J. M. Grant, G. Sun, R. A. Soref, J. Tolle, B. Li, M. Mortazavi, H. A. Naseem, and S.-Q. Yu, “Optical Characterization of Si-Based Ge1_xSnx Alloys with Sn Compositions up to 12%,” *J. Electron. Mater*. 45, 2133, 2016.

[17] G. He and H.A. Atwater, “Interband Transitions in SnxGe12x Alloys,” *Phys. Rev. Lett*. 79, 1937, 1997.

[18] R. Ragan and H.A. Atwater, “Measurement of the direct energy gap of coherently strained $Ge_{1-x}Sn_x$/Ge (001) heterostructure,” *Appl. Phys. Lett*. 77, 3418, 2000.

[19] K. Alberi, J. Blacksberg, L. Bell, S. Nikzad, K. Yu, O. Dubon, and W. Walukiewicz, **“**Band anticrossing in highly mismatched SnxGe1−x semiconducting alloys,’ *Phys. Rev. B* 77, 073202, 2008.

[20] M. Bauer, J. Taraci, J. Tolle, A. V. G. Chizmeshya, S. Zollner, D. J. Smith, J. Menendez, C. Hu, and J. Kouvetakis, “Ge–Sn semiconductors for band-gap and lattice engineering,” *Appl. Phys. Lett.*, vol. 81, no. 16, pp. 2992–2994, 2002.

[21] S. Wirths, R. Geiger, N. Von Den Driesch, G. Mussler, T. Stoica, S. Mantl, Z. Ikonic, M. Luysberg, S. Chiussi, J. M. Hartmann, H. Sigg, J. Faist, D. Buca, D. Grutzmacher, “Lasing in direct-bandgap GeSn alloy grown on Si,” *Nat. Photonics*, vol. 9, no. 2, pp. 88–92, 2015.

[22] L. Jiang, C. Xu, J.D. Gallagher, R. Favaro, T. Aoki, J. Mene´ndez, and J. Kouvetakis, “Development of light emitting group IV ternary alloys on Si platforms for long wavelength optoelectronic applications,” *Chem. Mater.* 26, 2522, 2014.

[23] S. Zaima, O. Nakatsuka, N. Taoka, M. Kurosawa, W. Takeuchi, and M. Sakashita, “Growth and applications of GeSn-related group-IV semiconductor materials,” *Sci. Tech. Adv. Mater.* 16, 043502, 2015.

[24] B. R. Conley, J. Margetis, W. Du, H. Tran, A. Mosleh, S. A. Ghetmiri, J. Tolle, G. Sun, R. Soref, B. Li, H. A. Naseem, and S.-Q. Yu, “Si-based GeSn photoconductors with a 1.63 A/W peak responsivity and a 2.4 µm long-wavelength cutoff”, *Appl. Phys. Lett*., 105, 221117, 2014.

[25] J. Werner, M. Oehme, M. Schmid, M. Kaschel, A. Schirmer, E. Kasper, and J. Schulze, "Germanium-Tin p-i-n photodetectors integrated on Silicon grown by molecular beam epitaxy," *Appl. Phys. Lett*. 98, 061108, 2011.

[26] S. Kim, J. Gupta, N. Bhargava, M. Coppinger, and J. Kolodzey, "Current–Voltage Characteristics of GeSn/Ge Heterojunction Diodes Grown by Molecular Beam Epitaxy," *Electron Device Lett. IEEE* 34, 1217, 2013.

[27] Werner, M. Oehme, A. Schirmer, E. Kasper, and J. Schulze, "Molecular beam epitaxy grown GeSn p-i-n photodetectors integrated on Si," *Thin Solid Films* 520, 3361, 2012.

[28] J. Kouvetakis, J. Menendez, and R. A. Soref, "Strain-engineered direct-gap Ge/Sn_xGe_{1-x} heterodiode and multi-quantum-well photodetectors, laser, emitters and modulators grown on $Sn_ySi_zGe_{1-y-z}$ buffered silicon," U.S. Patent 6897471 B1 issued May 24, 2005.

[29] T. Pham, W. Du, H. Tran, J. Margetis, J. Tolle, G. Sun, R. A. Soref, H. A. Naseem, B. Li, and S.-Q. Yu, "Systematic study of Si-based GeSn photodiodes with 2.6 µm detector cutoff for short-wave infrared detection," *Opt. Express*, vol. 24, no. 5, pp. 4519–4531, 2016.

[30] B. R. Conley, J. Margetis, W. Du, H. Tran, A. Mosleh, S. A. Ghetmiri, J. Tolle, G. Sun, R. Soref, B. Li, H. A. Naseem, S.-Q. Yu, "Si based GeSn photoconductors with a 1.63 A/W peak responsivity and a 2.4 µm long-wavelength cutoff," *Appl. Phys. Lett*., vol. 105, no. 22, p. 221117, 2014.

[31] R.W. Hoogeveen and A.P. Goede, "Extended wavelength InGaAs infrared (1.0–2.4 µm) detector arrays on SCIAMACHY for space-based spectrometry of the Earth atmosphere," *Infrared Phys. Technol*. 42, 1, 2001.

[32] C. Grein, P. Young, M. Flatte´, and H. Ehrenreich, "Long wavelength InAs/InGaSb infrared detectors: Optimization of carrier lifetimes," *J. Appl. Phys*. 78, 7143, 1995.

[33] R. Geiger, T. Zabel and H. Sigg, "Group iv direct band gap photonics: methods, challenges, and opportunities," *Front. Mater.* 2, 52*,* 2015.

[34] J. Liu, "Monolithically integrated Ge-on-Si active photonics," in *Photonics*, 2014, vol. 1, pp. 162–197.

[35] J. Liu, X. Sun, R. Camacho-Aguilera, Y. Cai, L. C. Kimerling, and J. Michel, "Monolithic Ge-on-Si lasers for integrated photonics," *The 7th International Conference on Group IV Photonics (GFP),* 2010.

[36] G.-E. Chang, S.-W. Chang, and S. L. Chuang, "Theory for n-type doped, tensile-strained Ge–$Si_xGe_ySn_{1-x-y}$ quantum-well lasers at telecom wavelength," *Opt. Express*, 17, 14, 2009.

[37] L. T. Canham, "Silicon quantum wire array fabrication by electrochemical and chemical dissolution of wafers," Appl. Phys. Lett. 57, 1046–1048, 1990.

[38] H. Ennen, J. Schneider, G. Pomrenke, and A. Axmann, "1.54-μm luminescence of erbium-implanted III-V semiconductors and silicon," Appl. Phys. Lett. 43, 943-945, 1983.

[39] O. Boyraz and B. Jalali, "Demonstration of a silicon Raman laser," *Opt. Express* 12, 5269–5273, 2004.

[40] H. Rong, A. Liu, R. Jones, O. Cohen, D. Hak, R. Nicolaescu, A. Fang, and M. Paniccia, "An all-silicon Raman laser," *Nature* 433, 292–294, 2005.

[41] H. Rong, R. Jones, A. Liu, O. Cohen, D. Hak, A. Fang and M. Paniccia, "A continuous-wave Raman silicon laser," *Nature*, 433, 725-728, 2005.

[42] G. Levaufre, A. Le Liepvre, C. Jany, A. Accard, P. Kaspar, R. Brenot, D. Make, F. Lelarge, G-.H. Duan, S. Olivier, S. Malhouitre, C. Kopp, G. Simon, F. Saliou, P. Chanclou, "Hybrid III-V/silicon tunable laser directly modulated at 10Gbit/s for short reach/access networks", *Optical Communication (ECOC) 2014 European Conference on*, pp. 1-3, 2014.

[43] C. Pang, H. Benisty, M. Besbes, X. Pommarede, A. Talneau, "Oxide-free InP-on-Silicon-on-Insulator Nanopatterned Waveguides: Propagation Losses Assessment Through End-Fire and Internal Probe Measurements", *Lightwave Technology Journal of,* vol. 32, pp. 1048-1053, 2014.

[44] S. Lin, X. Zheng, J. Yao, S. Djordjevic, J. Cunningham, J. Lee, I. Shubin, Y. Luo, J. Bovington, D. Lee, H. Thacker, K. Raj, and A. Krishnamoorthy, "Efficient, tunable flip-chip-integrated III-V/Si hybrid external-cavity laser array," *Opt. Express,* 24, 21454-21462, 2016.

[45] J. Liu, X. Sun, R. Camacho-Aguilera, Y. Cai, J. Michel, and L. C. Kimerling, "Band-engineered Ge-on-Si lasers," in *Electron Devices Meeting (IEDM), 2010 IEEE International*, 2010.

[46] R. Camacho-Aguilera, Y. Cai, N. Patel, J. Bessette, M. Romagnoli, L. Kimerling, and J. Michel, "An electrically pumped germanium laser," *Opt. Express* 20, 11316-11320, 2012.

[47] D. Peschka, M. Thomas, A. Glitzky, R. Nürnberg, K. Gärtner, M. Virgilio, S. Guha, Th. Schroeder, G. Capellini, Th. Koprucki, "Modeling of Edge-Emitting Lasers Based on Tensile Strained Germanium Microstrips", *Photonics Journal IEEE*, vol. 7, pp. 1-15, 2015.

[48] D. Nam, D. Sukhdeo, J. Kang, M. Brongersma, K. Saraswat, "A nanomembrane-based bandgap-tunable Ge microdisk for Si-compatible optoelectronics", *Lasers and Electro-Optics Pacific Rim (CLEO-PR) 2015 11th Conference on*, vol. 1, pp. 1-2, 2015.

[49] J. Liu, X. Sun, D. Pan, X. Wang, L. Kimerling, T. Koch, and J. Michel, "Tensile-strained, n-type Ge as a gain medium for monolithic laser integration on Si," Opt. Express 15, 11272-11277, 2007.

[50] R. Koerner, M. Oehme, M. Gollhofer, M. Schmid, K. Kostecki, S. Bechler, D. Widmann, E. Kasper, and J. Schulze, “Electrically pumped lasing from Ge Fabry–Pérot resonators on Si,” *Opt. Exp*., vol. 23, no. 11, pp. 14815, 2015.

[51] M. Prost, M. El Kurdi, A. Ghrib, S. Sauvage, F. P. Aniel, N. Zerounian, I. Sagnes, G. Beaudoin, F. Boeuf, C. Baudot, and P. Boucaud, “Optimized design of an electrically pumped germanium laser,” *presented at the SPIE, San Diego, CA, USA*, 2014.

[52] B. Dutt, D. S. Sukhdeo, D. Nam, B. M. Vulovic, Z. Yuan, and K. C. Saraswat, “Roadmap to an efficient germanium-on-silicon laser: Strain vs. n-type doping,” *IEEE Photon. J.,* 4, 5, 2012.

[53] R. A. Soref and L. Friedman, “Direct gap Ge/GeSn/Si and GeSn/Ge/Si heterostructures”, Superlattice. Microst. 14, 18,1993.

[54] Na. Amrane, S.Ait. Abderahamen, H. Aourag, “Band structure calculation of GeSn and SiSn,” *Infrared Phys. Technol*., 36, 834, 1995.

[55] A. Zaoui, M. Ferhat, M. Certier, B. Khelifa, H. Aourag, “Optical properties of SiSn and GeSn,” *Infrared Phys. Technol*., 37, 4, 1996.

[56] J. Mathews, R.T. Beeler, J. Tolle, C. Xu, R. Roucka, J. Kouvetakis, and J. Mene´ndez, “Direct-gap photoluminescence with tunable emission wavelength in Ge1-ySny alloys on silicon,” *Appl. Phys. Lett* 97, 221912, 2010.

[57] M. Ryu, T.R. Harris, Y.K. Yeo, R.T. Beeler, and J. Kouvetakis, “Temperature-dependent photoluminescence of Ge/Si and $Ge_{1-y}Sn_y$/Si, indicating possible indirect-to-direct bandgap transition at lower Sn content,” Appl. Phys. Lett. 102, 171908, 2013,” *Appl. Phys. Lett*. 102, 171908, 2013.

[58] R. Chen, H. Lin, Y. Huo, C. Hitzman, T.I. Kamins, and J.S. Harris, “Increased photoluminescence of strain-reduced, high-Sn composition Ge1−xSnx alloys grown by molecular beam epitaxy,” Appl. Phys. Lett. 99, 181125, 2011,” *Appl. Phys. Lett*. 99, 181125, 2011.

[59] L. Jiang, J.D. Gallagher, C.L. Senaratne, T. Aoki, J. Mathews, J. Kouvetakis, and J. Mene´ndez, “Compositional dependence of the direct and indirect band gaps in Ge1-ySny alloys from room temperature photoluminescence: implications for the indirect to direct gap crossover in intrinsic and n-type materials,” *Semicond. Sci.Tech*. 29, 115028, 2014.

[60] M. Oehme, M. Schmid, M. Kaschel, M. Gollhofer, D. Widmann, E. Kasper, and J. Schulze, “GeSn pin detectors integrated on Si with up to 4% Sn,” *Appl. Phys. Lett*. 101, 141110, 2012.

[61] A. Gassenq, F. Gencarelli, J. Van Campenhout, Y. Shimura, R. Loo, G. Narcy, B. Vincent, and G. Roelkens, “GeSn/Ge heterostructure short-wave infrared photodetectors on silicon,” O*pt. Express* 20, 27297, 2012.

[62] S. Su, B. Cheng, C. Xue, W. Wang, Q. Cao, H. Xue, W. Hu, G. Zhang, Y. Zuo, and Q. Wang, "GeSn pin photodetector for all telecommunication bands detection," O*pt. Express* 19, 6400, 2011.

[63] H.H. Tseng, H. Li, V. Mashanov, Y.J. Yang, H.H. Cheng, G.E. Chang, R.A. Soref, and G. Sun, "GeSn-based pin photodiodes with strained active layer on a Si wafer," *Appl. Phys. Lett*. 103, 231907, 2013.

[64] D. Zhang, C. Xue, B. Cheng, S. Su, Z. Liu, X. Zhang, G. Zhang, C. Li, and Q. Wang, "High-responsivity GeSn short-wave infrared pin photodetectors," *Appl. Phys. Lett*. 102, 141111, 2013.

[65] M. Oehme, K. Kostecki, K. Ye, S. Bechler, K. Ulbricht, M. Schmid, M. Kaschel, M. Gollhofer, R. Ko¨rner, W. Zhang, E. Kasper, and J. Schulze, "GeSn-on-Si normal incidence photodetectors with bandwidths more than 40 GHz," *Opt. Express* 22, 839, 2014.

[66] B.R. Conley, A. Mosleh, S.A. Ghetmiri, W. Du, R.A. Soref, G. Sun, J. Margetis, J. Tolle, H.A. Naseem, and S. Yu, "Temperature dependent spectral response and detectivity of GeSn photoconductors on silicon for short wave infrared detection," *Opt. Express* 22, 15639, 2014.

[67] T.N. Pham, W. Du, B.R. Conley, J. Margetis, G. Sun, R.A.Soref, J. Tolle, B. Li, and S.-Q. Yu, "Si-based Ge0. 9Sn0. 1 photodetector with peak responsivity of 2.85 A/W and longwave cutoff at 2.4 µm," *Electron. Lett*. 51, 854, 2015.

[68] C. Vedatrayee, B. Mukhapadhyay, and P.K. Basu, "Performance prediction of an electroabsorption modulator at 1550nm using GeSn/SiGeSn Quantum Well structure," *Physica E* 50, 67, 2013.

[69] R.A. Soref, G. Sun, and H.H. Cheng, "Franz-Keldysh electro-absorption modulation in germanium-tin alloys," *J. Appl. Phys*. 111, 123113, 2012.

[70] M. Oehme, J. Werner, M. Gollhofer, M. Schmid, M. Kasche, and E. Kasper, "Room-temperature electroluminescence from GeSn light-emitting pin diodes on Si," *IEEE Photon. Technol. Lett.* 23, 1751, 2011.

[71] R. Roucka, J. Mathews, R.T. Beeler, J. Tolle, J. Kouvetakis, and J. Mene´ndez, "Direct gap electroluminescence from Si/Ge_{1-y} Sn_y p-in heterostructure diodes," *Appl. Phys. Lett.* 98, 061109, 2011.

[72] J.P. Gupta, N. Bhargava, S. Kim, T. Adam, and J. Kolodzey, "Infrared electroluminescence from GeSn heterojunction diodes grown by molecular beam epitaxy,' *Appl. Phys. Lett*. 102, 251117, 2013.

[73] H.H. Tseng, K.Y. Wu, H. Li, V. Mashanov, H.H. Cheng, G. Sun, and R.A. Soref, "Mid-infrared electroluminescence from a Ge/$Ge_{0.922}Sn_{0.078}$/Ge double heterostructure pin diode on a Si substrate," *Appl. Phys. Lett*. 102, 182106, 2013.

[74] W. Du, Y. Zhou, S.A. Ghetmiri, A. Mosleh, B.R. Conley, A. Nazzal, R.A. Soref, G. Sun, J. Tolle, J. Margetis, H.A. Naseem, and S. Yu, “Room-temperature electroluminescence from Ge/$Ge_{1-x}Sn_x$/Ge diodes on Si substrates,” *Appl. Phys. Lett*. 104, 241110, 2014.

[75] E. Kasper and M. Oehme, “Germanium tin light emitters on silicon,” Jpn. *J. Appl. Phys*. 54, 04DG1, 2015.

[76] J.D. Gallagher, C.L. Senaratne, P. Sims, T. Aoki, J. Menendez, and J. Kouvetakis, “Electroluminescence from GeSn heterostructure pin diodes at the indirect to direct transition,” *Appl. Phys. Lett.* 106, 091103, 2015.

[77] G. Sun, R. A. Soref, and H. H. Cheng, “Design of an electrically pumped SiGeSn/GeSn/SiGeSn double heterostructure mid-infrared laser,” J. Appl. Phys. 108(3), 033107, 2010.

[78] G. Sun, R. A. Soref, and H. H. Cheng, “Design of a Si-based lattice-matched room-temperature GeSn/GeSiSn multi-quantum-well mid-infrared laser diode,” *Opt. Express*, vol. 18, no. 19, pp. 19957–19965, 2010.

[79] G. Sun, and S.-Q. Yu, “The SiGeSn approach towards Si-based lasers,” *Solid-State Electron.,* 83, 76, 2013.

[80] G.-E. Chang, S.-W. Chang, and S. L. Chuang, “Strain-balanced multiple-quantum-well lasers,” *IEEE J. Quantum Electron.*, vol. 46, no. 12, pp. 1813–1820, 2010.

[81] Y.-H. Zhu, Q. Xu, W.-J. Fan, and J.-W. Wang, “Theoretical gain of strained $GeSn_{0.2}$/$Ge_{1-x-y}S_xSn_y$ quantum well laser,” *J. Appl. Phys*. 107(7), 073108, 2010.

[82] B. Dutt, H. Lin, D. S. Sukhdeo, B. M. Vulovic, S. Gupta, D. Nam, K. C. Saraswat, and J. S. Harris, “Theoretical analysis of GeSn alloys as a gain medium for a Si-compatible laser,” *IEEE J. Sel. Topics Quantum Electron*., 19, 5, 2013.

[83] K. P. Homewood and M. A. Lourenço, “Optoelectronics: The rise of the GeSn laser,” *Nature Photon*., 9, 2, 2015.

[84] D. Stange, S. Wirths, R. Geiger, C. Schulte-Braucks, B. Marzban, N. vonden Driesch, G. Mussler, T. Zabel, T. Stoica, J.-M. Hartmann, S. Mantl, Z. Ikonic, D. Grutzmacher, H. Sigg, J. Witzens, and D. Buca, “Optically Pumped GeSn Microdisk Lasers on Si,” *ACS Photonics*, 3, 1279, 2016.

[85] S. Al-Kabi, S. A. Ghetmiri, J. Margetis, T. Pham, Y. Zhou, B. Collier, R. Quinde, W. Du, A. Mosleh, J. Liu, G. Sun, R. A. Soref, J. Tolle, B. Li, M. Mortazavi, H. A. Naseem, and S.-Q. Yu, “An optically pumped 2.5 µm GeSn laser on Si operating at 110 K”, Appl. Phys. Lett., 109, 171105, 2016.

[86] W. T. Silfvast, “Laser fundamentals,” 2nd ed. Cambridge;New York;: Cambridge University Press. 1937. 2004. pp 576-579.

[87] S. L. Chuang, "Physics of photonic devices," *2nd ed. Hoboken, N.J: John Wiley & Sons*. 2009. pp. 414-423.

[88] W. W. Chow, and S. W. Koch. "Semiconductor-laser fundamentals: Physics of the gain materials," *New York;Berlin: Springer*. 1999. pp. 3-12.

[89] E. Kapon, "Semiconductor lasers," *San Diego: Academic Press,* 1999. pp. 3-7.

[90] J. Margetis, S. A. Ghetmiri, W. Du, B. R. Conley, A. Mosleh, R. Soref, G. Sun, L. Domulevicz, H. A. Naseem, S.-Q. Yu, J. Tolle, "Growth and characterization of epitaxial $Ge_{1-x}Sn_x$ alloys and heterostructures using a commercial CVD system," *ECS Trans.*, 64, 6, 711, 2014.

[91] J. Margetis, A. Mosleh, S. A. Ghetmiri, S. Al-Kabi, W. Dou, W. Du, N. Bhargava, S.-Q. Yu, H. Profijt, D. Kohen, R. Loo, A. Vohra, and J. Tolle, "Fundamentals of $Ge_{1-x}Sn_x$ and $Si_yGe_{1-xy}Sn_x$ RPCVD epitaxy," *Mater. Sci. Semicond. Process.* (2016), http://dx.doi.org/10.1016/j.mssp.2016.12.024

[92] J. Margetis, A. Mosleh, S. Al-Kabi, S.A. Ghetmiri, W. Du, W. Dou, M. Benamara, B. Li, M. Mortazavi, H.A. Naseem, S.-Q. Yu, and J. Tolle, "Study of low-defect and strain-relaxed GeSn growth via reduced pressure CVD in H_2 and N_2 carrier gas," *J. Cryst. Growth*, 463, 128, 2017.

[93] D. K. Schroder, "Semiconductor material and device characterization," *3rd ed. Piscataway, NJ;Hoboken, N.J;: IEEE Press*, 2006. pp. 604-609.

[94] S. Wirths, R. Geiger, Z. Ikonic, A.T. Tiedemann, G. Mussler, J.M. Hartmann, S. Mantl, H. Sigg, D. Grutzmacher, and D. Buca, "Epitaxy and photoluminescence studies of high quality GeSn heterostructures with Sn concentrations up to 13 at.%," in *IEEE International Conference on Group IV Photonics GFP. IEEE Computer Society*, 2014.

[95] G. Grzybowski, L. Jiang, J. Mathews, R. Roucka, C. Xu, R.T. Beeler, J. Kouvetakis, and J. Mene´ndez, "Photoluminescence from heavily doped GeSn: P materials grown on Si (100)," *Appl. Phys. Lett*. 99, 171910, 2011.

[96] W. Du, S.A. Ghetmiri, B.R. Conley, A. Mosleh, A. Nazzal, R.A. Soref, G. Sun, J. Tolle, J. Margetis, H.A. Naseem, and S. Yu, "Competition of optical transitions between direct and indirect bandgaps in $Ge_{1-x}Sn_x$," *Appl. Phys. Lett*. 105, 051104, 2014.

[97] T.R. Harris, Y.K. Yeo, M. Ryu, R.T. Beeler, and J. Kouvetakis, "Observation of heavy- and light-hole split direct bandgap photoluminescence from tensile-strained GeSn (0.03% Sn)," *J. Appl. Phys.* 116, 103502, 2014.

[98] R.T. Beeler, G.J. Grzybowski, R. Roucka, L. Jiang, J. Mathews, D.J. Smith, J. Menendez, A.V.G. Chizmeshya, and J. Kouvetakis, "Observation of heavy-and light-hole split direct bandgap photoluminescence from tensile-strained GeSn (0.03% Sn)," *J. Chem. Mater.* 23, 4480, 2011.

[99] R. Geiger, T. Zabel, and H. Sigg, "Group IV direct band gap photonics: methods, challenges, and opportunities," *Front Mater*. v.2, 2015. pp. 81-89.

[100] S. Gupta, B. Magyari-Köpe, Y. Nishi, and K. C. Saraswat, “Achieving direct band gap in germanium through integration of Sn alloying and external strain,” *J. Appl. Phys*., vol. 113, no. 7, p. 73707, 2013.

[101] V.R. D’Costa, J. Tolle, R. Roucka, C.D. Poweleit, J. Kouvetakis,and J. Mene´ndez, “Raman scattering in Ge 1− y Sn y alloys,’ *Solid State Commun*. 144, 240, 2007.

[102] S. Su, W. Wang, B. Cheng, W. Hu, G. Zhang, C. Xue, Y. Zuo, and Q. Wang, “The contributions of composition and strain to the phonon shift in alloys,” *Solid State Commun*. 151, 647, 2011.

[103] S. A. Ghetmiri, W. Du, B. R. Conley, A. Mosleh, A. Nazzal, G. Sun, R. A. Soref, J. Margetis, J. Tolle, H. A. Naseem, S. -Q. Yu, “Shortwave-infrared photoluminescence from Ge1- xSnx thin films on silicon,” *J. Vac. Sci. Technol. B*, vol. 32, no. 6, p. 60601, 2014.

[104] A. A. Tonkikh, C. Eisenschmidt, V.G. Talalaev, N.D. Zakharov, J. Schilling, G. Schmidt, and P. Werner, “Pseudomorphic GeSn/Ge (001) quantum wells: Examining indirect band gap bowing,” *Appl. Phys. Lett*. 103, 032106, 2013.

[105] S. Shevchenko and A. Tereshchenko, “Peculiarities of dislocation photoluminescence in germanium with quasi-equilibrium dislocation structure,” *Phys. Status Solidi* 4, 2898, 2007.

[106] S. Al-Kabi, S. A. Ghetmiri, J. Margetis, W. Du, A. Mosleh, W. Dou, G. Sun, R. A. Soref, J. Tolle, B. Li, M. Mortazavi, H. A. Naseem, and S.-Q. Yu. “Study of High-Quality GeSn Alloys Grown by Chemical Vapor Deposition towards Mid-Infrared Applications,” *J. Electron. Mater,* 45, 6251, 2016.

[107] A. Mosleh, S.A. Ghetmiri, B.R. Conley, M. Hawkridge, M. Benamara, A. Nazzal, J. Tolle, S. Yu, and H.A. Naseem, “Material characterization of Ge1-xSnx alloys using a commercial CVD system for Optoelectronic Device Applications,” *J. Electron. Mater.* 43, 938, 2014.

[108] H. Tran, W. Du, S. A. Ghetmiri, A. Mosleh, G. Sun, R. A. Soref, J. Margetis, J. Tolle, B. Li, H. A. Naseem, S. -Q. Yu, “Systematic study of Ge1- xSnx absorption coefficient and refractive index for the device applications of Si-based optoelectronics,” *J. Appl. Phys*., 119, 10, 103106, 2016.

[109] Y. Zhou, W. Dou, W. Du, T. Pham, S. A. Ghetmiri, S. Al-Kabi, A. Mosleh, M. Alher, J. Margetis, J. Tolle, G. Sun, R. Soref, B. Li, M.Mortazavi, H. Naseem, and S.-Q. Yu, “Systematic study of GeSn heterostructure-based light-emitting diodes towards mid-infrared applications,” *J. Appl. Phys.* 120, 023102, 2016.

[110] R. Soref, D. Buca, and S.-Q. Yu, “Group IV Photonics: Driving Integrated Optoelectronics,” *Opt. Photonics News,* 27, 32, 2016.

[111] V. R. D'Costa, C. S. Cook, A. G. Birdwell, C. L. Littler, M. Canonico, S. Zollner, J. Kouvetakis, and J. Menendez, "Optical critical points of thin-film $Ge_{1-y}Sn_y$ alloys: A comparative $Ge_{1-y}Sn_y/Ge_{1-x}Si_x$ study," *Phys. Rev. B* 73, 125207, 2006.

[112] S. Al-Kabi, S. A. Ghetmiri, J. Margetis, T. Pham, Y. Zhou, W. Du, A. Mosleh, J. Liu, G. Sun, R. A. Soref, J. Tolle, B. Li, M. Mortazavi, H. A. Naseem, and S.-Q. Yu, "Optically pumped Si-based edge-emitting GeSn laser", *CLEO: Science and Innovations, 2017*.

[113] H. Li, X. Wang, and J. Liu, "Highly effective strain-induced band-engineering of (111) oriented, direct-gap GeSn crystallized on amorphous SiO2 layers," *Appl. Phys. Lett*. 108, 102101, 2016.

[114] J. M. Khosrofian and B. A. Garetz, "Measurement of a Gaussian laser beam diameter through the direct inversion of knife-edge data," *Appl. Opt*. 22, 3406, 1983.

[115] M. A.C. de Araújo, R. Silva, E. de Lima, D. P. Pereira, and P. C. de Oliveira, "Measurement of Gaussian laser beam radius using the knife-edge technique: improvement on data analysis," *Appl. Opt*. 48, 393, 2009.

[116] H. C. Casey, Jr., "Temperature dependence of the threshold current density in

$InP\text{-}Ga_{0.28}In_{0.72}As_{0.6}P_{0.4}$ (λ= 1.3 μm) double heterostructure lasers," *J. Appl. Phys*. 56, 1959, 1984.

[117] R. C. Miller, R. Dingle, A. C. Gossard, R. A. Logan, W. A. Nordland, Jr., and W. Wiegmann, "Laser oscillation with optically pumped very thin $GaAs\text{-}Al_xGa_{1-x}As$ multilayer structures and conventional double heterostructures," *J. Appl. Phys*. 47, 4509, 1976.

[118] M. Jaros, "Simple analytic model for heterojunction band offsets," *Phys. Rev. B, Condens. Matter*. 37, 7112, 1988.

[119] D. Buca, *IEEE Summer Topicals Meeting 2016, Newport Beach,* CA, July 11-13 (2016).

[120] H. Tran, W. Du and S. -Q. Yu, *manuscript in preparation, 2017.*

[121] D. Stange, N. Von Den Driesch, D. Rainko, C. Schulte-Braucks, S. Wirths, G. Mussler, A. T. Tiedemann, T. Stoica, J. M. Hartmann, Z. Ikonic, S. Mantl, D. Grutzmacher, D. Buca, "Study of GeSn based heterostructures: towards optimized group IV MQW LEDs," *Opt. Exp*. 24, 1358, 2016.

[122] K. Tanabe, K. Watanabe, & Y. Arakawa, " III–V/Si hybrid photonic devices by direct fusion bonding." Sci. Rep. 2, 349, 2012.

[123] T. J. Kippenberg, J. Kalkman, A. Polman, & K. J. Vahala, "Demonstration of an erbium-doped microdisk laser on a silicon chip," *Phys. Rev. A* **74**, 051802, 2006.

[124] A. Fallahkhair, K. S. Li, and T. E. Murphy, "Vector Finite Difference Modesolver for Anisotropic Dielectric Waveguides," *J. Lightwave Technol.* **26**, 1423, 2008.

Appendix A. Knife-Edge Method to Calculate the Gaussian Beam Size of Laser

The power density was calculated based on the knife-edge technique that is detailed in the Refs. 1 and 2. In order to calculate the power density, two parameters need to be determined: 1) the peak power of the pumping laser, and 2) the effective laser spot area that was homogenously shined on the waveguide device. The peak power was calculated by dividing the average power (read by power meter) over the duty cycle (2.7 × 10-4 s) of the pumping laser. The following method was used to calculate the effective laser spot area: the focused laser beam after the cylindrical lens has a rectangular shape. The well-known knife-edge technique was exploited to realize the focused laser beam uniformity profile. The transmitted laser power was measured while sliding a micrometer-mounted sharp-edge blade through the focused beam. Thus, the laser spot area that has a uniform distribution of the power was measured. Based on the measurement, the area was calculated as 6×10^{-4} cm^2.

References

[1] J. M. Khosrofian and B. A. Garetz, “Measurement of a Gaussian laser beam diameter through the direct inversion of knife-edge data,” Appl. Opt. 22, 3406, 1983.

[2] M. A.C. de Araújo, R. Silva, E. de Lima, D. P. Pereira, and P. C. de Oliveira, “Measurement of Gaussian laser beam radius using the knife-edge technique: improvement on data analysis,” Appl. Opt. 48, 393, 2009.

Appendix B: Description of Research for Popular Publication.

Si-based technology has been developed very fast in the last few decades. It is involved in numerous fields in the semiconductor industry. Integrated optoelectronic and photonics is one of the most important areas due to the reduction of size in a lot of applications. The main challenge is to integrate many optoelectronic components on a chip and still be compatible with CMOS processing Emitting devices such as LEDs and lasers are strongly needed in integrated photonics. Group IV elements, that are compatible structures to Si, have low efficiency for light emitting applications due to the nature of the indirectness of their bandgaps. Several approaches have been taken to make lasers from group IV materials such Si-Raman lasers, and heavy doped Ge lasers. However, there were many weaknesses such as low efficiency, high cost for doping, and high input power due to the high losses for these lasers. Even though III-V lasers are good light sources, integrating them on Si substrates requires different integration approaches such as wafer-bonding or direct growth and are still expensive.

In the last few years, it was theoretically proven that GeSn could be a direct bandgap material with Sn composition of 6 to 10%. After that, it was experimentally reported. Achieving direct bandgap material from group IV opens new interesting opportunities for integrated photonics for different reasons: (1) compatible with CMOS process; (2) monolithically grown on Si; (3) low cost; and, (4) covers a wide range of wavelengths in short and mid-infrared due to tunability of GeSn with change of the Sn composition.

Optically pumped edge-emitting lasers were demonstrated by Sattar Al-Kabi who is a Ph.D. candidate in the Microelectronics-Photonics graduate program at the University of Arkansas. The GeSn lasers cover 2 to 3 μm wavelength with the highest temperature operation, 180 K, and lowest lasing threshold, 45 kW/cm^2. This superior laser performance can lead

forward into electrically injected GeSn for room temperature operation. There are several groups around the world who work on SiGeSn/GeSn, however, the University of Arkansas group is one of the main leaders in this area. A direct bandgap GeSn was experimentally proven by Dr. Yu's group. Dr. Shui-Qing (Fisher) Yu, Professor of Electrical Engineering, has led the group for many breakthrough achievements. Tens of peer-reviewed papers have been published in scientific journals and conferences that show the impact of this group in the GeSn/SiGeSn field.

Appendix C: Executive Summary of Newly Created Intellectual Property

1- Demonstrated GeSn lasers covering 2 to 3 μm of wavelengths with the lowest lasing threshold and highest temperature operation using high quality GeSn grown with several Sn compositions up to 17.5 %.

2- Integrated many laser sources for photoluminescence and optical pumping setups measurements with an easy method to switch between laser sources and cryostats.

Appendix D: Potential Patent and Commercialization Aspects of Listed Intellectual Property Items

D.1 Patentability of Intellectual Property (Could Each Item be Patented)

1. ASM company is the owner of the intellectual property for the growth of high-quality GeSn.
2. The integration of many lasers and optics setup for PL and optical pumping measurements could not be patented since it would be obvious to researchers skilled in this field.

D.2 Commercialization Prospects (Should Each Item Be Patented)

1. ASM has a patent of the high-quality GeSn growth techniques. (#US20170154770 A1).
2. Not applicable

D.3 Possible Prior Disclosure of IP

1. The results of a demonstration of the optically pumped GeSn lasers were publicly disclosed in a journal article (Applied Physics Letters 109, 171105, (2016)). Furthermore, other optically pumped GeSn lasers results that cover 2 to 3 µm of wavelength and with high Sn composition up 17.5% are under submission to Nature Photonics (2017).
2. Not applicable

Appendix E: Broader Impact of Research

E.1. Applicability of Research Methods to Other Problems

Achieving optically pumped edge-emitting GeSn lasers results in this dissertation led to developing GeSn lasers with different structures, such as DHS and QWs for optically and electrically injected lasers. Moreover, it can be applied to achieving optically pumped SiGeSn lasers for short infrared applications.

E.2. Impact of Research Results on U.S. and Global Society

Monolithically and direct bandgap lasers from group IV is an interesting achievement to provide new methods for integrated photonics. Normally, GeSn is a cheap material which enables development for future laser applications in short and mid-infrared range. The number of research groups investigating SiGeSn/GeSn has increased in the last few years due to the importance of this area. Optimization of the GeSn lasers and achieving RT lasing operation of this material will make a big change in the industry for laser applications due to the low cost and wide range that can be covered using GeSn lasers.

E.3. Impact of Research Results on the Environment

The GeSn lasers with 2 to 3 μm range are very important for sensing applications. The absorption of many gases, such as CO, CO_2, C_2H_2, and CH_4 is located at wavelengths between 2 to 3.4 μm. This range can be covered with GeSn lasers, so can be used as sensing for these gases. Making cheap GeSn lasers for sensing these gases can help in controlling emission of the gases into the environment.

Appendix F: Microsoft Project for Ph.D. MicroEP Degree Plan

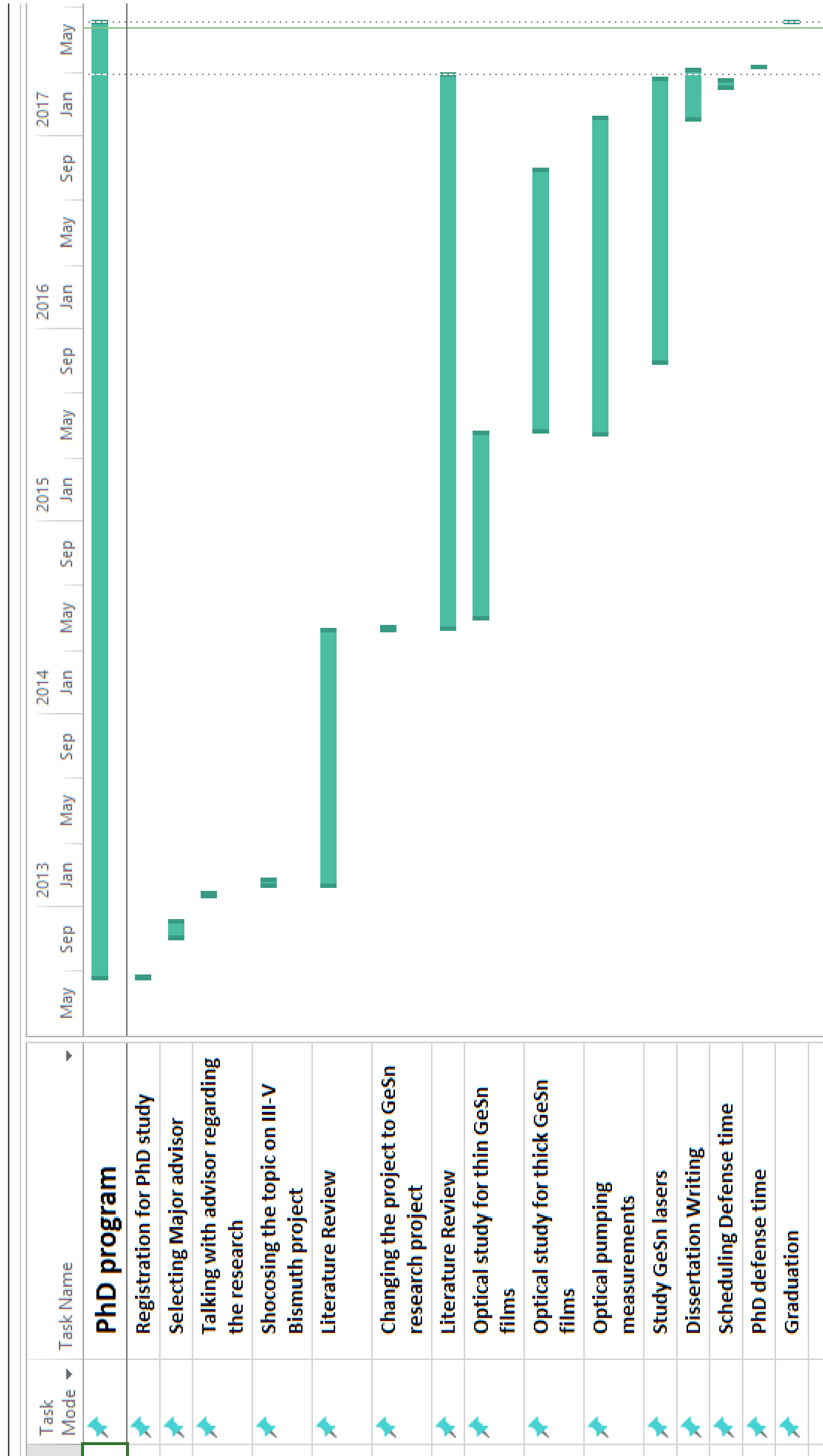

Appendix H: Identification of All Software Used in Research and Dissertation Generation

Computer #1:
    Model Number: Sony
    Serial Number: SVS131190X
    Location: Personal Laptop
    Owner: Sattar Al-Kabi
Software #1:
    Name: Microsoft Office 2016
    Purchased by: Electrical Engineering Department, University of Arkansas
Software #2:
    Name: Microsoft Project 2016
    Provided by: Microelectronics-Photonics, University of Arkansas
Software #3:
    Name: Matlab R2016a Student Version
    Provided by: University of Arkansas
Software #4:
    Name: Origin Lab
    Serial Number (2013-2014): GA3S4-6089-7208492
    Serial Number (2015): GA3S4-6089-7210853
    Serial Number (2016): GA3S4-6089-7211957
    Serial Number (2017): GA3S4-6089-7218359
    Purchased by: Sattar Al-Kabi
Software #5:
    Name: 1D and 2D TEM Solver
    Provided by: Free online link available
Computer #2:
    Model Number: Dell Inspiron
    Serial Number: 52M6XK1
    Location: ENRC Room 2923
    Owner: Dr. Shui-Qing Yu
Software #1:
    Name: SynerJY with built-in Origin software
    Purchased by: Dr. Shui-Qing Yu
Software #2:
    Name: LabVIEW 2016
    Purchased by: Electrical Engineering Department, University of Arkansas
Computer #3:
    Model Number: Dell Vostro
    Serial Number: 52M6XK1
    Location: ENRC Room 2923
    Owner: Dr. Shui-Qing Yu
Software #1:
    Name: SynerJY with built-in Origin software
    Purchased by: Dr. Shui-Qing Yu
Software #2:

Name: LabVIEW 2016
Purchased by: Electrical Engineering Department, University of Arkansas

Appendix I: All Publications Published, Submitted and Planned

I.1 List of Peer-Reviewed Published Works

13 J. Margetis, A. Mosleh, **S. Al-Kabi**, S.A. Ghetmiri, W. Du, W. Dou, M. Benamara, B. Li, M. Mortazavi, H.A. Naseem, S.-Q. Yu, J. Tolle, “Study of low-defect and strain-relaxed GeSn growth via reduced pressure CVD in H_2 and N_2 carrier gas,” *J of Cryst. Growth*, 463, 128–133, (2017).

12 J. Margetis, A. Mosleh, S. A. Ghetmiri, **S. Al-Kabi**, W. Dou, W. Du, N. Bhargava, S-Q. Yu, H. Profijt, D. Kohen, R. Loo, A. Vohra, e, J. Tolle, “Fundamentals of $Ge_{1-x}Sn_x$ and $Si_yGe_{1-x-y}Sn_x$ RPCVD epitaxy,” *Mater. Sci. Semicond. Process.* (2016). oi.org/10.1016/j.mssp.2016.12.024

11 S. A. Ghetmiri, Y. Zhou, J. Margetis, S. **Al-Kabi,** W. Dou, A. Mosleh, W. Du, A. Kuchuk, J. Liu, G. Sun, R. A. Soref, J. Tolle, H. A. Naseem, B. Li, M. Mortazavi, and S.-Q. Yu, “Study of SiGeSn/GeSn/SiGeSn quantum well structures towards Si-based infrared emitters,” *Optics Lett. 42, Issue 3, pp. 387-390 (2017).*

10 **S. Al-Kabi**, S. A. Ghetmiri, J. Margetis, T. Pham, Y. Zhou, B. Collier, R. Quinde, W. Du, A. Mosleh, J. Liu, G. Sun, R. A. Soref, J. Tolle, B. Li, M. Mortazavi, H. A. Naseem, and S.-Q. Yu, “An optically pumped 2.5 μm GeSn laser on Si operating at 110 K”, *Appl. Phys. Lett.*, 109, 171105, (2016). *Highlighted in ScienceDaily website.*

9 W. Dou, S. A. Ghetmiri, **S. Al-Kabi**, A. Mosleh, W. Du, G. Sun, R. A. Soref, J. Margetis, J. Tolle, B. Li, M. Mortazavi, H. A. Naseem, S.-Q. Yu, “CVD Grown Pseudomorphic GeSn/GeSn and SiGeSn/GeSn Single Quantum Wells,” *J. Electron Mater*, (2016). doi:10.1007/s11664-016-5031-2

8 **S. Al-Kabi**, S. A. Ghetmiri, J. Margetis, A. Mosleh, W. Dou, W. Du, G. Sun, R. A. Soref, J. Tolle, B. Li, M. Mortazavi, H. A. Naseem, S.-Q. Yu, “High-Quality CVD Grown Thick GeSn Samples with Enhanced Photoluminescence Intensity,” *J. Electron Mater*, (2016). doi:10.1007/s11664-016-5028-x

7 W. Du, **S Al-Kabi**, S. A. Ghetmiri, H. Tran, T. Pham, B. Alharthi, A. Mosleh, J. Margetis, J. Tolle, H. A Naseem, M. Mortazavi, G. Sun, R. Soref, B Li, S.-Q. Yu, “Development of SiGeSn Technique Towards Mid-Infrared Devices in Silicon Photonics” *ECS Transactions*, 75, 231 (2016).

6 Y. Zhou, W. Dou, W. Du, T. Pham, S. A. Ghetmiri, **S. Al-Kabi**, A. Mosleh, M. Alher, J. Margetis, J. Tolle, G. Sun, R. A. Soref, B. Li, M. Mortazavi, H. A. Naseem, S. -Q. Yu, “Systematic study of GeSn heterostructure-based light-emitting diodes towards mid-infrared applications,” J. Appl. Phys. 120, (2), 023102 (2016).

5 A. Mosleh, M. Alher, W. Du, L. Cousar, S. A. Ghetmiri, **S. Al-Kabi**, W. Dou, P. C. Grant, G. Sun, R. A. Soref, B. Li, H. A. Naseem, S.-Q. Yu, “Buffer-free GeSn and

SiGeSn growth on Si substrate using in-situ SnD_4 gas mixing", *J. Electron. Mater. 45 (4), 2051* (2016).

4 A. Mosleh, M. Alher, W. Du, L. Cousar, S. A. Ghetmiri, **S. Al-Kabi**, W. Dou, P. C Grant, G. Sun, R. A. Soref, B. Li, H. A. Naseem, S. –Q. Yu, "$Si_yGe_{1-x-y}Sn_x$ films grown on Si using a cold-wall ultrahigh-vacuum chemical vapor deposition system", *J. Vac. Sci. Technol. B*, 34 (1), 011201 (2016). *Selected as one of the featured articles of the month.*

3 **S. Al-Kabi**, S. A. Ghetmiri, J. Margetis, W. Du, A. Mosleh, M. Alher, W. Dou, G. Sun, R. A. Soref, J. Tolle, B. Li, M. Mortazavi, H. A. Naseem, S.-Q. Yu, "Optical characterization of Si-based $Ge_{1-x}Sn_x$ alloys with Sn compositions up to 12%", *J. Electron. Mater.*, 45 (4) 2133 (2015). *Highlighted by editor-in-chief as one of the best articles.*

2 A. Mosleh, M. A Alher, L. Cousar, H. H. Abusafe, W. Dou, P. Grant, **S. Al-Kabi**, S. A. Ghetmiri, B. Alharthi, H. Tran, W. Du, M. Benamara, B. Li, M. Mortazavi, S.-Q. Yu, H. A Naseem, "Enhancement of Material Quality of (Si) GeSn Films Grown by $SnCl_4$ Precursor", *ECS Transactions*, 69 (5), 279 (2015).

1 M. Alher, A. Mosleh, L. Cousar, W. Dou, P. Grant, S. A. Ghetmiri, **S. Al-Kabi**, W. Du, M. Benamara, B. Li, M. Mortazavi, S.-Q. Yu, H. A Naseem, "CMOS Compatible Growth of High-Quality Ge, SiGe and SiGeSn for Photonic Device Applications", *ECS Transactions*, 69 (5), 269 (2015).

I. 2 List of Conference Proceedings and Publications

10 H. Alahmad, M. Alher, **S. Al-Kabi**, S. A. Ghetmiri, A. Mosleh, S.-Q. Yu, H. A. Naseem, "Growth and characterization of GePb Alloy using layer inversion method" *Accepted EMC*, (2017).

9 **S. Al-Kabi**, S. A. Ghetmiri, J. Margetis, T. Pham, Y. Zhou, W. Dou, W. Du, A. Mosleh, J. Liu, G. Sun, R. A. Soref, J. Tolle, B. Li, M. Mortazavi, H. A. Naseem, and S.-Q. Yu, "Optically pumped Si-based edge-emitting GeSn laser," *Accepted by CLEO*, (2017).

8 W. Du, S. A. Ghetmiri, **S. Al-Kabi**, J. Margetis, T. Pham, Y. Zhou, W. Dou, A. Mosleh, J. Liu, G. Sun, R. A. Soref, J. Tolle, B. Li, M. Mortazavi, H. A. Naseem, and S.-Q. Yu, "Study of SiGeSn/GeSn/SiGeSn Quantum Well towards All Group-IV-Optoelectronics," *Accepted by CLEO*, (2017).

7 W. Du, S. A. Ghetmiri, **S. Al-Kabi**, A. Mosleh, T. Pham, Y. Zhou, H. Tran, J. Margetis, J. Tolle, G. Sun, R. Soref, B Li, M. Mortazavi, H. A Naseem, S.-Q. Yu, "Silicon-based $Ge_{0.89}Sn_{0.11}$ photodetector and light emitter towards mid-infrared applications," *SPIE Photonics West,* 10108, 1010813-1, (2017).

6 B. Alharthi, A. Mosleh, J. Margetis, **S. Al-Kabi**, S. A. Ghetmiri, H. Tran, W. Du, M. Benamara, M. Mortazavi, J. Tolle, H. A. Naseem, and S.-Q. Yu, "CVD Growth and

Characterization of SixGe1-x-ySny Alloys for High-Efficiency Multi-Junction Solar Cells," *Photovoltaic Specialists Conference (PVSC), IEEE 43rd*, (2016). DOI: 10.1109/PVSC.2016.7750166.

5 W. Dou, S. A. Ghetmiri, **S. Al-Kabi,** A. Mosleh, W. Du, G. Sun, R. A. Soref, J. Margetis, J. Tolle, B. Li, M. Mortazavi, H. A. Naseem, S.-Q. Yu, "CVD Grown Pseudomorphic GeSn/GeSn and SiGeSn/GeSn Single Quantum Wells," *accepted for EMC conference* 2016.

4 **S. Al-Kabi**, S. A. Ghetmiri, J. Margetis, A. Mosleh, W. Dou, W. Du, G. Sun, R. A. Soref, J. Tolle, B. Li, M. Mortazavi, H. A. Naseem, S.-Q. Yu, "High-Quality CVD Grown Thick GeSn Samples with Enhanced Photoluminescence Intensity," *accepted for EMC conference* 2016.

3 W. Du, S. A. Ghetmiri, **S. Al-Kabi**, A. Mosleh, J. Margetis, J. Tolle, G. Sun, R. A. Soref, B. Li, H. A. Naseem, S.-Q. Yu, M. Mortazavi, "Optical study of $Ge_{0.95}Sn_{0.05}$/$Ge_{0.9}Sn_{0.1}$/$Ge_{0.95}Sn_{0.05}$ quantum-well towards group-IV based light source on Si", *accepted for CLEO conference* 2016.

2 Y. Zhou, W. Du, W. Dou, T. Pham, A. Mosleh, S. A. Ghetmiri, **S. Al-Kabi**, J. Margetis, J. Tolle, G. Sun, R. A. Soref, B. Li, M. Mortazavi, H. A. Naseem, S.-Q. Yu, "Systematic study of Si-based $Ge_{0.9}Sn_{0.1}$ light emitting diode toward mid-infrared application", *accepted for CLEO conference* 2016.

1 S.-Q. Yu, S. A. Ghetmiri, W. Du, J. Margetis, Y. Zhou, A. Mosleh, **S. Al-Kabi,** A. Nazzal, G. Sun, R.A. Soref, J. Tolle, B. Li, and H. A. Naseem, "Si-based GeSn light emitter: mid-infrared device in Si photonics," *SPIE Photonics West*, February 7-12 (2015).

I.3 List of Submitted Works

2 J. Margetis[†], **S. Al-Kabi**[†], W. Du, W. Dou, Y. Zhou, T. Pham, P. Grant, A. Mosleh, S. A. Ghetmiri, B. Li, J. Liu, G. Sun, R. A. Soref, J. Tolle, M. Mortazavi, and S.-Q. Yu, "Si-based GeSn lasers with wavelength coverage of 2 to 3 μm and operating temperatures up to 180 K," *submitted to Nature Photonics.* ***[†] These authors contributed equally***

1 S. A. Ghetmiri, **S. Al-Kabi**, J. Margetis, W. Dou, Y. Zhou, A. Mosleh, W. Du, A. Kuchuk, J. Liu, G. Sun, R. A. Soref, J. Tolle, H. A. Naseem, B. Li, M. Mortazavi, and S.-Q. Yu, "Study the effect of different excitation lasers on the PL emission of GeSn QW structures," *submitted to Journal of Applied Physics.*

I.4 List of Planned Work

1 W. Dou, M. Benamara, A. Mosleh, **S. Al-Kabi**, W. Du, J. Margetis, J. Tolle, B. Li, M. Mortazavi, S.-Q. Yu, “Defect-free GeSn on Ge by Self-Assembled Dislocation Network Formation at Spontaneous Gradient GeSn,” planned to be submitted to *Scientific Report* 2017.

2 H. Alahmad, M. Alher, **S. Al-Kabi**, S. A. Ghetmiri, A. Mosleh, S.-Q. Yu, H. A. Naseem, “Growth and characterization of GePb Alloy using layer inversion method” planned to be submitted to *J. Elect. Mater*., (2017).

3 B. Alharthi, H. Tran, **S. Al-Kabi**, W. Dou, S. A. Ghetmiri, A. Mosleh, J. Margetis, J. Tolle, W. Du, M. Mortazavi, B. Li, H. Naseem, and S.-Q. Yu, “Investigating Structural and Optical Properties of $SixGe_{1-x-y}Sn_y$ Films Grown Using RPCVD Reactor,” planned to be submitted to *J. Elect. Mater*., (2017).

Appendix J. Taken from Author's Published Works

Chapter 3 is largely reproduced from my publication in the Journal Electronic Materials.

S. Al-Kabi, S. A. Ghetmiri, J. Margetis, W. Du, A. Mosleh, M. Alher, W. Dou, G. Sun, R. A. Soref, J. Tolle, B. Li, M. Mortazavi, H. A. Naseem, S.-Q. Yu, "Optical characterization of Si-based $Ge_{1-x}Sn_x$ alloys with Sn compositions up to 12%", *J. Electron. Mater.*, 45 (4) 2133 (2015).

Chapter 4 is mainly reproduced from my publication in the Journal Electronic Materials.

S. Al-Kabi, S. A. Ghetmiri, J. Margetis, A. Mosleh, W. Dou, W. Du, G. Sun, R. A. Soref, J. Tolle, B. Li, M. Mortazavi, H. A. Naseem, S.-Q. Yu, "High-Quality CVD Grown Thick GeSn Samples with Enhanced Photoluminescence Intensity", *J. Electron. Mater.,* 45: 6251. 2016.

Chapter 5 was largely published as:

S. Al-Kabi, S. A. Ghetmiri, J. Margetis, T. Pham, Y. Zhou, B. Collier, R. Quinde, W. Du, A. Mosleh, J. Liu, G. Sun, R. A. Soref, J. Tolle, B. Li, M. Mortazavi, H. A. Naseem, and S.-Q. Yu, "An optically pumped 2.5 μm GeSn laser on Si operating at 110 K", *Appl. Phys. Lett.*109, 16. 2016.